Emission of Radio Waves in Particle Showers:

Validation of microscopic simulations with the SLAC T-510 experiment and their potential in the future Square Kilometre Array

Zur Erlangung des akademischen Grades eines
DOKTORS DER NATURWISSENSCHAFTEN
von der Fakultät für Physik
des Karlsruher Instituts für Technologie (KIT)

genehmigte
DISSERTATION

von Anne Zilles (M.Sc.)
aus Düren

Tag der mündlichen Prüfung: 25.11.2016
Referent: Prof. Dr. Dr. h.c. Johannes Blümer
Korreferent: Prof. Dr. Michael Feindt
Betreuer: Dr. Tim Huege

ABSTRACT

Emission of Radio Waves in Particle Showers:
Validation of microscopic simulations with the SLAC T-510 experiment and their potential in the future Square Kilometre Array

If a high-energetic cosmic-ray particle enters the Earth's atmosphere it induces an extensive air shower of secondary particles which emits a radio signal. The interpretation of air-shower data measured by an antenna array is based on the comparison of the detected radio signals to the results of detailed simulations of the radio emission. This is a common way to interpret air-shower data, but it relies on a complete understanding of the radio emission by a particle shower as well as the ability to model the underlying physics in simulations.

To validate the ability of established microscopic simulations to predict radio emission from a particle shower, the SLAC T-510 experiment was performed. Here, an electron beam of known primary energy was shot into a dense target, which was positioned in a strong magnetic field, inducing a pure electromagnetic cascade. As an integral part of the experiment and in the context of this thesis, microscopic Geant4 simulations were prepared and performed. The simulations include the details of the experimental set-up, such as the beam energy, target geometry and material, and the magnetic field configuration as well as both well-established formalisms for the calculation of radio emission, the endpoint and the ZHS formalisms, running in parallel. Details of the implementation are discussed within this work. As will be shown, a comparison of the measured data of the SLAC T-510 experiment with the results of the detailed simulation study led to the conclusion that both formalisms can predict the absolute scale of the radio signal produced by a particle shower accurately within the uncertainties of the SLAC T-510 experiment. These uncertainties turned out to be dominated by internal reflections of the radio signal at the bottom surface of the target. Furthermore, in this thesis it will be presented that the detailed simulation can describe features of the radio emission from particle showers. Features such as the scaling of the emitted radio signal with the magnetic field strength and the formation of a Cherenkov cone for the magnetic as well as charge excess emission components of the radio signal can be reproduced as measured experimentally within the systematic uncertainties.
The verification of the formalisms for the calculation of radio emission from particle showers is crucial in particular for future high-precision experiments for the radio detection of cosmic rays such as the future SKA1-low antenna array.

Also within this thesis, an initial simulation study is performed, demonstrating that a LOFAR-like approach for the reconstruction of the depth of the shower maximum, is applicable to SKA1-low data. The used reconstruction method is based on the comparison of simulated two-dimensional lateral distribution functions to measured data. It is expected that SKA1-low can measure the depth of the shower maximum for individual air-shower events in the energy region, where the transition from Galactic to Extragalactic origin of cosmic rays is assumed to take place, with such a high precision that a decomposition of the the cosmic ray spectrum into individual element spectra might become feasible. Here, SKA1-low should especially profit from the larger bandwidth at higher frequencies as well as from the extreme density of the antenna array compared to LOFAR.

ZUSAMMENFASSUNG

Emission von Radiowellen in Teilchenschauern:
Validierung von mikroskopischen Simulationen mit Hilfe des SLAC-T-510-Experiments und ihr Potential im zukünftigen SKA1-low-Antennenfeld

Wenn ein hochenergetisches Teilchen der kosmischen Strahlung in die Erdatmösphäre eindringt, löst es einen ausgedehnten Luftschauer aus sekundären Teilchen aus. Die geladen Sekundärteilchen emittieren Radiosignale. Üblicherweise basiert die Interpretation der Luftschauerdaten, die von einem Antennenfeld gemessen wurden, auf den Vergleich zwischen gemessenen Daten und Simulationsergebnissen für das erwartete Radiosignal. Hierbei stützt sich die Herangehensweise jedoch auf ein vollständiges Verständnis der Radioemission in Teilchenschauern als auch auf die Fähigkeit die zugrunde liegende Physik zu simulieren.

Für die Bestätigung, dass gängige mikroskopische Simulationen die Radioemission von Luftschauern vorhersagen können, wurde das SLAC-T-510-Experiment durchgeführt. Hierbei wurde ein Elektronenstrahl mit bekannter Primärenergie in ein Target hoher dichte geschossen, dass in einem starken magnetischen Feld positioniert war. Im Target wurde eine rein elektromagnetische Teilchenkaskade induziert. Als wesentlicher Teil dieses Experiments wurde im Rahmen dieser Arbeit eine Geant4-Simulation, die die Details des experimentellen Aufbaus wie die Strahlenergie, die Targetgeometrie- und material als auch die Magnetfeldkonfiguration beinhaltet, vorbereitet und durchgeführt. Sie greift zudem für die Vorhersage der Radioemission eines Teilchenschauers auf beide gängige Formalismen zur Berechnung des Radiosignals, den Endpunkt- und den ZHS-Formalismus, die parallel implementiert sind, zurück. Ein Vergleich der gemessenen Daten des SLAC-T-510-Experiments mit den Ergebnissen der mikroskopischen Simulationsstudie führt zur Schlussfolgerung, dass beide Formalismen die absolute Skala des Radiosignals von einem Teilchenschauer innerhalb der Unsicherheiten des SLAC-T-510-Experiments präzise vorhersagen können. Wie sich herausgestellt hat, sind die experimentellen Unsicherheiten von Reflexionen des Signals innerhalb des Targets dominiert. Des weiteren wird in dieser Arbeit gezeigt, dass die detaillierten Simulationen Eigenschaften der Radiostrahlung von Teilchenschauern beschreiben können. Das Skalieren des Signals mit der Magnetfeldstärke als auch die Ausbildung eines Cherenkovrings, sowohl für die durch den Askaryaneffekt als auch für die durch den magnetischen Effekt dominierte Komponente der Radiostrahlung, können im Vergleich zu Messungen innerhalb der systematischen Unsicherheiten reproduziert werden. Die Verifizierung der Formalismen zur Berechnung der Radiostrahlung von Teilchenschauern ist entscheidend für zukünftige Hochpräzisionsexperimente in der Radiodetektion von Luftschauern, wie das geplante SKA1-low-Antennenfeld.

Ebenfalls in dieser Arbeit wurde eine erste Simulationsstudie angefertigt, in der gezeigt wird, dass die Methode zur Rekonstruktion der Tiefe des Schauermaximums, die bei LOFAR angewandt wird, auch auf SKA1-low-Daten anwendbar ist. Die Methode basiert auf den Vergleich von simulierten zweidimensionalen Funktionen der Lateralverteilungen mit gemessenen Daten. Es wird erwartet, dass SKA1-low die Tiefe des Schauermaximums für individuelle Luftschauerereignisse im Energiebereich, in dem der Übergangs von galaktischen zum extragalaktischen Ursprung der kosmischen Strahlungen erwartet wird, mit einer so hohen Auflösung messen kann, das die Zerlegung des Spektrum der kosmischen Strahlung in einzelne Elementspektren machbar scheint. Dabei sollte SKA1-low insbesondere von der weiten Frequenzbandbreite bei hohen Frequenzen als auch von der extrem hohen Dichte des Antennenfeldes im Vergleich zu LOFAR profitieren.

CONTENTS

1 INTRODUCTION

Cosmic rays are charged particles propagating through the Universe, whose origin has not yet been fully understood. Some of them reach energies beyond the energies achieved by human technology and therefore they probe particle physics that cannot not be reproduced in a laboratory setting. They have to originate from astronomical objects that belong to the most violent objects known in the universe. In Astroparticle Physics, the study of cosmic rays connect the knowledge of the largest structures in the Universe with the knowledge about the smallest sub-structures of matter and the forces in-between them.

When such highly energetic cosmic rays impinge on the Earth's atmosphere, they create extensive air showers, cascades of secondary particles. During the shower development, the shower particles emit a radio signal which can be measured with radio antenna arrays on the ground.

The interpretation of air-shower radio measurements is based on the comparison of the measured radio signal to detailed simulations of the radio emission. This is a common way to interpret air shower data, but it relies also on a complete understanding of the radio emission from a particle shower as well as the ability to model the underlying physics in simulations. Here, the main uncertainties arise from the hadronic interaction models used in the simulations and the unknown primary particle. In the last 5 years, huge progress in the analysis of data measured by radio antenna arrays was made. Especially, the measurements of the depth of the shower maximum of individual air-shower events by LOFAR, which is based on the comparison to simulated two-dimensional lateral distribution functions from CoREAS simulations, demonstrated how extremely detailed the simulation can reproduce the radio signal from an air shower.

Nevertheless, before starting this thesis, there was the question whether the used microscopic simulations are able to predict radio emission from an air shower accurately, that needed to be answered to prepare for future high precision experiments in the field of radio detection of air showers. Therefore, it is crucial to validate the predictions of microscopic calculations with different systematic uncertainties than in air shower measurements, such as uncertainties in the hadronic interaction models. To this end, the SLAC T-510 experiment was realised, where a pure electron beam of known parameters was shot into a dense target, positioned in a strong magnetic field. An integral part of the experiment was the performance of a detailed simulation study including both well-established formalisms for the microscopic calculation of radio emission from particle showers, the endpoint and the ZHS formalisms. The preparation and the execution of this simulation study as well as the comparison of the simulated results to measured data and its interpretation is done in the scope of this thesis.

In addition, LOFAR, an instrument designed for performing radio astronomy, successfully

measured the mass composition of the cosmic rays in the energy region where the transition from Galactic to Extragalactic origin is assumed to happen. Inspired by the great success of LOFAR, a second project within this thesis deals with the performance of the future Square Kilometre Array as a high-precision detector for cosmic rays via the radio detection of individual air-shower events. Here, the investigation focuses on whether a LOFAR-like approach for the reconstruction of the depth of the shower maximum is also applicable to SKA1-low data and how precisely the depth of the shower maximum could then be measured.

The thesis is structured as follows: After a short introduction to the field of cosmic ray physics, given in Chapter 2, the current status of the modeling of radio emission from air showers is discussed in Chapter 3. Details of the experimental setup and the performance of the laboratory experiment SLAC T-510 to measure the radio emission from a particle shower with known parameters can be found in Chapter 4. While the realisation of the corresponding simulation study is documented in Chapter 5 , the comparison of the resulting predictions with measured data and its interpretation is given in Chapter 6. Chapter 7 gives then an introduction to the idea of enabling SKA1-low as a cosmic ray detector and to the approach of the reconstruction of the mass composition via a comparison of simulated two-dimensional lateral distribution functions to measured data. Finally, a preliminary simulation study on the potential of SKA1-low and its results are presented and discussed.

2 COSMIC RAYS AND EXTENSIVE AIR SHOWERS

Cosmic rays are highly energetic particles from the outer space, hitting the Earth's atmosphere every day. They consist of atomic nuclei (98%) and 2% electrons [1] and a small contribution of γ rays. Out of the atomic nuclei, 87% protons, 11% helium nuclei and 2% heavier nuclei contribute to this component. The composition of cosmic rays arriving at the Earth changes with energy. As shown in Fig. 1, the energy spectrum of the cosmic rays extends over 11 orders of magnitude in energy and the particle flux varies over 31 orders of magnitude. The energies reach from less than a few 100 MeV up to at least a few 100 EeV.

The energy spectrum can be described by a power law: the particle number N at a certain energy E, observed in a solid angle Ω, area A and in a time t can be written as $\frac{dN}{dE\,d\Omega\,dA\,dt} \propto E^{-\gamma}$ with a spectral index $\gamma > 0$. Here, the energy spectrum can be split into three regions: For energies below the so-called "knee" at $E \approx 10^{15.5}$ eV, the spectral index is $\gamma = 2.7$. Above this energy, the value changes to $\gamma = 3.1$.
A possible interpretation of the change in the spectral index is that for these energies the acceleration mechanisms of typical galactic sources are at their energy limit with the maximal energy scaling with the charge of the elements. First, protons would reach their maximum energy, then helium nuclei and so on. This could be observed as a transition from light to heavy composition as measured by KASCADE-Grande [3]. These features of a break-off of particular element spectra can be explained by an electromagnetic acceleration mechanisms and are observed by dividing the spectrum into mass groups.
At an energy of about 10^{17} eV, another slight kink is observed where the spectral index changes from $\gamma = 3.1$ to $\gamma = 3.3$. Different experiments reported on this feature at slightly different energies, sometimes called the "second knee" [4, 5, 6]. For example KASCADE-Grande split up the energy spectrum into different mass groups and found a steepening of the spectrum for heavy cosmic rays, the "heavy knee". This assumption would fit to a rigidity-dependent limit in the particle acceleration of the dominant source type at the knee region. For higher energies, a light component from a possible extra-galactic origin becomes dominant.
To clarify whether the "second knee" and the "heavy knee" describe the same or completely different features of the spectrum is hard until a comparison of the energy scales between the different experiments using an independent measurement, e.g. via radio detection, is performed.

At an energy of about $10^{18.5}$ eV, another change in the spectral index to $\gamma = 2.7$ is observable, the so-called "ankle" [7].
For energies above $E = 10^{19.4}$ eV a strong suppression of the flux is observable so that even devices specialised for detection of ultra-high energy cosmic rays (UHECR) have not enough exposure. One explanation is a propagation effect, the so-called "GZK-Cutoff" (Greisen-Zatsepin-Kuzmin) [8, 9] at an energy of $6 \cdot 10^{19}$ eV. It is assumed that protons of an energy of $6 \cdot 10^{19}$ eV interact with photons of the cosmic microwave background. This

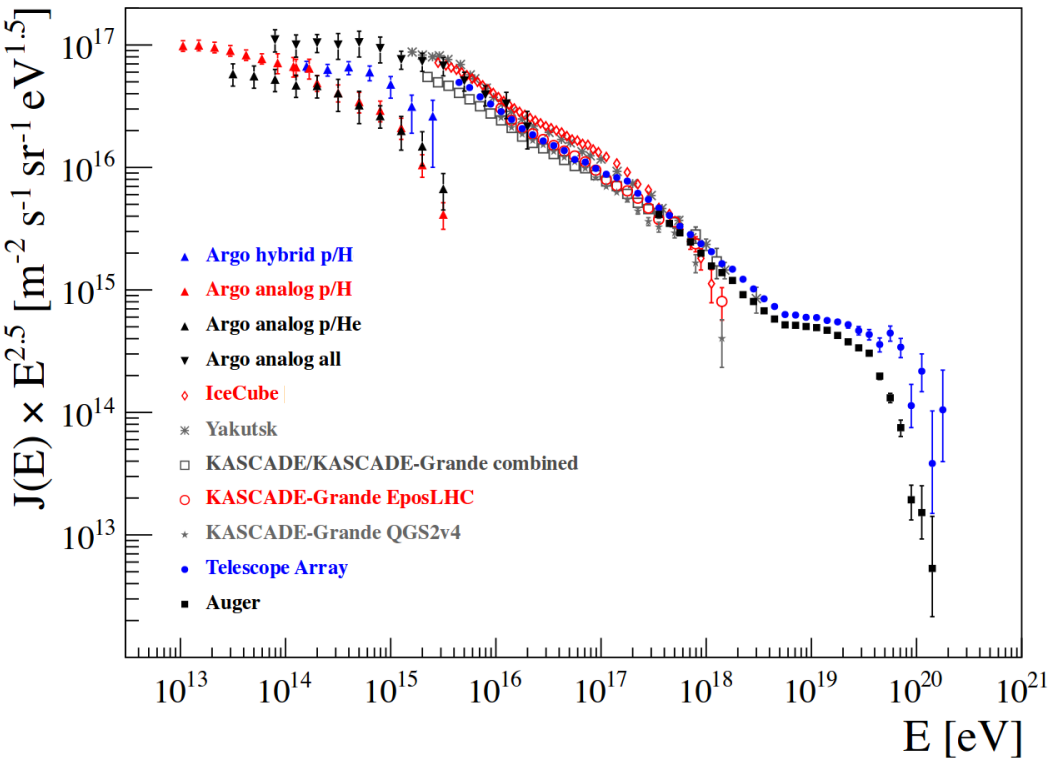

Figure 1: A compilation of the energy spectrum of cosmic rays measured by several experiments. Adapted from [2].

produces a Δ-resonance which decays into pions and protons or neutrons, respectively, which limits the mean free path length of the original particle and far sources are not visible anymore above this threshold energy. For heavier nuclei, photodisintegration would lead to a similar effect [10]. The cut-off at these energies could, however, also be explained by a maximum energy of the sources [11].

The steep energy spectrum leads also to the conclusion that cosmic rays are accelerated actively and non-thermally, since temperatures of higher than 10^{16} K would be necessary to accelerate the particle to such high energies. These temperatures were only achieved right after the Big Bang. Furthermore, the description of the energy spectrum by a power-law excludes thermal acceleration. Otherwise, the energy spectrum would follow an exponential function. This leads to the conclusion that this spectrum is dominated by a collective, non-thermal acceleration, for example by shock fronts.

To explore the origin of cosmic rays, which is one of the biggest challenges in experimental astroparticle physics, reliable measurements of the mass compositions as a function of the cosmic-ray energy are necessary.
Since the energy spectrum for cosmic rays extends over so many magnitudes with decreasing flux for high energies, the complete spectrum can not be measured by one single experimental setup. While at energies below 10^{14} eV composition and flux is accurately measured as a function of energy directly by space- and balloon-borne experiments [12, 13], at higher energies the flux of cosmic rays is too low to obtain sufficient statistics with direct measurements. Here, a indirect measurement of the secondary particles produced in a so-called

extensive air shower in the Earth's atmosphere must be performed. Air shower experiment are specialised for a specific energy region, for example by instrumenting a huge detection area to measure the particles of the highest energies [7].

2.1 EXTENSIVE AIR SHOWERS

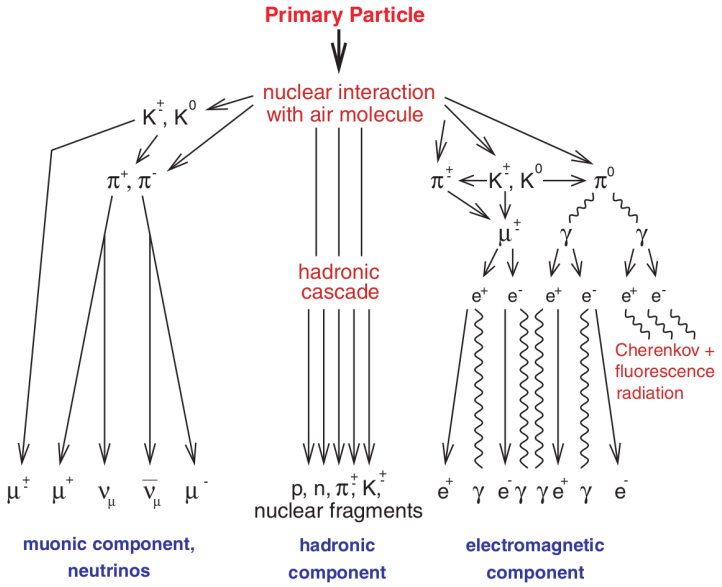

Figure 2: Sketch of an air shower induced by a cosmic ray particle [14]. The secondary particles in the shower can be grouped into three components: The muonic component including neutrinos, the hadronic and the electromagnetic component.

The cascade of ionised particles and electromagnetic radiation in the atmosphere induced by a primary cosmic particle is also called extensive air shower. A schematic view of the development of such an air shower is shown in Fig. 2.

Via a nuclear interaction, a primary particle interacts with a nucleus of the Earth's atmosphere and produces secondary particles. These secondaries can be ordered in three groups: the muonic component consists of muons and neutrinos, the hadronic one of protons, neutrons, nuclear fragments, neutral and charged pions and kaons, and the electromagnetic component is composed of electrons, positrons and photons (see Fig. 2).

The lateral and longitudinal profile of the air shower split up into the single components is displayed in Fig. 3. The number of particles in a shower differs between the specific components and changes which the shower depth as well as the distance to the shower axis. Since the individual shower profiles also depend on the primary particle, they can be used to study the mass composition of cosmic rays via indirect detection. The atmosphere, acting as a calorimeter, can be used for measurements of up to at least 10^{20} eV using very large detector arrays at the Earth's surface to observe areas of up to thousands of square kilometers. More details can be found in Section 2.4.

The interpretation of air-shower measurements is still limited by systematic uncertainties,

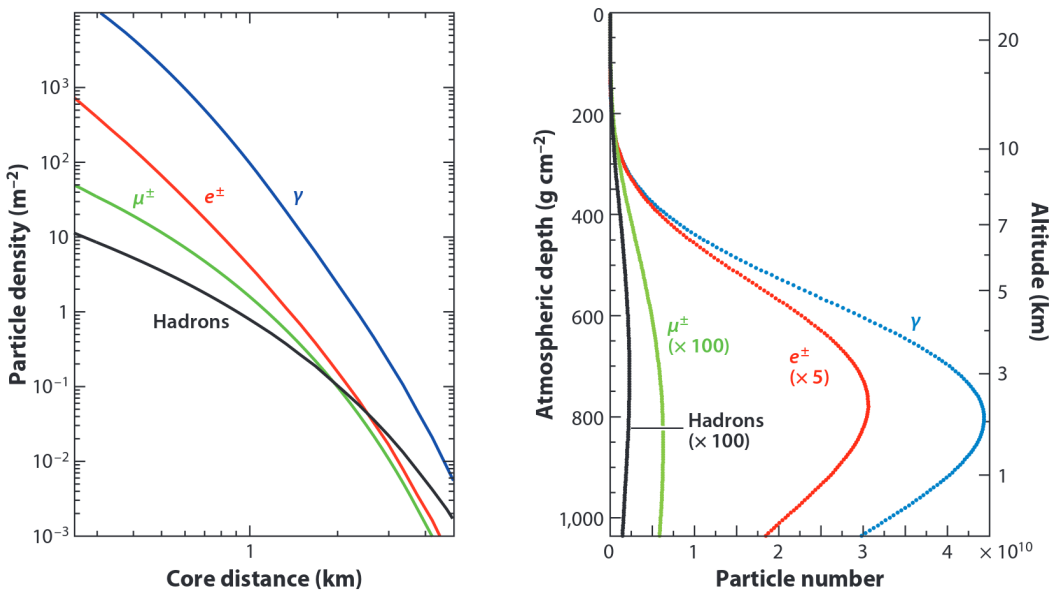

Figure 3: Average lateral (left) and longitudinal (right) shower profiles for vertical showers, induced by protons with an energy of 10^{19} eV [15]. The lateral distribution of the particles at ground is calculated for an atmospheric depth of 870 g/cm^2.

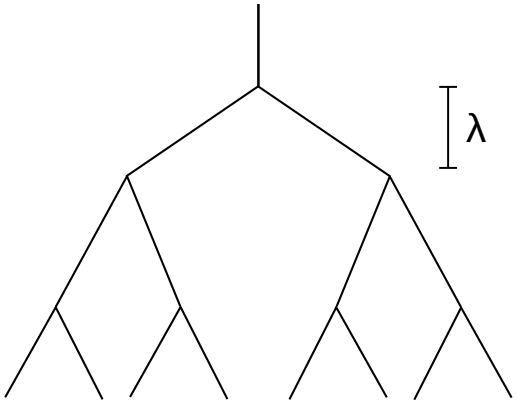

Figure 4: Heitler model: Sketch of the air shower described by a simple branching model.

particular in the hadronic interactions models used in air-shower simulations. Low statistics at the highest energy also pose a problem.

2.1.1 Heitler's toy model

Heitler developed a simple model to describe some general features of an air shower in the context of purely electromagnetic cascades [16]. But the basic structure can be also applied to air showers induced by hadrons. In this model, it is assumed that each line element, as demonstrated in figure, represents a particle or a packet of energy. This line element undergoes a branching process after one collisions length λ [11]. At each vertex, where the branching process happens, the energy on a line is split in two. After $n = X/\lambda$ steps with X as the slant depth along the shower axis, the number of segments is given by

$$N(X) = 2^{X/\lambda}. \tag{1}$$

The energy per particle at a slant depth X is defined as

$$E(X) = E_0/N(X). \tag{2}$$

Until reaching the critical energy E_C for the splitting process, the splitting continues. For electromagnetic cascades the critical energy is about $E_C \approx 87\,\text{MeV}$ [11]. For energies lower than that, the particles only lose energy, get absorbed or decay. With this model, characteristic parameters as the number of particles at the shower maximum

$$N(X_{\text{max}}) = E_0/E_C \tag{3}$$

and the shower maximum

$$X_{\text{max}} = \lambda \frac{\ln(E_0/E_C)}{\ln 2} \tag{4}$$

can be achieved. For hadronic cascades, these features can be approximately described by:

$$N_{\text{max}} \propto E_0 \text{ and } X_{\text{max}} \propto \ln(E_0). \tag{5}$$

2.2 MASS COMPOSITION OF COSMIC RAYS

To answer the question where the structure in the energy spectrum comes from and in the end to distinguish between models for sources and propagation of cosmic rays, the energy spectrum has to be measured in detail, preferably by splitting it up into single elements.
Fig. 5 shows results for direct measurements by different experiments for energies below $10^{14}\,\text{eV}$. The abundance of cosmic rays follows roughly the distribution of elements in the solar system. Hydrogen and helium dominate the element distribution. Elements with higher charge numbers up to nickel, originating from star burning are found with more than 2-3 orders of magnitude lower fluxes. For heavier elements the abundance drops by several orders of magnitude. Deviations between the measured cosmic element and the solar element distributions as observed for lithium (Li), beryllium (Be) and boron (B) can be explained by spallation of carbon (C), oxygen (O) and iron (Fe) during their propagation [17]. A detailed study was performed by the TIGER collaboration [18], supporting the model of a cosmic-ray origin in OB spectral classes. Supernovae which mostly occur in OB associations are therefore prime candidates as substantial contributor to galactic cosmic rays. Since for energies above $10^{14}\,\text{eV}$ direct measurements are not feasible, the mass of the primary particle has to be reconstructed from measurements of air showers. The reconstruction often relies on Monte Carlo simulations which leads to a model dependence. Especially for energies larger than those reached in particle accelerators, this introduces a source of a large systematic uncertainty. The separation of different primary masses is determined statistically since the separation of different masses in air-shower measurements is not clear enough to distinguish them on a shower-to-shower basis. To analyse the measurement in terms of a mean mass, model simulations of proton and iron induced air showers are used for comparison. These elements mark the extremes of dominating elements in the cosmic rays (compare to Fig. 5).

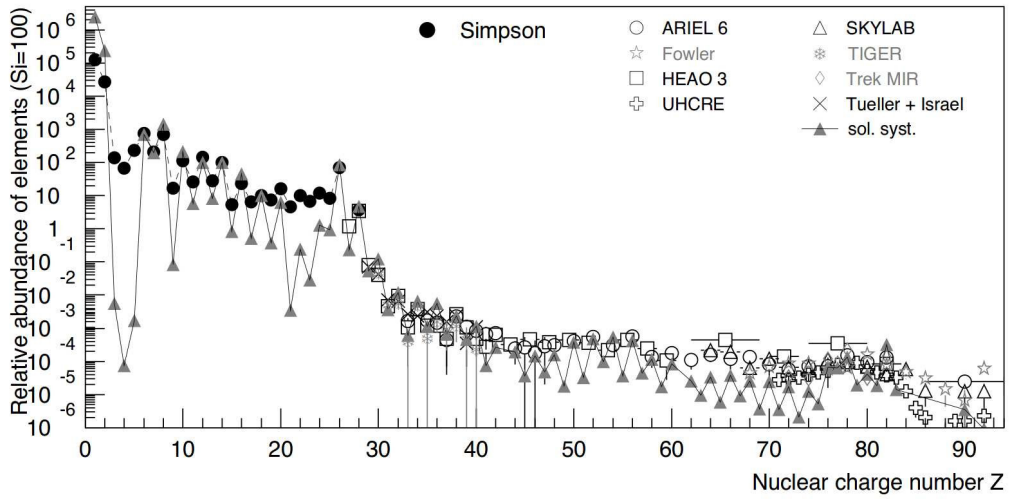

Figure 5: Nuclear Abundance: Abundance of elements in cosmic rays (black) and abundances in the solar system (gray) as a function of their nuclear charge number Z at energies around 1 GeV/n, normalised to the silicon abundance [17]. In the solar system, Hydrogen (H) and helium (He) are the dominating elements. At high charge numbers, above silicon (Si), iron (Fe) is the dominating element.

Fig. 6 shows a compilation of the measurements of the mean depth of the shower maximum, a mass-sensitive parameter, as a function of energy via different detection techniques. This is compared with the results from air-shower simulations using the hadronic interaction model QGSJET-II [19], Sibyll2.1 [20] and EPOSv1.99 [21] and for proton- and iron-induced air showers. While the composition at an energy of about 10^{15} eV is observed to become heavier, it seems to evolve to a lighter composition again for energies above 10^{17} eV. This is also consistent with the measurements of the KASCADE-Grande experiment [3]. For the highest energies the interpretation of the measurements slightly differs between experiments due to systematic uncertainties [22].

2.3 POSSIBLE SOURCES OF COSMIC RAYS

Since cosmic rays are charged and therefore deflected by interstellar and intergalactic magnetic fields, they cannot be traced back to their origin. Only at extremely high energies above $10^{19.5}$ eV protons can transverse the Milky Way without significant deflection. There are indications for a correlation between candidates for extragalactic sources at these energies which could not be confirmed so far [25]. For lower energies, a modeling of the sources and their propagation is needed.

It is believed that cosmic ray particles gain their observed energies in prolonged, cyclic processes. The observed power-law shape of their energy spectrum can be explained by stochastic acceleration in their sources [26]. Here, a relativistic shock acceleration could lead to an efficient energy gain. Based on these assumptions, possible source candidates

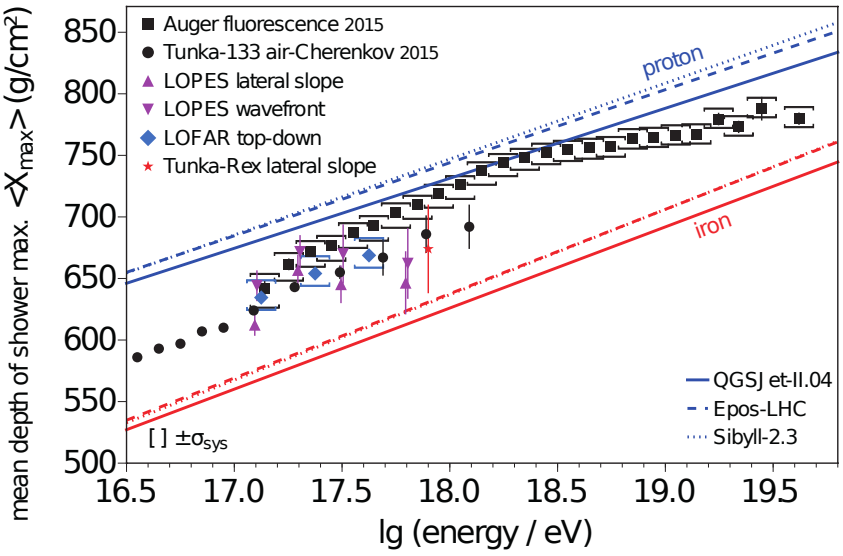

Figure 6: Overview on different measurements of the mean X_{max} by selected air-Cherenkov experiments, air-fluorescence detectors, and radio measurements in comparison to the predictions by CORSIKA simulations based on different hadronic interaction models for pure proton and iron compositions [23].

can be identified. To accelerate a particle of charge Z to a maximum energy of E_{max}, the source has to fulfill the condition

$$E_{max} = 1/2 \cdot 10^{18}\,\text{eV} \cdot \beta \cdot Z \cdot R/\text{kpc} \cdot B/\mu\text{G}. \tag{6}$$

with the source size R, the magnetic field strength B and with the relativistic shock speed $\beta = v/c$.
For energies up to 10^{15} eV, galactic cosmic rays might be accelerated in shock fronts of supernova remnants (SNR). SNRs have sufficient energy output and the measured cosmic-ray mass composition at lower energies is consistent with theoretical predictions of SNR models [27, 28]. In addition, gamma-ray measurements observe supernova remnants as hadronic acceleration sites [29].

The interpretation of features in the energy spectrum and the mass composition of cosmic rays lead to the conclusion that at energies of 10^{17} eV another type of source becomes dominant. Possible candidates can be determined by equation 6. As shown in Fig. 7, active galactic nuclei, neutron stars or gamma ray bursts could be potential acceleration sites.
For energies at 10^{20} eV, a convincing source candidate is not yet found.

2.4 INDIRECT DETECTION OF COSMIC RAYS VIA AIR SHOWER MEASUREMENTS

For the detection of air showers different techniques exist. One general type of detector are particle detector arrays which measure the lateral profile of an air shower, whereas optical detectors measure the longitudinal profile. The third option, the detection of air showers via radio emission, is presented in Chapter 3.2.
To profit from the different advantages of the particular detection methods, different techniques are often combined within one experiment.

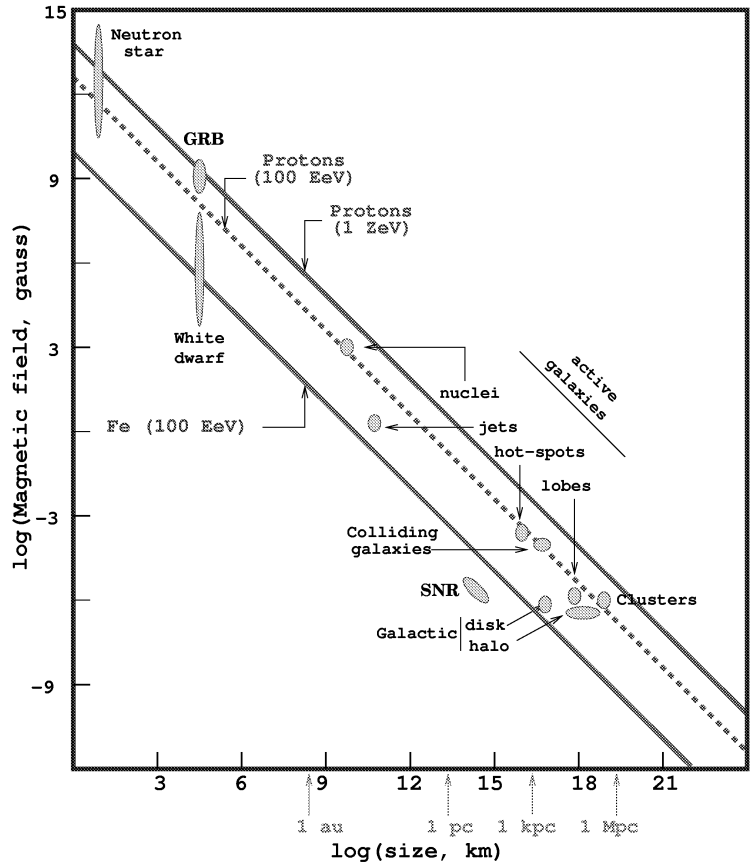

Figure 7: “Hillas plot”, showing possible candidates for the acceleration of Ultra High Energy Cosmic Rays and the maximum energy attainable in these in dependence on the source size R and the local magnetic field strength B [24].

2.4.1 Particle detectors

For energies above 10^{14} eV a significant number of particles, produced in an air shower as secondary particles, can reach the ground and can be detected by particle detectors. In experiments like KASCADE-Grande [30], the particles are detected with scintillator detectors. Here, ionizing particles produce light while transversing the scintillating material. Other experiments like the Pierre Auger Observatory [31] use water-Cherenkov detectors for particle detection. These are huge tanks filled with water and equipped with photomultipliers. The photomultipliers detect the Cherenkov light produced by the particles transversing the water. The spacing between the single detector stations as well as the covered area determine to which primary cosmic ray energy the particle detector array is sensitive. The KASCADE experiment with the spacing of 13 m and an area of $200 \times 200\,\mathrm{m}^2$ measured air showers from 10^{14} eV to 10^{16} eV. At the Pierre Auger Observatory, the water tanks have a distance of 1.5 km to each other covering an area of $50 \times 70\,\mathrm{km}^2$. Air showers of energies from about $10^{18.5}$ eV to 10^{20} eV can be measured.

A full duty cycle is the advantage of particle detector arrays which maximises statistics. Therefore, particle detectors are best to apply for measurements of the energy spectrum up to the highest energies. Their energy resolution is about $20 - 30\%$, but sensitive to

a model-dependence of the energy scale since they rely on air-shower simulations. The strong model dependence influences the reconstruction of the mass composition. Therefore, particle detectors are often combined with other techniques, like optical detectors or radio arrays as done e.g. at the Pierre Auger Observatory (see Chapter 3.2.2). In combination with other detectors, the interpretation of their measurements is less model dependent.

2.4.2 Optical detectors

The electromagnetic emission, close to optical wavelengths, of an air shower can be measured by optical detectors. Since the refractive index of air slightly differs from unity, the charged particles of an air shower produce Cherenkov radiation. The emission is concentrated in the forward direction and is therefore already detectable at energies of about 10^{10} eV. This is used by imaging telescopes, as MAGIC(-II) [32] or H.E.S.S. [33], to measure deep air showers induced by gamma rays. Their huge mirror telescopes detect the Cherenkov-ring of the air shower directly, in contrast to non-imaging Cherenkov detectors. Here, sparse arrays of photomultipliers detect the coincident flash of UV light over an extended area, as is done at the Tunka-133 [4] or the Yakutsk experiment [34].

Interactions of air-shower particles and nitrogen in the air lead to the emission of fluorescence light which can be detected for energies above 10^{17} eV. The detection is also performed with mirror telescopes as done at the Pierre Auger Observatory [31], but aiming on recording a side view of the shower development.
After correction for geometry and absorption of light, the depth of shower maximum can be directly determined from the longitudinal shower profile since the intensity of the fluorescence light is proportional to the number of particles in the shower.
Future experiments such as JEM-EUSO [35] are designed as satellite-borne fluorescence telescopes in space. They will observe huge volumes of the Earth's atmosphere from above, to detect cosmic rays beyond energies of 10^{20} eV.

Optical detection has a good sensitivity to the depth of the shower maximum of $20 - 30\,\mathrm{g/cm^2}$ and a high precision of $10 - 15\%$ in energy since this detection technique is mainly sensitive to the electromagnetic component of the shower maximum [36]. The energy scale can be calibrated absolutely with a reference source and is less dependent on air-shower models. The disadvantage of this technique is the low duty cycle since the operation is limited to clear, moonless nights, and the sensitivity to the conditions of the atmosphere.

3 MODELING OF RADIO EMISSION FROM PARTICLE/AIR SHOWERS

The electromagnetic component of the particle shower creates radio emission while propagating through the Earth's atmosphere or through a dense medium. Pulses of a length of tens of nanoseconds are produced, varying in amplitude between pulses hidden in the Galactic noise and pulses with amplitudes orders of magnitudes above the Galactic noise. The signal can be interpreted by two main mechanisms for emission of the signal (compare to Fig. 8):

The first, the so-called Askaryan effect [37, 38], can be described as a variation of the net charge excess of the shower in time ($\dot{q}$), in combination with Cherenkov-like effects due to the refractive index of air which will be described later. During the shower development, first the absolute negative charge grows until the shower reaches its maximum and finally decreases when the shower dies out. In a shower secondary electrons, positrons and gamma rays are produced. They develop an electromagnetic sub-shower in which an excess of negative charge is acquired. Even if the interactions with the medium are completely charge-symmetric, the excess arises since the matter in the medium only contains electrons. The interaction of the shower with atomic electrons leads to a charge asymmetry: Møller ($e^- + e^-_{\text{atom}} \rightarrow e^- + e^-$), Bhabha ($e^+ + e^-_{\text{atom}} \rightarrow e^+ + e^-$) and Compton ($\gamma + e^-_{\text{atom}} \rightarrow \gamma + e^-$) scattering of matter electrons accelerate matter electrons into the shower. In addition electron-positron annihilation ($e^+ + e^-_{\text{atom}} \rightarrow \gamma\gamma$) and Bhabha scattering decelerate shower positrons which also contributes to the charges excess in the shower. Effectively, the surrounding medium is ionised by the (air) shower particles and the ionisation electrons are swept into the cascade, whereas the heavier positive ions stay behind. In a non-absorptive, dielectric medium the time-variation of the net charge excess develops a coherent electromagnetic pulse. A first measurement of a radio signal produced by the Askaryan effect by firing photon bunches into sand were done at SLAC in 2000 [39] and later also in dielectric media like ice [40, 41].

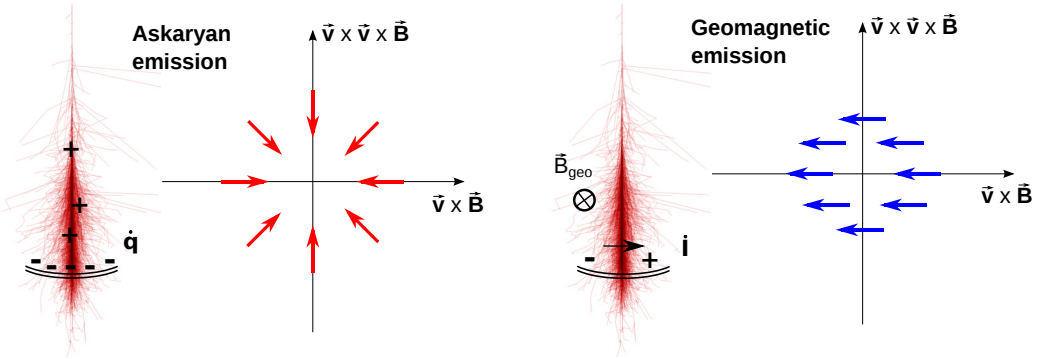

Figure 8: Main radio emission mechanisms in an extensive air-shower and the polarisation of their corresponding electric field in the shower plane.

The radio signal is linearly polarised. The electric field vector is oriented radially around the shower axis, so the orientation of the electric field vector depends on the location of an observer with respect to the shower axis. This effects plays a sub-dominant role in air showers, while it is the dominant contribution to the radio signal of showers in dense media. E.g. the Auger Engineering Radio Array (AERA) located in Argentina measured a contribution of $(14 \pm 2)\%$ effect to the radio signal compared to the component induced by the geomagnetic-emission process [42].

The second mechanism and the main mechanism in air shower is the (geo-)magnetic effect: Here, a radio signal gets emitted by the time-variation of the transverse current in the shower ($\dot{I}$). The secondary electrons and positrons in the shower are accelerated by a (geo-)magnetic field. The acceleration takes place in the shower front. Following the Lorentz force $\vec{F} = q\vec{v} \times \vec{B}$ (q: particle charge, $\vec{v}$: velocity vector/propagation direction, $\vec{B}$: magnetic field vector), the electrons and positrons get deflected in opposite directions. They are decelerated due to the interactions with air molecules. In total, this leads to a net drift of the electrons and positrons, moving perpendicular to the shower axis, which can be described by transverse currents.
As also for the Askaryan effect, during the shower development, first the number of secondary particles grows until it reaches its maximum and then the number starts to decrease, the shower dies out. So, the transverse currents vary in time which leads to electromagnetic radiation. The polarisation of this signal is linear with the electric field vector aligned with the Lorentz force (along $\vec{v} \times \vec{B}$). All charged particle can be affected by a magnetic field. But since electrons and positrons have the highest charge-to-mass ratio, only they can contribute significantly to the radio signal (muons are too heavy).
The (geo-)magnetic component of the radio signal was confirmed in a number of experiments. This effect has even been already observed in the 1960s [43]. Nowadays, for example, experiments as the CODALEMA experiment [44] as well as LOPES [45], AERA [46], LOFAR [47] and Tunka-Rex [48] showed that the amplitude of the radio pulse depends on energy and direction of the shower as well as they confirmed the geomagnetic effect as dominant mechanism.

Coherence and Cherenkov-like effects:
For wavelengths large compared to the thickness of the air shower disk (of the order of meters) the relative phase shifts acquired during propagation are negligible, and the vectorial electric fields add up coherently. Then, the electric field amplitude scales linearly with the particle number and thus (approximately) with the energy of the primary particle. The received power then scales quadratically with the energy of the primary particle. Here, the coherence is frequency-dependent and more prominent at low frequencies below 100 MHz. However, since the refractive index of air is slightly larger than 1 and scales with altitude, the radio waves travel slightly more slowly through the air than the relativistically moving particle front. In addition to a strong forward-beaming of the emission, this leads to a so-called Cherenkov compression. For a given emission region along the shower axis and a particular observer position on ground, the emission is time-compressed since radiation emitted by the whole shower arrives simultaneously (see sketch in Fig. 9). The pulses become very narrow, being coherent up to frequencies in the GHz region.

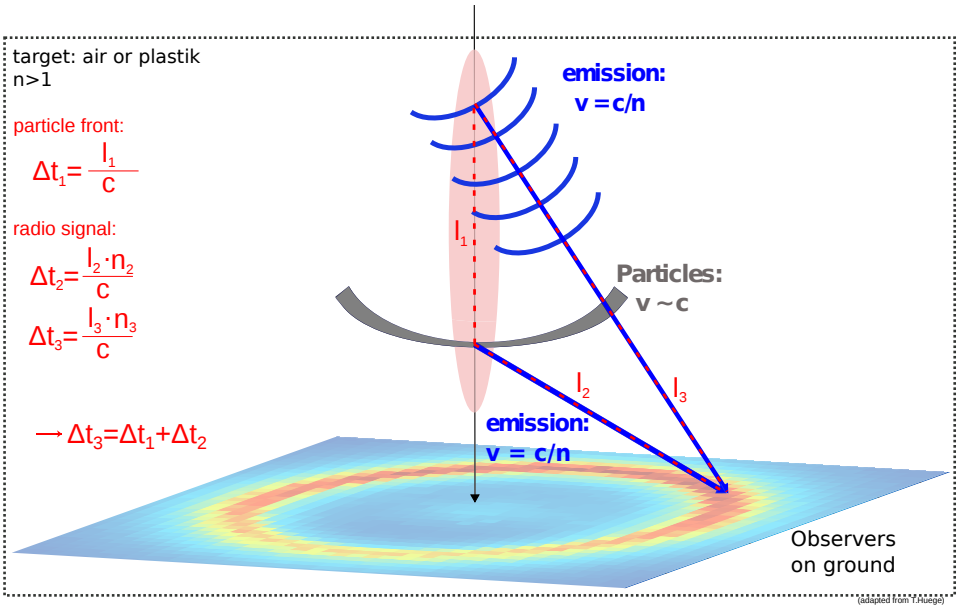

Figure 9: Sketch of Cherenkov-like effects in the radio emission of a particle shower causing a ring structure in the footprint on ground.

These observer positions can be found on the "Cherenkov ring", given by $\cos(\theta_{Ch}) = \frac{1}{n \cdot \beta}$ with n being the refractive index of the medium, which depends on the height of emission, and β is the particle velocity. For air the Cherenkov angle has a typical value of 1° which leads to a typical radius on ground of $100 - 200$ m for a vertical 10^{17} eV air shower.
For positions inside the cone it is expected that the radiation from the end of the shower arrives earlier than the contributions from the early shower. For positions outside the Cherenkov cone it should be the opposite, so that a time reversal is expected to be observed by crossing the Cherenkov angle. Such a reversal, i.e. the early emission arrives before the late emission, is not observed.

In dependence of the position of the observer and hence the orientation of the electric field vector for the two emission machanisms the two contributions can add constructively or destructively, leading to an asymmetric ring structure as a "radio footprint" on the ground (s. Fig. 9). The degree of asymmetry is influenced by the relative contributions of the (geo-)magnetic and Askaryan effects, depending on the angle of the magnetic field to the shower axis and the effective field strength.
As the results from LOFAR showed [49] the radio emission of air showers is elliptically polarised which is a mixture of linear and circular polarisations. Based on the theory of emission by both main effects, one would reason that during the shower evolution the emission of both components would superpose constructively. This would lead to a purely linear polarisation and the electric field vector should trace a line perpendicular to the shower axis. But, since the emission by the Askaryan and the (geo-)magnetic effect are slightly offset over the longitudinal evolution of the air shower, the pulses associated with the single emission mechanisms do not arrive at the observer simultaneously and the electric field vector traces an ellipse [50].

3.1 MICROSCOPIC MODELING

Describing the radio signal using the (geo-)magnetic and the Askaryan effect as emission mechanisms is a macroscopic description.
In microscopic approaches, no assumption on the nature of the radiation needs to be made. Two well-established formalisms based on first principles will be presented in this section. Both are applicable in Monte-Carlo simulations of particle showers. For the simulation of the interaction and the propagation, a continuous particle track is approximately described by being split up into short, straight sub-tracks as illustrated in Fig. 10.

In the calculation of the radio emission of a particle shower, each single electron and positron is considered separately. Its emitted radio signal is calculated and propagated to the observer position. Here, the signal of all particles are superposed to arrive as the total radio emission of the whole shower. Coherence effects are automatically taken into account by a proper handling of the propagation to account also for the time delays of the emission from individual particles. In that way, this classical electrodynamics calculation of the radio emission does not separate the single emission mechanisms and has no free parameters that would influence the resulting electric field.

To derive formalisms representing this approach, one starts with Maxwell's equations for linear, isotropic, homogeneous and non-dispersive media, in the relativistic case [51] and derives the Liénard-Wiechert potentials describing the electric field from charged particle motion. The resulting formula is valid for vacuum and has to be modified to introduce a refractive index:

$$\Phi(\vec{x},t) = \left[\frac{q}{(1-n\vec{\beta}\cdot\hat{r})R}\right]_{\text{ret}} \quad \text{and} \quad \vec{A}(\vec{x},t) = \left[\frac{q\vec{\beta}}{(1-n\vec{\beta}\cdot\hat{r})}\right]_{\text{ret}} \tag{7}$$

with $q = \pm e$ defining the particle charge, n describes the refractive index of the medium at the particle position, $R = |\vec{R}(t)|$ is the distance of the particle position to the observer, and $\hat{r} = \vec{R}(t)/|\vec{R}(t)|$ represents the line-of-sight direction between particle and observer (unit-vector in the direction of the observer). The parameter $\vec{\beta} = \vec{v}/c$ is given by the particle's velocity $\vec{v}$ and the index "ret" indicates that the equation has to be evaluated at the retarded time $t' = t - nR/c$ for the observer position $\vec{x}$ at the time t. Based on the vector potentials of equation 7 the electric field of a moving charged particle can be derived as:

$$\vec{E}(\vec{x},t) = -\nabla\Phi(\vec{x},t) - \frac{\partial}{\partial t}\vec{A}(\vec{x},t). \tag{8}$$

3.1.1 The endpoint formalism

This chapter gives a concise summary of the endpoint formalism, while details can be found in [52].

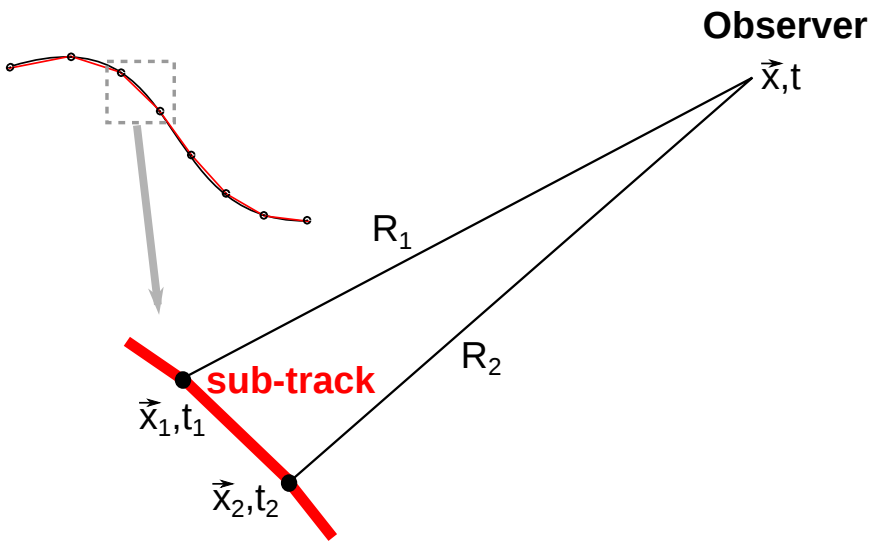

Figure 10: Sketch for defining parameters for the endpoint formalism to describe the particle track and the observer position. The curved, black line at the top represents a particle trajectory which can be approximated by a series of short, straight sub-tracks (red).

The result from combining the formulas 7 and 8 represents the electric field in a dielectric, non-magnetic medium for a particle with Lorentz factor γ and a charge q:

$$\vec{E}(\vec{x},t) = q\left[\frac{\hat{r}-n\vec{\beta}}{\gamma^2(1-n\vec{\beta}\cdot\hat{r})^3R^2}\right]_{\text{ret}} + \frac{q}{c}\left[\frac{\hat{r}\times(\hat{r}-n\vec{\beta})\times\dot{\vec{\beta}}}{(1-n\vec{\beta}\cdot\hat{r})^3R}\right]_{\text{ret}}. \tag{9}$$

The first term is the so-called near-field term and it is just a minor correction to the observed field in the far-field because of its scaling with R^{-2}. For $\beta = 0$ it reduces to the Coulomb's Law for a point source. The second term, the radiation term, scales with $1/R$. It depends on the time derivative of $\vec{\beta}$ and shows that the radiation comes from the acceleration of the charged particles.

Formula 9 is a continuous formulation and therefore difficult to apply in Monte-Carlo simulations. Including the idea of splitting a particle track into sub-track, a discrete formulation for the electric field can be derived.

One can calculate the time-average electric field over the time-scale Δt where adequate choice of Δt is dictated by the time resolution of interest. As long as Δt is defined to be significantly longer than the time-scale of the acceleration process, the details of of the acceleration process are negligible. The time integral for one starting (1) and stopping point (2), taking into account the conversion of the retarded emission time t' to the observer time $t = t' + nR/c$, with $t' = t_{1/2}$ is given by:

$$\int \vec{E}(\vec{x},t)\mathrm{d}t = \pm\frac{q}{c}\left(\frac{\hat{r}_{1/2}\times(\hat{r}_{1/2}\times\vec{\beta}^*)}{(1-n\vec{\beta}^*\cdot\hat{r}_{1/2})R_{1/2}}\right). \tag{10}$$

The used parameters are illustrated in Fig. 10. The simplest acceleration process is an instantaneous acceleration of a particle from rest at a time $t' = t'_0$ to a velocity $\beta = \beta^*$, or analogously the deceleration of a particle from the velocity $\beta = \beta^*$ to rest. One can define the electric field from such events as $\vec{E}_\pm$ where the acceleration vector $\dot{\vec{\beta}}$ can be

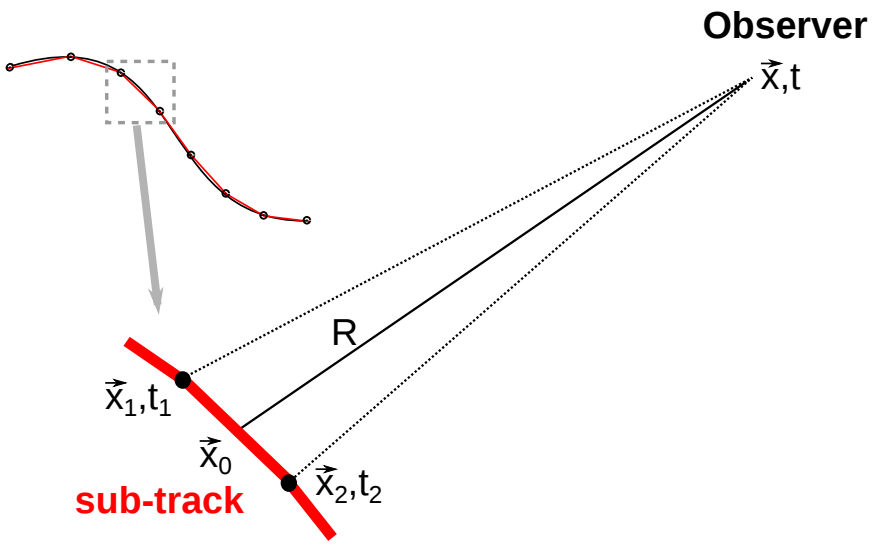

Figure 11: Sketch for defining parameters for the ZHS formalism to describe the particle track and the observer position.

parallel to the velocity vector in the case of acceleration $(+)$ or anti-parallel to the velocity vector in the case of deceleration $(-)$. Here, the velocity vector $\vec{v}$ is defined as $\vec{v} = \frac{\vec{x}_2 - \vec{x}_1}{t_2 - t_1}$. One can connect these events with "starting points", "stopping points" of particle tracks or "creation" and "destruction" of a particle. Since the time-integrated electric field is finite, one can calculate the time-averaged electric field over the chosen time scale Δt:

$$\vec{E}_{\pm}(\vec{x}, t) = \pm \frac{1}{\Delta t} \frac{q}{c} \left(\frac{\hat{r}_{1/2} \times (\hat{r}_{1/2} \times \vec{\beta}^*)}{(1 - n\vec{\beta}^* \cdot \hat{r}_{1/2}) R_{1/2}} \right). \tag{11}$$

One can reproduce physical situations like synchrotron and transition radiation correctly with this approach [52].
But in the limit of very low frequencies, which corresponds to that the assumption of being in the far-field is not valid anymore, as well as close to Cherenkov angle the resulting electric field from formula 12 goes to infinity. In case of a particle track close to the Cherenkov angle, the calculation of the radio emission using the endpoint formalism becomes numerically unstable (goes to infinity) and a ZHS-like calculation becomes necessary (fallback). Then one can use the middle of the track $\vec{R}_m = 0.5 \cdot (\vec{R}_1 + \vec{R}_1)$ in the calculation of the electric field as position vector for the track ("ZHS-like"):

$$\vec{E}_{\pm}(\vec{x}, t) = \pm \frac{1}{\Delta t} \frac{q}{c} \left(\frac{\hat{r}_m \times (\hat{r}_m \times \vec{\beta}^*)}{(1 - n\vec{\beta}^* \cdot \hat{r}_m) R_m} \right) \tag{12}$$

3.1.2 The ZHS formalism

The original ZHS formalism [53] reproduces the radio emission from moving charges in the frequency-domain, but later the formalism was adapted for applications in the time domain [54]. A particle track is completely defined by two limiting times t_1 and t_2, the velocity along the track $\vec{v}$ and the position vector to an arbitrary point of the track $\vec{x}_0$. Starting with Maxwell's equations, one can derive the vector potential of a distribution of source charges.

Assuming an observation at large distances from the source leads to the following vector potential $\vec{A}(\vec{x}, t)$:

$$\vec{A}(\vec{x}, t) = \frac{\mu}{4\pi} \frac{q}{R} \frac{\vec{v} - (\vec{v} \cdot \hat{r})\hat{r}}{|1 - n\vec{\beta} \cdot \hat{r}|}. \tag{13}$$

The detailed derivation of the formula is shown in [54]. Here, the fraction $\frac{\vec{v}-(\vec{v}\cdot\hat{r})\hat{r}}{|1-n\vec{\beta}\cdot\hat{r}|}$ can be interpreted as the projection of the displacement vector onto a plane perpendicular to the observation direction. The enumerator describes the velocity of the track perpendicular to $\vec{v} - (\vec{v} \cdot \hat{r})\hat{r}$, with $\hat{r}$ representing the direction of the line-of-sight to the observer. The used parameters are illustrated in Fig. 11.
In contrast to the endpoint formalism, ZHS describes the radiation as arising from the straight track itself (not the acceleration at the ends of the tracks). As long as the acceleration and the deceleration at the end-points of a track happen in a shorter time than the particle is moving with a constant velocity, the emission from the starting and stopping point of the track is negligible. The ZHS formalism builds on the Fraunhofer approximation, i.e., tracks have to be subdivided such that they are small with respect to the wavelength of interest and the distance between source and observer, so that the coherence condition is fulfilled. In addition the tracks must be much smaller than the distance from the radiating particle to the observer, so that the angle to the observer does not change along the track. Unlike the endpoint formalism, for low frequencies as well as close to Cherenkov angle the formula 13 gives a finite answer, but the formula is only valid in the far-zone region.

3.1.3 Application in Monte-Carlo simulations and in the interpretation of measured data

A “full” MC simulation of a particle shower tracks individual particles separately. In detail, the particle trajectory is split up into straight sub-tracks to take into account the propagation and interactions of the particles. The radio emission from each particle sub-track can then be calculated individually taking into account coherence effects at the observer’s position.
In that way, the endpoint formalism is applied in CORSIKA [55], a state-of-the-art simulation code to simulate air showers, within the CoREAS module [56], a plug-in which can be selected for a CORSIKA simulation run.
In an equivalent way, the ZHS formalism is built into the AIRES code [57], leading to ZHAireS [58].
The results of the two independent Monte Carlo simulations agree with each other, but just within their limitations to the far zone, away from low frequencies. It could be shown that the two approaches are mathematically equivalent [59, 60]. Nevertheless, a study of their validation in the context of the calculation of a radio signal from particle showers is missing since the mathematical equations differ.

3.2 EXPERIMENTS FOR AIR SHOWER DETECTION

As already mentioned in the introduction, the radio detection of air showers rapidly evolved in the last decade [61]. The second generation of digital radio detection experiments has

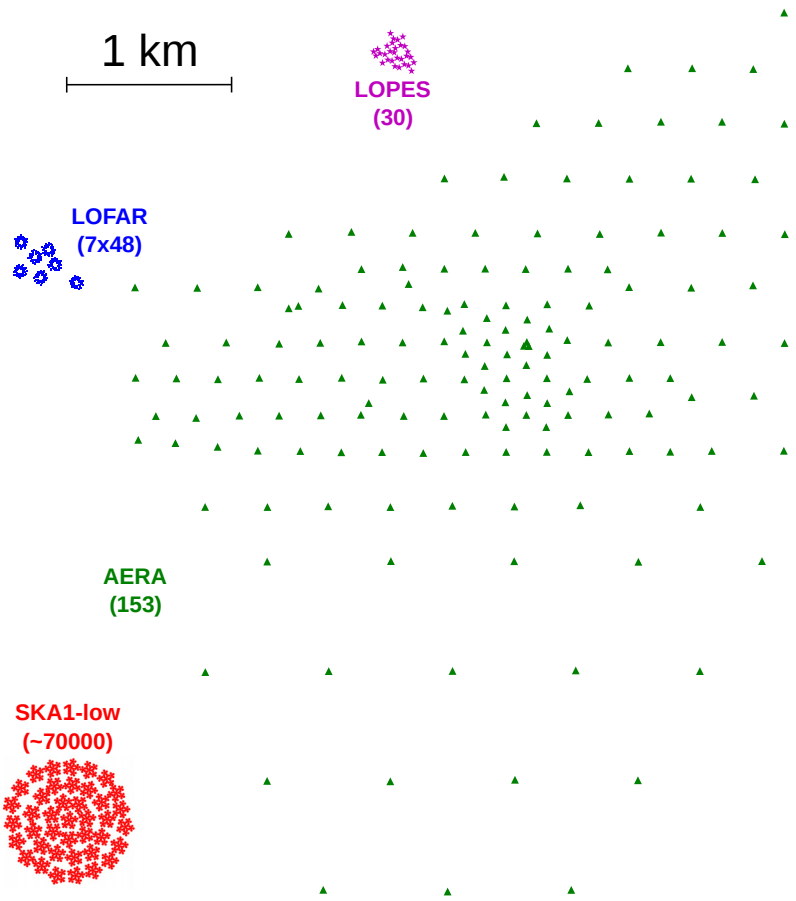

Figure 12: Some digital radio detection experiments (plotted on the same scale). Each symbol represents one radio detector. The number in brackets denotes the total number of antennas typically used for cosmic-ray detection.

been already established. There exist two different, but complementary approaches in designing radio arrays: One approach is to set up an antenna array on a large area with antenna distances as large as possible. This is done for example at AERA (see section 3.2.2) with its 150 antennas on an area of about 17 km^2 aiming at high statistics for high energetic air showers. The other approach is to establish very dense arrays covering a small area, but with a large number of antennas. This approach is used in the LOFAR experiment, which has only an area of about 0.2 km^2 and is enabled for cosmic ray detection. This experiment is aiming at a better understanding of the radio emission physics and the interpretation of the single measured air-shower events. Some arrays for radio detection of cosmic rays are shown as compilation in Fig. 12.

3.2.1 LOPES

The LOFAR Prototype Station (LOPES) [62] consists of 30 inverted V-shaped dipole antennas set up as an array of an area of about 200 $\times$ 200 m^2. It was sensitive to radio signals

from air showers in the frequency band of $40 - 80$ MHz. The radio array was deployed on the KASCADE field and triggered by the KASCADE-Grande experiment [63] at the site of the Karlsruhe Institute of Technology (KIT) in Germany. During its operation time from 2003 to 2013 and beyond, it could establish and prove many concepts for modern radio detection. For example, it could be demonstrated that radio emission by air showers is coherent and dominated by the geomagnetic effect [64]. In addition, it could be shown that during thunderstorms strong electric fields have a significant effect on the radio signal [65] as well as that the depth of the shower maximum can be determined by the lateral distribution of the radio signal [66]. It was also the first experiment which made the proof-of-principle of digital radio interferometry [64].

3.2.2 AERA

The Auger Engineering Radio Array (AERA) [67] is the radio extension of the Pierre Auger Observatory, located in Argentina. With its 150 antennas of different types (log-periodic dipole antennas and butterfly antennas) distributed on an area of $17\,\mathrm{km}^2$, it is the world's largest radio detector for measuring air showers. It is aiming at measuring cosmic rays of energies above 10^{17} eV. The antennas are sensitive to frequencies from 30 to 80 MHz. One of the great achievements of this experiment is being the first one which proved a contribution from the charge-excess to the radio signal of an air shower [42]. It could also be shown that the radiation energy reconstructed by air shower simulations can be used as a cosmic-ray energy estimator and that is scales quadratically with the cosmic-ray energy as expected for coherent emission [46].

3.2.3 ANITA

ANITA (Antarctic Impulsive Transient Antenna) is a balloon-borne experiment. Up to now it had three flights over Antarctica, while a fourth one is planned for the end of 2016. The balloon's payload consists of 32 or 48 horn antennas as shown in Fig. 21 which are sensitive in a frequency band of $200 - 1200$ MHz. At these frequencies the Cherenkov cone becomes visible, which requires specific geometries to measure a radio signal from an air shower. The Cherenkov cone of the shower must hit the antennas, directly or via a reflection on the ground. Also a transmitted radio signal from a particle cascade initiated in the Antarctic ice is detectable. The main goal of the ANITA experiment is to detect ultra-high-energy neutrinos. Unlike charged cosmic rays or photons, due to their low cross section most neutrinos do not induce a particle shower in the atmosphere, but just pass without any interaction. Since the density is higher and the interaction gets more likely than in the atmosphere, some neutrinos initiate a particle shower below ground, for example in ice. The non-detection of neutrinos so far led to an upper limit at energies of $E_\nu > 10^{19}$ eV. In the first ANITA flight already, sixteen cosmic ray events of mean energy of $1.5 \cdot 10^{19}$ eV were measured [68] which is the highest cosmic-ray energy measured by radio detection so far.

3.2.4 LOFAR

The Low Frequency Array (LOFAR) [69] is one of the pathfinders for the SKA (see Chapter 7) and was planned as a radio astronomy experiment. It is a new-generation radio telescope, situated in the North of the Netherlands with satellite stations distributed over Europe. The antenna array is organised as stations with 96 low-band antennas (LBA, slanted dipole antenna, $10-90\,\mathrm{MHz}$) and 48 high-band antennas (HBA, $110-240\,\mathrm{MHz}$) each. There are many different observation modes and some of them can run simultaneously, such as the air shower measurements which can run in parallel with astronomical observations. The LOFAR core consists in total of 24 stations on an area with a diameter of about 2 km. The central 6 stations placed close together on the so-called superterp. Other stations are positioned around this center with increasing distances to each other [70].
To enable LOFAR to be used for cosmic-ray detection it was extended with a scintillator array, the LOFAR Radboud Air Shower Array (LORA) [71]. These are 20 particle detectors covering the superterp area (compare to Fig. 13) which provide a trigger for the radio antennas for air showers above $10^{16}\,\mathrm{eV}$. The information provided by LORA is also needed for the reconstruction of the arrival direction, the shower core position on ground and a first energy estimate of the shower. LOFAR is the densest antenna array used for cosmic-ray detection so far which makes a deep test of models, e.g. for the distribution of radio amplitudes [72], possible. Therefore, it is also possible to perform a very detailed study on the lateral distribution function of the radio emission. One of the last great achievements was the mass composition measurement by LOFAR which estimated a light mass contribution of elements in the energy range of $10^{17}-10^{17.5}\,\mathrm{eV}$ [73]. Since the data by the HBAs are more challenging to analyse, just the LBA data, in particular of the outer LBAs, were used for this study. In addition, the operational frequency band of the LBAs is limited from 30 MHz to 80 MHz in the air-shower analysis because the lower end of the LBA frequency range is overwhelmed by strong ionospheric reflections of terrestrial radio-frequency interference (RFI) while its higher end is dominated by the commercial FM radio band.

3.2.5 SKA-low

The low-frequency array of the future Square Kilometre Array (SKA-low) will be located in West-Australia. Phase 1 of the low-frequency part of SKA (SKA1-low) will be build in 2018 and completed in 2023. The first operation is planned for 2020. The core of low-frequency array will consist of almost 70.000 antennas on an area of less then $0.44\,\mathrm{km}^2$ in a circle with a diameter of 750 m. Therefore, it will be the densest antenna array of the world, sensitive to frequencies from $50-350\,\mathrm{MHz}$. With some technical design modifications as a deployment of a simple particle-detector array for triggering, SKA1-low can be easily enabled for cosmic ray detection. Since a simulation study of the ability to measure the mass composition with SKA1-low with extreme precision is one part of this thesis, more details about SKA1-low can be found in Section 7.

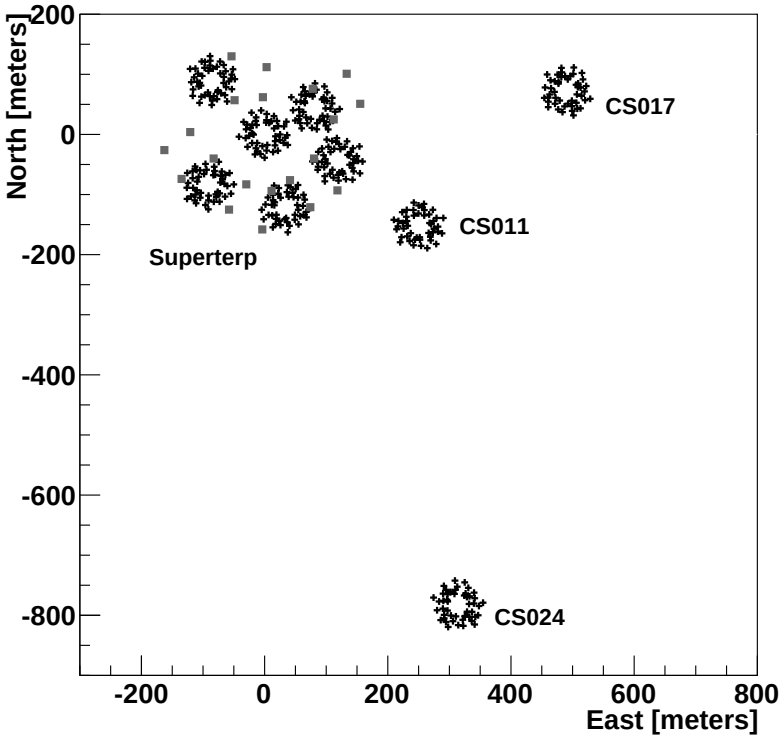

Figure 13: Part of the LOFAR core [74]. Only the LBA antenna positions in the outer rings of each station are indicated with a "+". The gray squares represents the positions of the LORA particle detectors.

3.2.6 Laboratory experiments

Several accelerator experiments, e.g. at the Stanford Linear Accelerator Center (SLAC), have been preformed to study the radio emission from particle cascades by the Askaryan effect under laboratory conditions. They could show that the emission mechanism is well understood for electromagnetic showers in different dielectric media as sand [39] or ice [40, 41] and worked as a validation of the concepts of measuring electromagnetic shower in ice for the ANITA experiment. The Askaryan effect could be validated as emission mechanism producing strong coherent pulses whose polarisation, field strength and timing followed the theoretically predicted behavior.

3.3 ABILITY TO PREDICT RADIO EMISSION FROM A PARTICLE/AIR SHOWER USING MICROSCOPIC SIMULATIONS

The interpretation of the air-shower measurements of all these antenna arrays is based on predictions from simulations (see Section 3.1.3). Thus, a full understanding of properties of the pulse as a function of time is crucial for the interpretation of the data. The state-of-the-art simulation codes, CoREAS and ZHAireS, both basing on microscopic approaches, the endpoint and the ZHS formalism respectively, calculate the radio emission from air showers on the basis of full Monte-Carlo simulations. In a former simulation study it could been

shown that their predictions agree within $\approx$ 20% with each other [75]. This deviations is likely to be originated in the underlying air-shower program, AIRES and CORSIKA, e.g. by the included hadronic interactions models or the energy cuts for the the simulations of the particle cascade.
Also a quantitative comparison to measured air-shower data showed a good agreement with the prediction from simulations. For AERA data, simulation sets for a specific radio events were produced, with varying the input parameters within the uncertainties of the measured arrival direction, core position and particle energy reconstructed from the Auger particle water detectors [76]. The comparison of the simulations and the data showed a good agreement within the uncertainties, accordingly to the input parameters. The absolute scale of the radio emission could be reproduced within $\approx$ 20%. In addition, the comparison of measurements of the LOPES and the Tunka-Rex experiments underline the good quantitative prediction of the radio signal by the state-of-the art simulations [77, 78]. Even more impressive, the LOFAR experiment performed a comparison of the predictions from CoREAS simulations to the measured two-dimensional lateral distribution functions of radio events [74]. Their agreement were even more impressive, showing how extremely detailed the simulation can reproduce the radio signal from an air shower.
For future radio arrays as SKA1-low, this ability to predict the radio signal in such extreme details will become even more important since SKA1-low will sample the radio footprint of an air shower with extreme precision and it will be therefore sensitive even to the smallest structures.

As an important complementary test for the ability of the radio-emission codes to describe measured data, laboratory experiments must be performed. These measurements are affected by different systematic uncertainties than air shower experiments and provide a comparison between data and simulations independent of hadronic interactions models, unknown mass-composition of the primary particles or unknown geometry. With dedicated particle-beam experiments at electron accelerators the study of the radio emission by a well-defined and pure electromagnetic showers with known primary particle type and primary energy is possible. In addition, a direct comparison of data to the results using the ZHS and the endpoint formalisms for the same shower can be performed, independent on the underlying air shower simulation programs, CORSIKA and AIRES, which differ in the treatment e.g. of the hadronic interaction in the shower simulation. Furthermore, in the past only the Askaryan effect was studied in laboratory experiments.

The SLAC T-510 experiment, which will be introduced in Chapter 4, could demonstrate that microscopic simulations using the ZHS and the endpoint formalisms describe all aspects of the radio signal from a electromagnetic particle shower, quantitatively as well as qualitatively.
For this experiment, the preparation and performance of the simulation study for the prediction of the radio emission from the particle shower on the basis of microscopic simulations were carried out in the context of this work. The details can be found in Chapter 5. The interpretation of the comparison between measured data and simulation results as well as follow-up analyses based on simulations are presented in details in Chapter 6.

4 TESTING PREDICTIONS FOR RADIO EMISSION FROM PARTICLE SHOWERS UNDER LAB CONDITIONS

The interpretation of measured air shower data via radio detection relies on the understanding of the radio emission from extensive air showers. Established microscopic calculations using the endpoint and the ZHS formalisms as already introduced in section 3.1 are based on first principles and have no free parameters. Both are based on well-known electrodynamics and it could be shown that they are mathematically identical within certain limitations [60]. But nevertheless, a validation by a laboratory experiment with different systematic uncertainties than air shower measurements is needed.

For that, e.g. an electron accelerator can be used to produce an electromagnetic particle shower. Since the tracks of secondary particles in an "air" shower can reach up to several hundreds of meters, a medium denser than air has to be used to host the shower. To also account for the (geo-)magnetic effect, a magnetic field with much higher strength than the Earth's magnetic field has to be induced to deflect the charged particles in the target as done in an air shower.
In addition, even if a recent comparison of measured air shower data and results of microscopic calculations confirms the absolute scale of the radio emission [79, 78], this comparison is limited due to uncertainties in the air shower cascade itself like the mass composition of the cosmic rays. A fixed target experiment would provide a known beam geometry and electromagnetic shower composition and can therefore confirm the absolute scale of the radio emission predicted by microscopic calculations with different systematic uncertainties.

In 2014, such an experiment was performed at the SLAC National Accelerator Laboratory using a high density polyethylene (HDPE) target placed in a strong magnetic field (see Fig. 14). Beside the first observations of radio emission from transverse currents induced in a secondary cascade by a magnetic field in dense media (so far just the Askaryan effect has been observed in previous experiments in ice, silica sand and in rock salt as introduced in Section 3), also both formalisms for calculating the radio emission from particle showers could be validated within the experimental systematic uncertainties by setting up a detailed simulation study, which was performed as part of this thesis (see Chapter 5).

4.1 EXPERIMENTAL SETUP OF THE T-510 EXPERIMENT

In January/February 2014, the T-510 experiment was performed at the End Station Test Beam (ESTB) in End Station A (ESA) at the SLAC National Accelerator Laboratory.

4.1.1 The SLAC electron beam

The SLAC electron beam was shot into a plastic target with an energy per electron of about $4.35 - 4.55\,\mathrm{GeV}$ [80]. First, the electrons passed through 2 radiation lengths of a lead

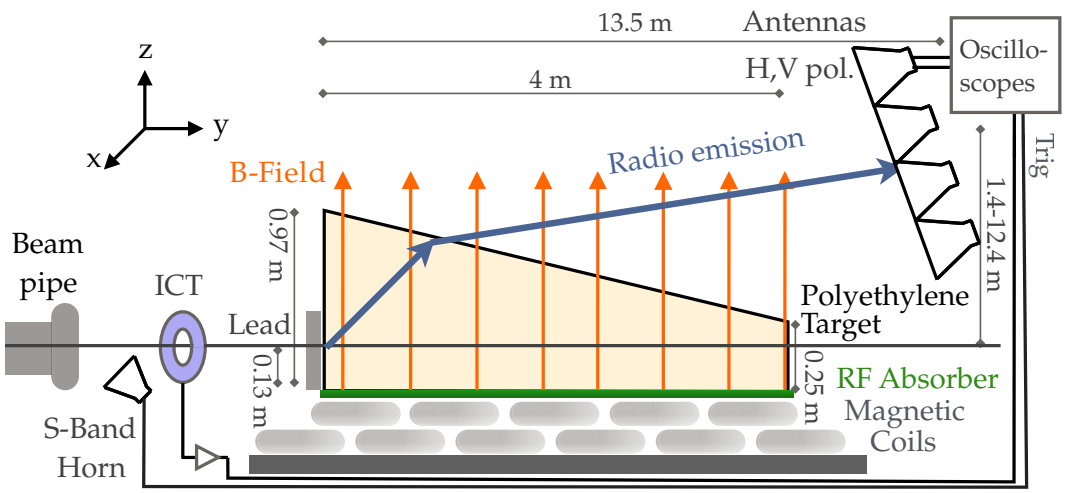

Figure 14: Sketch of the experimental setup including the antenna tower position and the geometry for the signal propagation. Taken from [80] (slightly modified).

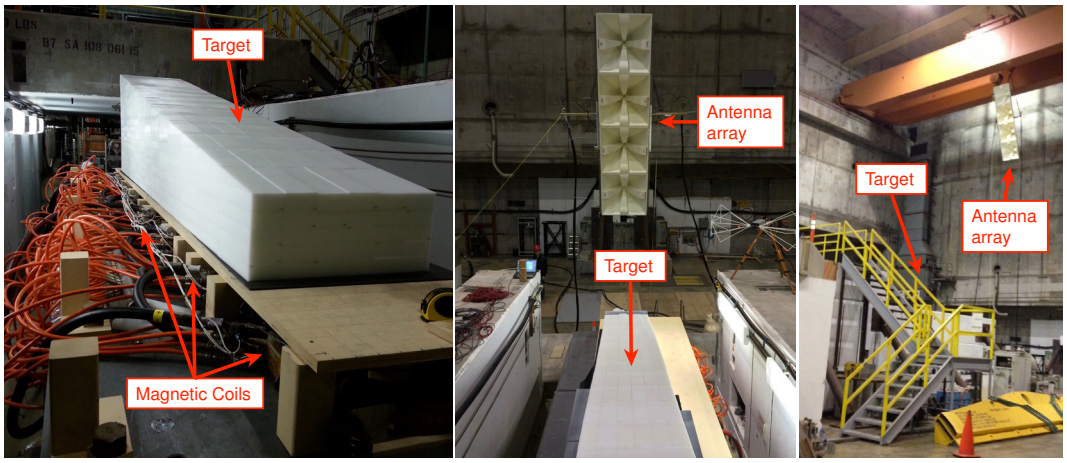

Figure 15: Left: The HDPE target on top of the magnetic field coils which are water-cooled (orange tubes). Center: The quad-ridged horn tower attached to a crane, shown in a position close to the target. Right: The tower position for one data-taking run (12.4 m above the beam, and 13.5 m from the beam entrance to the target). Taken from [80] (slightly modified).

pre-shower target before entering the dielectric target where a shower of secondary particles evolved. The measured mean bunch charge was 131 pC, with a shot-to-shot standard deviation of 3 pC and 2% systematic uncertainty. The particle shower generated in the target is equivalent to a shower induced by a primary cosmic ray with an energy of about $4 \cdot 10^{18}$ eV [80].

Measurements of the beam current:

To record the total charge in each bunch shot into the target, an integrated charge transformer (ICT) was placed between the end of the beam pipe and the target. Its accuracy is given within 3% for bunch charges larger than 100 pC. The charge distribution measured by the ICT for a typical run is shown in Fig. 16 (left). It has a mean of 131 pC and a standard deviation of 3.3 pC [81].

In addition, a high-frequency S-band ($2 - 4$ GHz) horn antenna measured the transition radiation as the beam exited the beam pipe. The intensity of radiation scales with the total

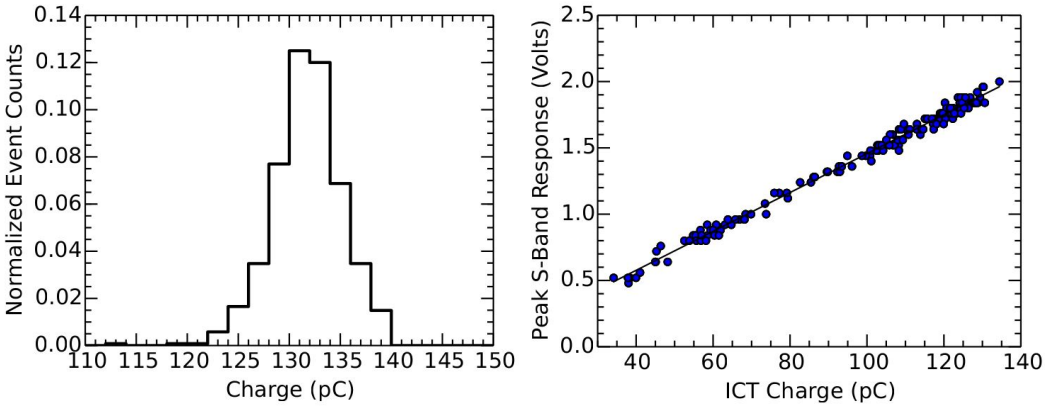

Figure 16: Left: Shot-to-shot beam charge distribution for a typical data taking run. Right: Peak amplitude recorded in the S-band ($2-4$ GHz) horn compared to the bunch charge [81].

charge (s. Fig 16, right). This provides a global trigger for the measurement system (s. Fig. 14) as well as the shot-to-shot relative calibration of the beam charge.

4.1.2 The High Density Polyethylene target

To reduce the size of the particle shower to laboratory scales (tracks of secondary particles could otherwise reach up to several hundreds of meters in air), a target made out of dense material is needed in which the shower development can take place.

The target was 3.96 m long, 0.96 m tall, and 0.60 m wide, large enough to contain the majority of the particles in the shower (compare to Fig. 17). Just a few low energetic particles can escape out of the target. It was built up of single bricks made out of 1500 kg of High-Density Polyethylene (HDPE), each of a size of 5.08 cm $\times$ 10.16 cm $\times$ 30.48 cm. In the simulation study performed for this experiment (see Chapter 5) it is assumed to be a solid block and possible small gaps between the single bricks are neglected. This can effect the strength of the electric field as well as the timing of the signal and can lead to additional but minor systematic uncertainties.
To reduce internal reflections, the target was positioned on a RF absorbing blanket. The relative absorption in dependence of the frequency is shown in Fig. 18. In addition, several pieces of a RF absorber foam were placed at both sides of the target and at the exit surface of the target, so that the measurement only accounts for radiation coming trough the upper surface of the target. To avoid internal reflections of the signal, this surface was chosen to be slanted by an angle of 9.8° below the horizontal. The index of refraction of $n_{\mathrm{HDPE}} = 1.52$ corresponds to a Cherenkov angle inside the target of 49°, the angle of the out-coming rays with respect to the horizontal is about 29.8°. This leads to an expected position of the Cherenkov cone on the vertical axis at about 6.5 m above the beam line at a distance of 13.5 m from the entry point of the beam.

The electron beam enters the target at 12 cm height above the target bottom surface, after passing through a 1.2 cm thick lead plate. The lead acts as a pre-shower target with a width of two radiation lengths ($X_{\mathrm{rad,lead}} \approx 0.6$ cm) and therefore it reduces the necessary overall length of the target to include the particle shower.

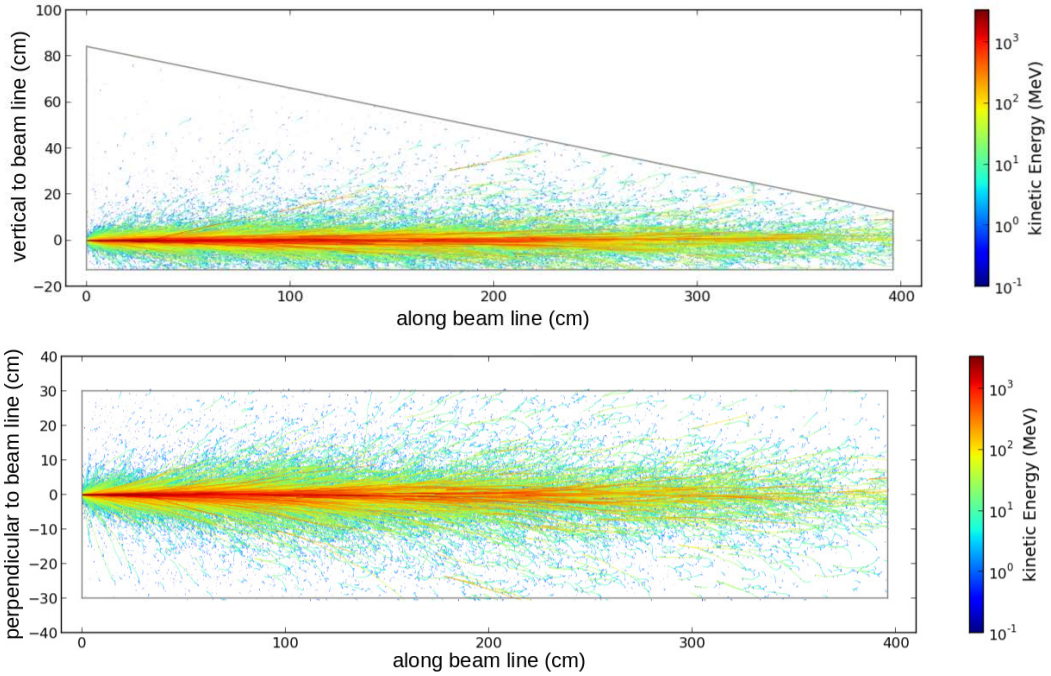

Figure 17: Example simulation with 100 primary electrons of an energy of $E = 4.35\,\text{GeV}$ and a magnetic field strength of 2400 G for the particle distribution in the target as function of their kinetic energy (color-code): Top: View from the side of the target. Bottom: View from the top of the target.

4.1.3 The magnetic field

To provide an uniform magnetic field in the vertical direction with a field strength up to 970 G, fifteen water-cooled solenoids were staggered in two rows under the target [80]. The bottom row had eight coils placed side-by-side, while the top row included seven coils that covered the full length of the target (compare with Fig. 19). The outside diameter of each coil is 60 cm, the inside diameter 48 cm and the height is 8 cm. Due to the water cooling, a maximum current of 800 A could be reached in each coil. They were arranged in 3 groups of five each connected in series and supplied with a current with reversible polarity. So, a value of 2400 A was given as a system current. A map of the magnetic field strength, scaled to a maximum induced current of 2400 A, is shown in Fig. 20. Because the magnetic field component vertical to the beam line falls off near the edges of the coils, the target was placed with the target edge in the middle of the first coil. The strength of the magnetic field along the beam was chosen to be strong enough to bring the expected radiation intensity from the magnetic effect and the one of from the Askaryan effect to the same order of magnitude (compare to Sec. 4.2).

Measuring the magnetic field map:
In the simulations of the T-510 experiment, the measured, three-dimensional magnetic field map, as shown in Fig. 20 (left) is included. The initial magnetic field map was measured at beam height with a Hall probe in a grid with 5 cm spacing at a magnetic coil current of 2530 A while the T-510 data were taken at 2400 A. To check for the linearity of the magnetic field strength with the applied current, the magnetic field was measured at several

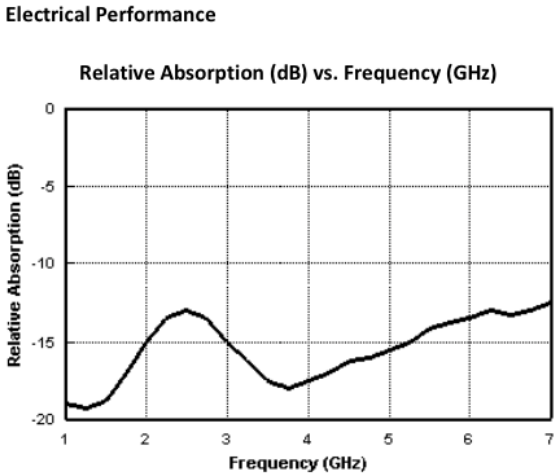

Figure 18: Relative absorption by the RF absorbing blanket in dependency of the frequency (figure provided by MWT Material, Inc.).

Figure 19: Picture of the staggered coils to produce a strong and uniform magnetic field in the vertical direction to the beam line.

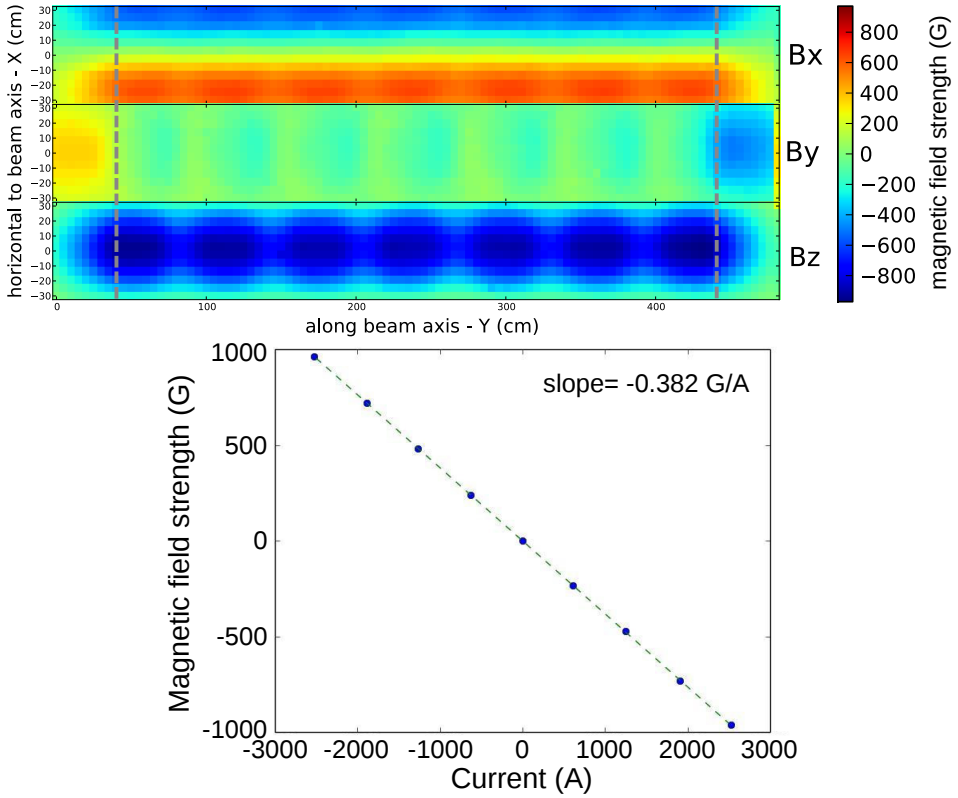

Figure 20: Top: Measured three-dimensional magnetic field map for a current of 2400 A (in 5cm×5cm squares) which is included in simulations. The gray lines mark the target area. Bottom: Measurement of the linear dependence of the magnetic field strength on the applied current [82].

different currents between −2400 A and 2400 A, as shown in figure 20 (bottom). A linear fit to the data points returns a scaling factor m for rescaling the complete magnetic field map to the desired strength in dependence on the applied current. This results in the following dependency usable to set the magnetic field strength within the simulation:

$$B' = B + m \cdot \Delta I \tag{14}$$

with $B = 2530$ A as the current at which the magnetic field map was measured, the scaling factor $m = -0.382$ G/A, $\Delta I = 2530\,\text{A} - I_{\text{data}}$ as the change in current and B' as the resulting magnetic field strength.
Along the beam position, the average magnetic field in the vertical direction is 845 G, and the RMS variation is 72 G (root-mean-squared variation). The peak magnetic field strength is measured to be 970 G to which will be referred in the following. From laboratory calibration tests, the Hall Probe average systematic error is known to be 5.73%.

4.1.4 The horn antennas

To measure the vertically and horizontally polarised component of the electric field produced by the particle shower, four dual-polarization, quad-ridged horn antennas [83] provided by the ANITA collaboration (see Chapter 3.2.3), each with an opening of 1 m × 1 m, were arranged on a tower. The antenna tower was placed at the far wall of ESA in a

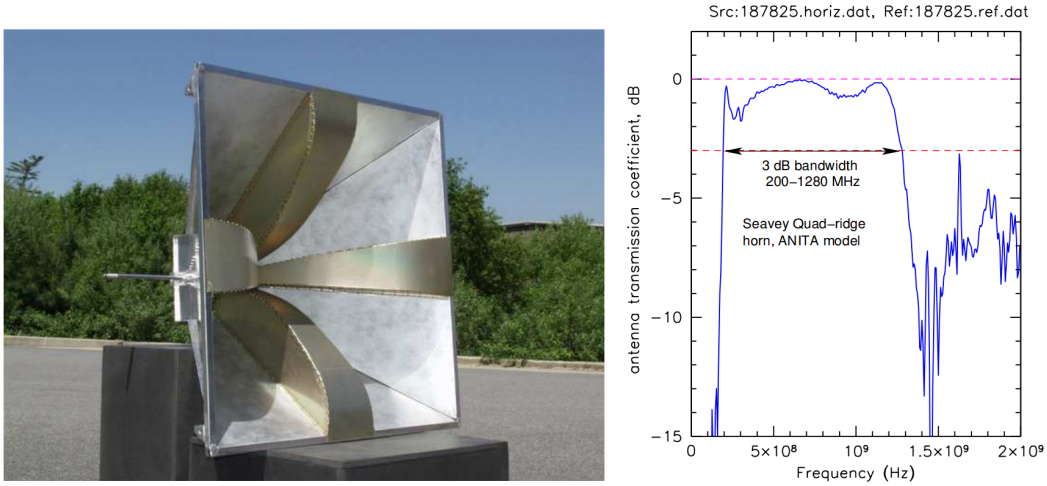

Figure 21: Left: A photograph of an ANITA quad-ridged dual-polarization horn. Right: A typical measured transmission coefficient for signals into the quad-ridged horn as a function of radio frequency [83].

maximum distance of $L = 13.5\,\text{m}$ from the entry point of the beam in the target to fulfill the condition for full coherence of the radio emission according to $kL \gg 1$, with the wavenumber $k = 2\pi nf/c$, the frequency f and the index of refraction n [84].
Since the radiation of the particle shower is expected to peak at the Cherenkov angle of 29.8°, the tower was tilted at 19.6° towards the target for a better alignment with the expected radiation escaping through the upper target surface. With the help of an overhead crane the antenna tower could be moved at any time, so that it was possible to sample the electric field at many positions at vertical distances between 1.5 m and 12.5 m with respect to the beam height.
The antennas were sensitive in a frequency band from $200 - 1200\,\text{MHz}$ (compare to Fig. 21). The induced signals were digitised with a sampling rate of 5 GHz. In the analysis the band of $200 - 300\,\text{MHz}$ was excluded in data as well as in simulations because of uncertainties due to diffraction effects and in antenna response at low frequencies [80].

Positioning of the antennas:
As shown in Fig. 20, the magnetic field is arranged to be strongest in the vertical direction. This is chosen to have the transverse current during shower development (s. Section 3) oriented primarily along the horizontal axis. The produced radiation will then be horizontally-polarised. On the other hand, the radiation produced by the Askaryan effect due to the time-variation of the net current will be radially polarised. To differentiate the two components of the radiation, the antenna tower can now be placed on the vertical axis which is perpendicular to the beam axis and parallel to the magnetic field direction (see Fig. 22). Thus, the magnetic radiation will be observed at the antennas as being horizontally polarised, while the Askaryan radiation is vertically polarised.
The position of the antenna tower and the tilt angle of the tower were measured by a laser distance measuring equipment and digital protractors, returning a total uncertainty of the distance measurement of 0.01 cm and of the tilt angle measurement of 3°. The accuracy of the of the height measurements is about 5 cm [85]. The alignment towards the target was done using ropes.

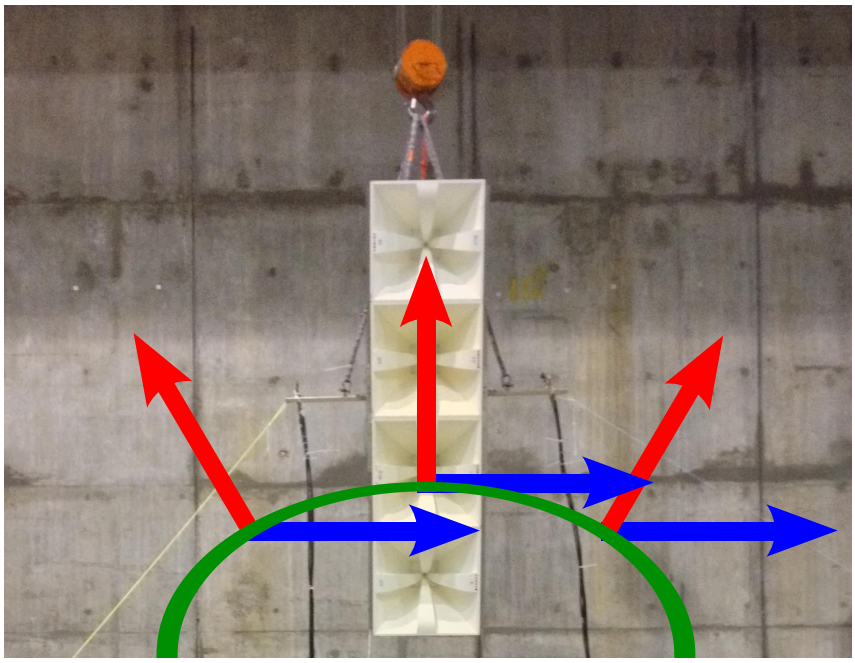

Figure 22: Positioning of the antenna tower at the Cherenkov ring (green) so that contributions of the Askaryan (red) and magnetic effect (blue) are split up in the horizontal and vertical channels of the antenna.

4.1.5 The Data Acquisition System

The Data Acquisition System (DAQ) (see sketch in Fig. 23) was triggered by a S-Band horn antenna placed near the exit of the beam pipe to register transition radiation (TR). Waveforms from the horn antennas were sampled at 5 GHz. The data acquisition system consisted of 3 8-bit oscilloscopes connected to a single router via an Ethernet connection. The router was connected to a laptop running a LabVIEW program which could control the scopes. It could simultaneously read the output of all three oscilloscopes at the same time and write them to a text file.
Every run was output into one text file per scope which contained the header with information like the charge measured by the ICT and waveform information of each channel, in addition to a time stamp.

4.2 SCALING RESULTS TO AIR SHOWERS

Since it was never one of the goals of the T-510 experiment to accurately replicate all the conditions of an air shower in the lab or to create a model system with relative field strengths arising from both magnetic and Askaryan emission comparable to those found in air showers, a direct comparison of air showers to T-510 measurements is difficult. Nevertheless, the target density, the frequencies of observation, and the magnetic field strength are scaled appropriately to relevant parameters important for air shower observations [80].

With its beam energy of $4.35 - 4.55\,\mathrm{GeV}$ and its measured mean charge of $131 \pm 3\,\mathrm{pC}$, the induced electromagnetic shower reproduces an air shower induced by an primary with an energy of about $4 \cdot 10^{18}\,\mathrm{GeV}$.

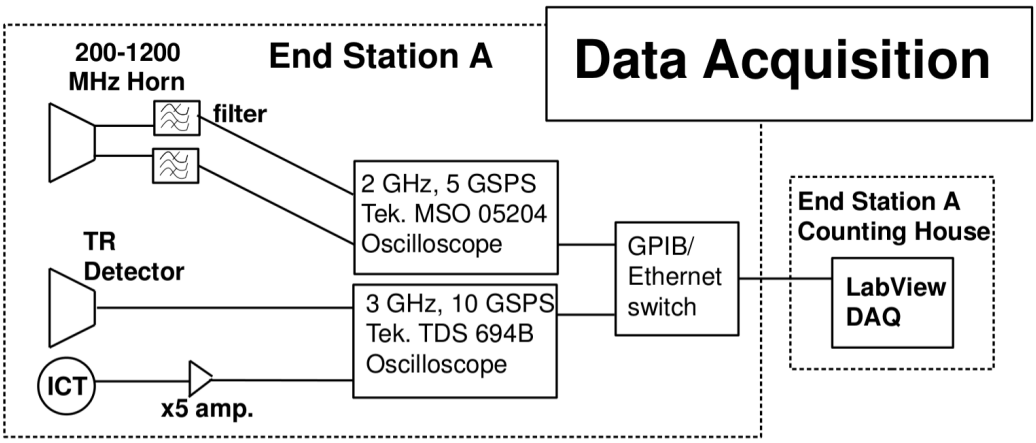

Figure 23: Data Acquisition system during data taking [86].

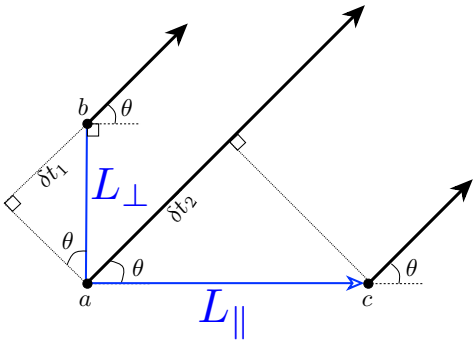

Figure 24: Sketch for defining the transverse (δt_1) and longitudinal (δt_1) coherence times [80].

In contrast to air showers, the radiation from the Askaryan effect dominates over the magnetic emission in dense media. The source of both radiation effects is the current distribution in the shower. For the Askaryan radiation, the total longitudinal current is important which depends on the total track length of particles, weighted by the charge asymmetry. The total track length scales as the radiation length or with the inverse of the density ($1/\rho$). For the magnetic radiation, the source of radiation is the total transverse current which depends on the total track length weighted by the transverse velocity, or the accumulated transverse acceleration during a radiation length. The acceleration increases with the magnetic field strength B, and the time of acceleration increases as the radiation length or $1/\rho$. Therefore, the total transverse current scales as B/ρ^2. To get a comparable ratio of source currents for magnetic emission to Askaryan emission as observed in an air shower and, therefore, to mimic the relative importance of geomagnetic radiation to Askaryan radiation in air showers, the ratio $(B/\rho^2)/(1/\rho) = B/\rho$ has to be comparable to that in air showers. Derived from an Earth's magnetic field strength of about 0.5 G and a density of the air of $1.225 \cdot 10^{-3}$ g/cm^3, the magnetic field strength should be about 1000 G to get the same magnitude for the ratio B/ρ using an HDPE target, where the shower development takes place, with a density of 0.94 g/cm^3.

The transverse delay time δt_1 and the longitudinal delay time δt_2 define the frequencies

and angles over which the radio emission of a shower is coherent. Here, the transverse delay time determines the range of frequencies where the radiation is in phase and both, the longitudinal and transverse, set the range of angles over which the radiation is coherent.
In comparison, the bandwidth of observed frequencies in T-510 is higher than the corresponding bandwidth for air shower experiments. Also the shape of the observed beam pattern depends on the Cherenkov angle and beam width, which both are different in T-510 and in air shower experiments.
One has to presume that the radiation is coherent over the transverse dimensions of the shower, $L_\perp$, which is assumed to be one twelfth of the Molière radius, R_m. The observed frequencies f have to be in the same magnitude as the time difference δt_1, as the transverse time delay between radiation coming from the shower center a and radiation coming from the edges of the shower b, arriving at an observation angle θ (compare to Fig. 24). Here, δt_1 is given as:

$$\delta t_1 = \frac{n L_\perp \sin\theta}{c}. \tag{15}$$

For observations at the Cherenkov angle, $\theta = \theta_C$, this leads to the following relation for the observed frequencies:

$$f \sim 1/\delta t_1 \sim c/(L_\perp \sin\theta_C) \sim c/(R_m \sin\theta_C). \tag{16}$$

Now, one has to consider that the density of the atmosphere is changing along the air shower, while it is fixed for T-510 experiment. For the T-510 experiment, $\sin\theta_C$ has a value of 0.8, while in air showers $\sin\theta_C$ scales with the inverse of the density. Consequently, the measurements of the T-510 experiments made at $200 - 1200$ MHz are comparable with observations of air showers in the $10 - 60$ MHz band, where experiments like AERA or Tunka-Rex operate.

5 MODELING THE RADIO EMISSION FROM A PARTICLE SHOWER FOR THE T-510 EXPERIMENT

In the context of this thesis, principle ideas, as presented in this chapter, as well as some figures and preliminary results, were already published in:

- A. Zilles for the SLAC T-510 collaboration, “Geant4 Simulations of Radio Signals from Particle Showers for the SLAC T-510 Experiment” in the proceedings 6th Acoustic and Radio EeV Neutrino Detection Activities (ARENA 2014) [87],
- A. Zilles et al.,“Modelling of radio emission in the SLAC T-510 experiment using microscopic Geant4 simulations” in the proceedings of the 34th International Cosmic Ray Conference (ICRC 2015) [88].

For the simulation of the particle shower in the target and its radiation at radio frequencies the toolkit Geant4 10.0 was used [89]. This toolkit is object-oriented and programmed in C++. It simulates the passage of particles through matter, treating their propagation and interactions. It simulates the shower development by splitting up continuous trajectories of particles into sub-tracks. The sub-tracks can be seen as straight lines with given starting and stopping points and their corresponding times. This information is used as the basis for the calculation of radio emission by particle showers (compare to Chapter 3.1.2 and 3.1.1). The simulation also includes details of the experimental setup, such as the target geometry and material, as well as the beam particles and their energy. All relevant interactions of shower photons, electrons and positrons are included (multiple scattering, ionisation, bremsstrahlung, Compton scattering, gamma conversion, photoelectric effect, pair production, annihilation).
The positions of the antennas during the measurements are given as observers for the calculation of the produced radio signal.
For data measurements as well as in the simulations the coordinate system was chosen as shown in Fig. 14. Since the electric field at an antenna position is calculated in the simulation for all three space dimension, the tilt of the antenna tower can be considered in the comparison to the measurements as a rotation of the vertical component of the simulated electric field.

5.1 IMPLEMENTATION OF THE REALISTIC MAGNETIC FIELD STRENGTH DISTRIBUTION

The measured three-dimensional map of the magnetic field strength (shown in Fig. 20) is integrated in the simulation, so that the effect of the realistic magnetic field on the emission of the radio signal can be studied.
Each component of the measured magnetic field map is read in by Geant4. The current value of magnetic field strength which affects the particle track is set depending on the

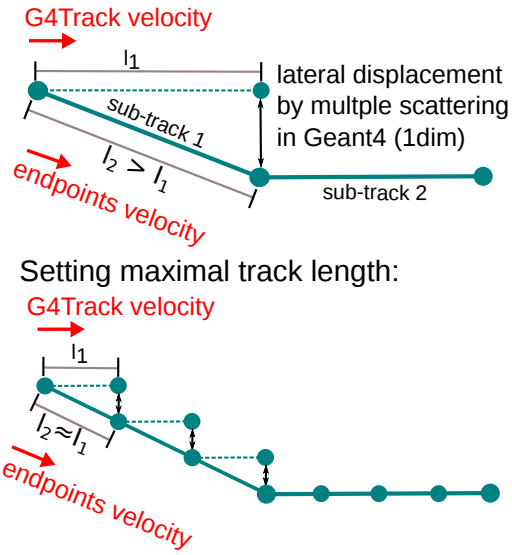

Figure 25: Handling Multiple Scattering in Geant4 on track-level and reducing its impact by setting a maximal length of the sub-track.

position of the current sub-track. Since the magnetic field strength scales linearly with the applied current [82], the strength of the field in the simulation can be controlled by the current set during the measurements. The maximum magnetic field strength during the measurements of about 970 G along the vertical axis with respect to the beam line is given by the maximum applied current of 2400 A.

5.2 REDUCING THE IMPACT OF "SUPERLUMINAL" ELECTRONS

For the calculation of the radio emission the charge of a particle, the positions of the sub-track's start- and end-points and their corresponding times are needed (compare to Sec. 3.1). On this basis the velocity and acceleration along the sub-track as well as the particle propagation direction can be reconstructed.
The information delivered by Geant4 on the track velocity and its direction cannot be used, although the G4Track velocity follows the behavior expected for a relativistic particle velocity (see Fig. 26, right). This is because the G4Track velocity represents the particle's velocity calculated at the beginning of the sub-track. But multiple scattering handled by Geant4 leads to a lateral displacement of the end-point of the sub-track. Within Geant4 this is taken into account by a relocation of the end-point of the sub-track. Details on the handling of Multiple Scattering in Geant4 can be found in [89]. On the other hand, the relocation leads to an inconsistency between the position of the particle sub-track's start- and end-point and the particle velocity along the sub-track as well as its direction. The information provided by Geant4 on the particle velocity and the direction is therefore not usable for the calculation of the radio emission using the endpoint or the ZHS formalism.
These parameters have to be calculated on the basis of positions of sub-track start- and end-point and their corresponding times: $v_{\text{sub-track}} = \frac{|\vec{x}_{\text{end}} - \vec{x}_{\text{start}}|}{t_{\text{end}} - t_{\text{start}}}$. The distribution of the calculated velocity in dependence of the kinetic energy of the particle is shown in Fig. 26 (left). One can observe that for many sub-tracks the particle velocity exceeds the velocity of light

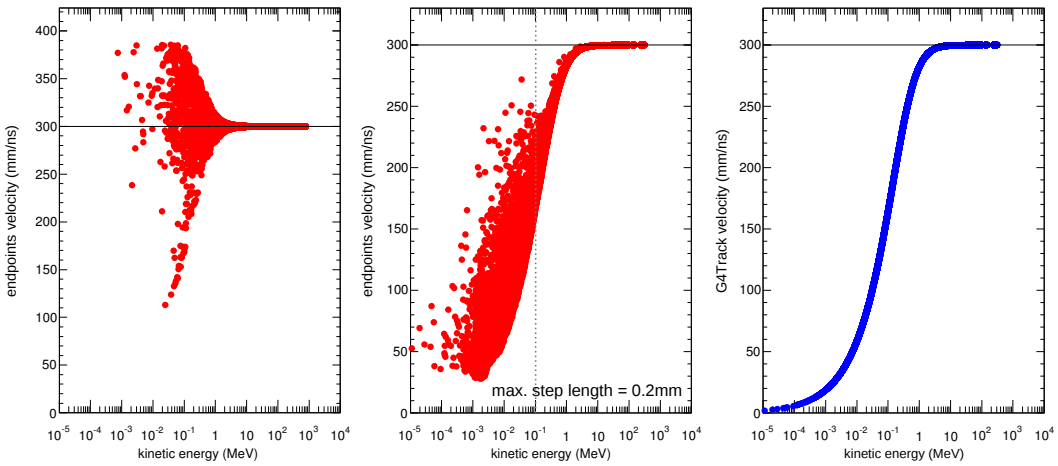

Figure 26: Simulation with 1 e^- as primary with an energy of 4.35 GeV: A comparison of different approaches to obtain the particle velocity along a sub-track vs. its kinetic energy is shown. The velocity can be calculated from the start- and end-point information of a sub-track (left: no maximal step length set, center: maximal step length of 0.2 mm), or the velocity can be obtained directly from Geant4 (right). The horizontal line in each graph marks the value of the velocity of light in vacuum.

in vacuum of $c = 300$ mm/ns since the length of the sub-track gets longer as demonstrated in Fig. 25. The artificial velocities larger than the speed of light result also from the lateral displacement by multiple scattering.
To reduce this effect due to lateral displacement, the internal Geant4 function of setting a maximal step length is chosen. Since the total sub-track length is shorter, also the lateral displacement for this sub-track decreases. A value of 0.2 mm was found to be a valid sub-track length. In this case, the effect of having a velocity along the sub-track higher than expected from a relativistic velocity is still observable for low energetic particle. Since their contribution to the total radio signal is negligible ($< 1\%$), these particle are skipped in the calculation by setting an energy cut of $E_{\text{kin}} > 0.1$ MeV as indicated with a line in Fig. 26 (middle).

5.3 IMPLEMENTATION OF THE FORMALISMS IN THE SHOWER SIMULATION

The simulations include the calculation of the radio signals produced by the particle showers in the target based on the sub-track positions $(\vec{x}_{\text{start}}, \vec{x}_{\text{end}})$ and times $(t_{\text{start}}, t_{\text{end}})$ given by Geant4. Each sub-track contributes to the calculation of the electric field or to the vector potential using the endpoint and ZHS formalisms which run in parallel. This provides a one-to-one comparison so that shower-to-shower fluctuations are not an issue in the comparison of the results for the two formalisms. In the simulation, a 400 ns time window for the arrival of the signal at the antenna is chosen starting with the time at which a signal originated from the entry point of the beam to the target would reach the antenna. The sampling rate for the simulated time traces is set to a value of 100 GHz.

The shower simulations are done by injecting 5000 electron primaries with an energy of $4.35 - 4.55$ GeV each. Due to coherent emission of the radiation, the resulting electric field can then be scaled up linearly to the measured charge of 131 pC which is checked for this

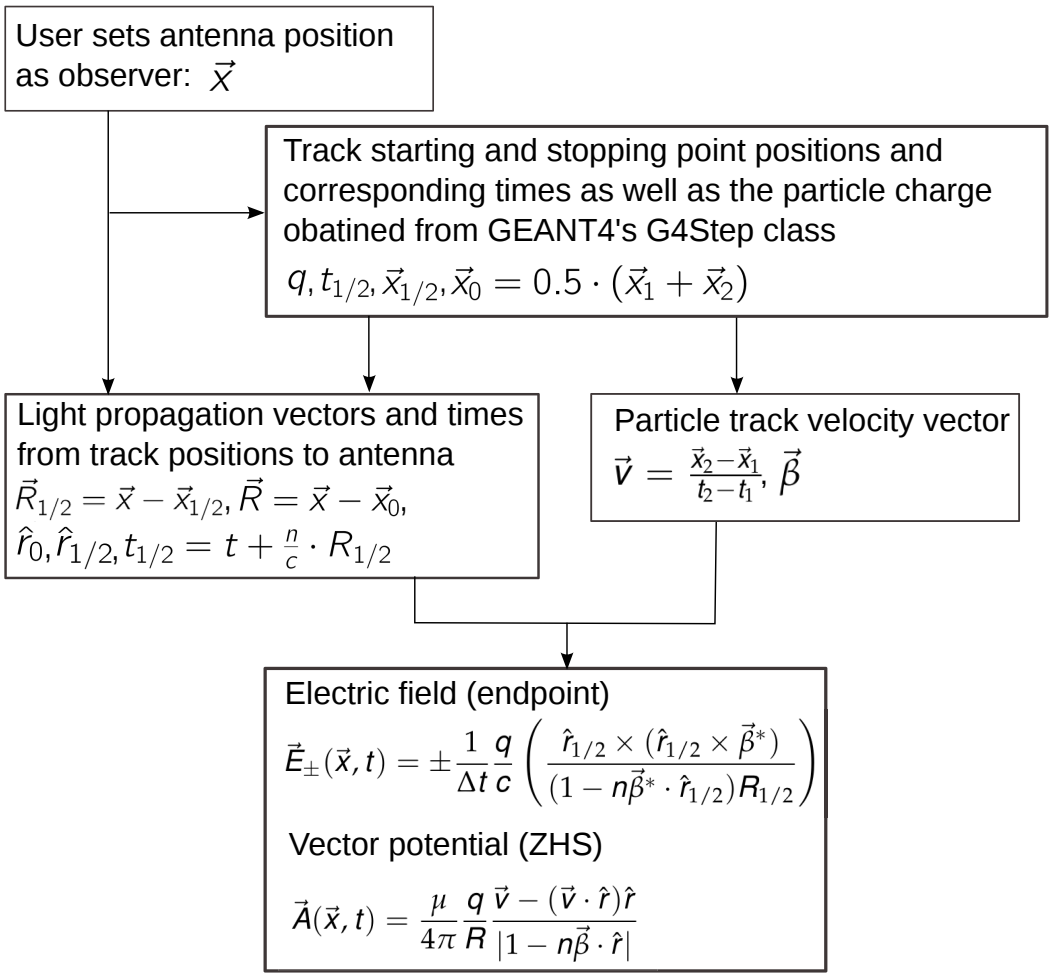

Figure 27: Parameters which define the track and the observer obtained from Geant4 and the derivation of other used parameters to calculate the electric field and the vector potential, respectively.

simulation study: Fig. 28 shows a comparison of the resulting radio signal filtered to a frequency band of $300 - 1200$ MHz from a simulation ran with 5000 and 25000 electron primaries, respectively. After scaling to 131 pC, the signals for both simulations are consistent with each other.

The specifics of the implementation of the two formalism are presented in the following:

5.3.1 Details of the implementation of the ZHS formalism

The ZHS formalism calculates the radio emission of a particle track as a vector potential, as introduced in section 3.1.

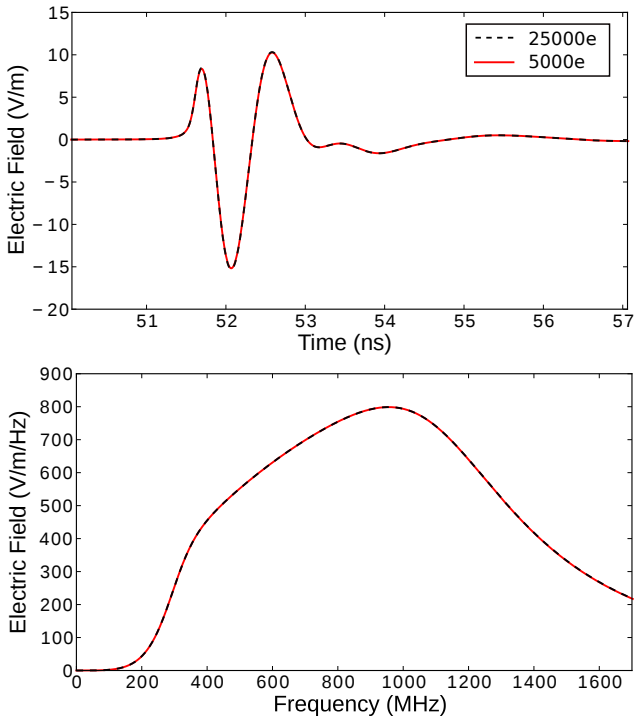

Figure 28: Results for the radio signal for an antenna height of 6.5 m using the endpoint formalism, simulated with 5000 (red solid line) and 25000 (black dashed line) electron primaries and filtered to a frequency band of 300 − 1200 MHz: Top: Signals in the time domain scaled to 131 pC. Bottom: Signals in the frequency domain scaled to 131 pC.

Since a shower is considered to be a superposition of finite particle tracks (sub-tracks) with a constant velocity, the vector potential of a shower is simply given by the sum of the individual track-level vector potentials for an observer position in the far-field:

$$\vec{A}_{shower}(\vec{x}, t) = \sum_{tracks} \vec{A}_{tracks}(\vec{x}, t) \tag{17}$$

The corresponding electric field is then given by:

$$\vec{E}_{shower}(\vec{x}, t) = -\frac{\partial}{\partial t}\vec{A}_{shower}(\vec{x}, t) \tag{18}$$

which can be expressed approximately as:

$$\vec{E}_{shower}(\vec{x}, t_i + \Delta t) = -\frac{\vec{A}_{shower}(\vec{x}, t_{i+1}) - \vec{A}_{shower}(\vec{x}, t_i)}{\Delta t} \tag{19}$$

The middle of the sub-track is chosen as the position vector of the track in eq. 13:
$\vec{x}_0 = \vec{R}_m = 0.5 \cdot (\vec{R}_1 + \vec{R}_1)$
The simulations return the vector potential derived by the ZHS formalism which has then to be converted to the corresponding electric field by formula 19.

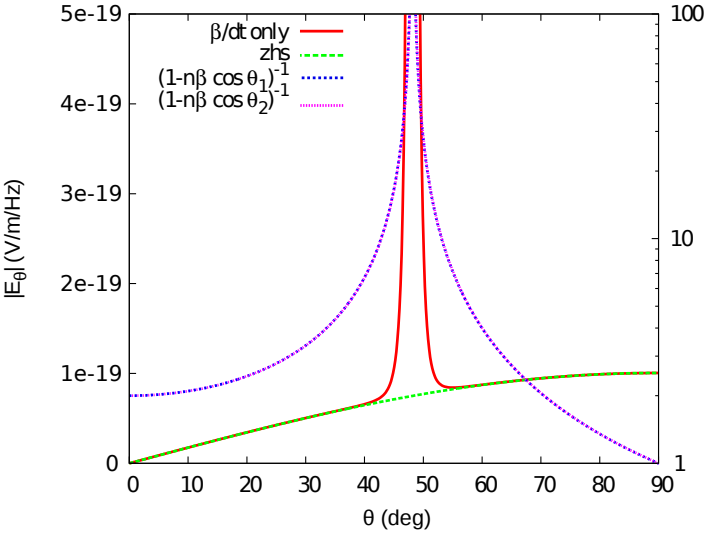

Figure 29: Divergence at Cherenkov angle for the endpoint formalism: Electric field at 10 m distance viewing a 1 cm track at 1 GHz in an refractive index of $n = 1.5$ of the medium [90]. The red line represents the result for the endpoint formalisms, while the green line represents the electric field calculated with the ZHS formalism. The purple and the pink lines show the behavior of the $(1 - n\beta\cos(\theta))^{-1}$-term of the endpoint formalism.

5.3.2 Details of the implementation of the endpoint formalism

The implementation of the endpoint formalism was done in a way similar to the code of the CoREAS program.
As already mentioned in Sec. 3.1.1, the calculation of the radio emission using the endpoint formalism becomes numerically unstable at the Cherenkov angle and a ZHS-like calculation becomes necessary. Thus, the value for the fall-back-threshold to the ZHS-like approach has to be found for the shower evolution in the HDPE target. The behavior of the denominator in formula 12 has to be studied in more detail.
Therefore, the electric field from a track with a length of 1 cm in a distance of 10 m to an observer is calculated [90]. A frequency of 1 GHz and a refractive index of $n = 1.5$ is considered. The comparison of the result obtained by the endpoint formalism (see Fig. 29, left, red line) for the electric field in dependency of the angle θ between the track and the observer is shown in comparison to the result from the ZHS formalism (green dashed line). If the observer angle θ comes close to the Cherenkov angle of about 49° the resulting electric field using the endpoint formalism diverges and goes to infinity while the results for the ZHS formalism remain finite. This divergence is caused by the $1 - n\beta\cos(\theta)$ term in the denominator. Its behavior is also shown in Fig. 29 (right scale) in the first case that θ starts at large angles and then approaches the Cherenkov angle and in the second case it starts at small angles and then approaches the Cherenkov angle.

To avoid diverging results using the endpoint formalisms one has to introduce a threshold for the value of the denominator for which the formalism uses a ZHS-like approach as already introduced in section 3.1.1. Since this threshold depends on the Cherenkov angle, it has to be obtained for each considered medium. For the simulation of the radio emission in

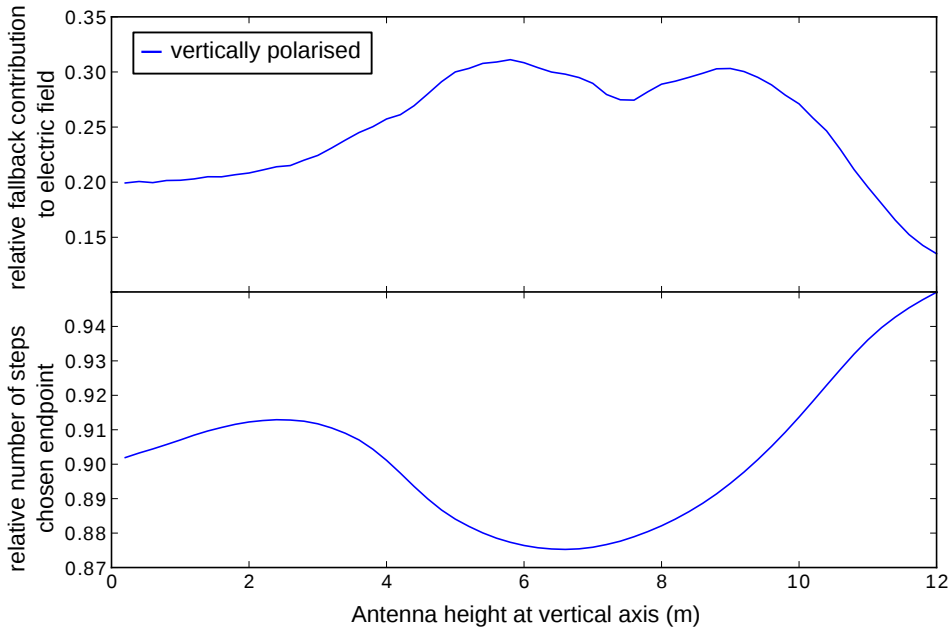

Figure 30: Divergence at Cherenkov angle for endpoint formalism after refraction and transmission: A scan over different antenna position positions on a vertical axis at 10.9 m distance from entering point (no magnetic field applied). The expected Cherenkov cone position is at about 6.5 m height. Top: The relative contribution of the ZHS-like fall-back to the total calculated radio signal using the endpoint formalism for each antenna position. Bottom: The relative numbers of steps in the shower simulation to which the endpoint formalism was applied in dependence of the antenna height.

the T-510 experiment, a threshold value of $(1 - n\beta\cos(\theta))^{-1} = 10$ is chosen to exclude the singularity while for air-shower simulations the threshold value is 1000. This means that for an observer angle of $\leqslant 5^\circ$ around the Cherenkov angle the ZHS-like fall-back is used to calculate the expected radio signal for these tracks.

To check whether the chosen value is suitable, simulations for the radio emission detected by antennas at different heights on a vertical axis at about 12.5 m from the target start were performed, using the T-510 simulation setup and a bandpass filter from $300 - 1200$ MHz. In Fig. 30 the plot at the top shows the the relative contribution of the ZHS-like fall-back to the total calculated radio signal for each antenna position. Even at the height of the Cherenkov cone of about 6.5 m the contribution is less than 30% and therefore, the endpoint formalism still determines the dominant part of the simulated radio signal. This result is consistent with the conclusion from Fig. 30 (bottom) that the relative number of sub-tracks in the simulation which were treated with the endpoint formalism is well above 85%, even with a small bump around the Cherenkov angle as expected. A variation of the threshold value between $9 \leqslant (1 - n\beta\cos(\theta))^{-1} \leqslant 11$ leads to a less than 1%-variation in the peak amplitude for the vertically as well as horizontally polarised component of the simulated radio signal for an antenna position at the Cherenkov cone.

For the simulation study, it is possible to use the set threshold value of $(1 - n\beta\cos(\theta))^{-1} = 10$ since the obtained electric field is still dominantly calculated on the basis of the endpoint

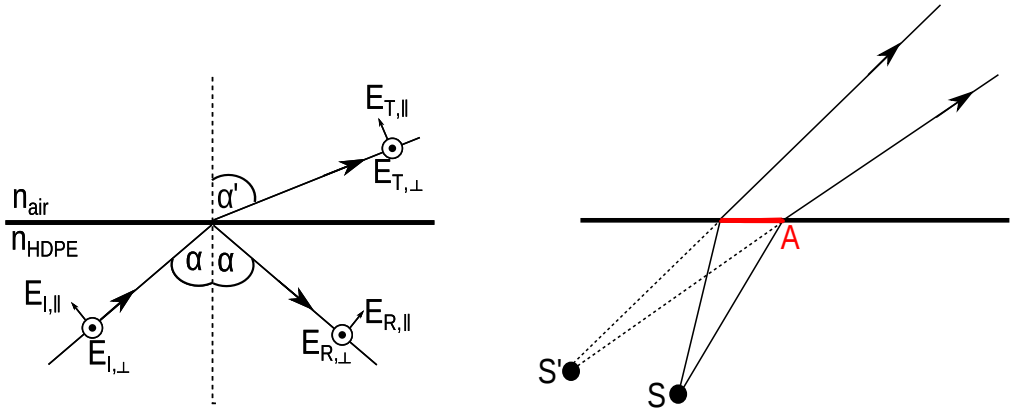

Figure 31: Left: Sketch of the refraction of a incoming ray at a boundary surface. Right: After refraction at a boundary, the rays are spread. This results in an apparent shift of the radiation source from S to S' from the observer's point of view.

formalism and the results for the electric field simulation can be seen as constant within 10% variation of the threshold value.

5.3.3 Timing of the signal arrival in the simulation

Within the Cherenkov cone, if the angle between track and observer is smaller than the Cherenkov angle, one has to account for the reversal of the arrival time for the signals corresponding to the starting and stopping point of the track. The timings have to be carefully checked. Especially, since there are many particles which travels faster than the speed of light in the medium, the chosen time binning of the observer may not be able to resolve the time of the particle track between starting and stopping point (compare to a finite time resolution of a detector). Then a δ-function-like pulse would be produced and the observer time binning could act as a filter. If both arrival times, the one from the starting point and the one of the stopping point, would land in the same observer's time bin, the signal contribution of this track has then to be spread out over time bins, as also done in CoREAS.

5.3.4 Refraction and transmission effects

Refraction at the upper slanted target boundary as well as Fresnel transmission coefficients and demagnification effects [84] are taken into account in the propagation of the radio signals via ray optics. The boundary conditions of Maxwell's equations dictate the change in the amplitude of an electric field passing trough a dielectric boundary. The ratio of the transmitted electric field to the incident one is given by $t = E_T/E_I$. Here, one has to distinguish two cases: the electric field parallel to the plane of incidence ($t_\parallel$) and the electric

field perpendicular to the plane of incidence ($t_\perp$). The corresponding fraction of the electric field which is reflected at the boundary is defined by

$$r_\parallel = \frac{n_{\text{Air}} \cdot \cos\alpha - n_{\text{HDPE}} \cdot \cos\alpha'}{n_{\text{Air}} \cdot \cos\alpha + n_{\text{HDPE}} \cdot \cos\alpha'} \tag{20}$$

$$r_\perp = \frac{n_{\text{HDPE}} \cdot \cos\alpha - n_{\text{Air}} \cdot \cos\alpha'}{n_{\text{HDPE}} \cdot \cos\alpha + n_{\text{Air}} \cdot \cos\alpha'}. \tag{21}$$

$$\tag{22}$$

with α as the angle of incidence to the plane normal and α' as the corresponding angle to the plane normal outside the target (compare to Fig. 31, left).
Finally, the ratio of the transmitted electric field to the incident electric field depends on the ratio of the refractive indices of both media and is given by the the relation to the reflected part of the field as described in [91]:

$$t_{\parallel,\perp} = \sqrt{\frac{n_{\text{HDPE}}}{n_{\text{Air}}}(1 - r^2_{\parallel,\perp})}. \tag{23}$$

Refraction of rays at a boundary between media with different refractive indices results in a shift in the apparent position of the radiation source (see Fig. 31, right). In the treatment of the transmitted signal, it has to be account for this. The law of energy conservation requires that the incident power has to be equal to the sum of the reflected and transmitted power. On the assumption that the area A on the target surface illuminated by the radiation is determined by a spherical wave front and that the angle of incidence and refraction, respectively, are constant in this area, the final analytical form for the so called Fresnel coefficients, including a correction for the spreading of the rays after refraction, can be expressed analytically by [91]:

$$t_\parallel = \sqrt{\frac{\tan\alpha}{\tan\alpha'}(1 - r^2_\parallel)} \tag{24}$$

$$t_\perp = \sqrt{\frac{\tan\alpha}{\tan\alpha'}(1 - r^2_\perp)}. \tag{25}$$

Fig. 32 (bottom) illustrates the Fresnel transmission coefficients behavior as a function of the signal emergent angle. Larger emergent angles represent larger antenna heights with respect to the point of refraction, following a cosine.
For every combination of track and antenna position, the point of refraction on the upper surface has to be found individually. For the calculation of the point of refraction, where the propagation time of the signal from the end-points of the sub-track to antenna is the shortest and its path fulfills Snell's law, the coordinate system is transformed as shown in Fig. 32 (top). Here, the target surface is defined as x-z-plane. From geometrical considerations, the equation

$$|Y_t| \cdot \tan\alpha = |Z_d| - |Y_d| \cdot \tan\left(\arcsin\left(\frac{n_{\text{HDPE}}}{n_{\text{Air}}} \cdot \sin\alpha\right)\right) \tag{26}$$

can be derived, with $|Y_t|$ denoting the distance of the track to the surface and $|Y_d|$ the one for the antenna. The parameter $|Z_d|$ represents the distance in z-direction to the point of

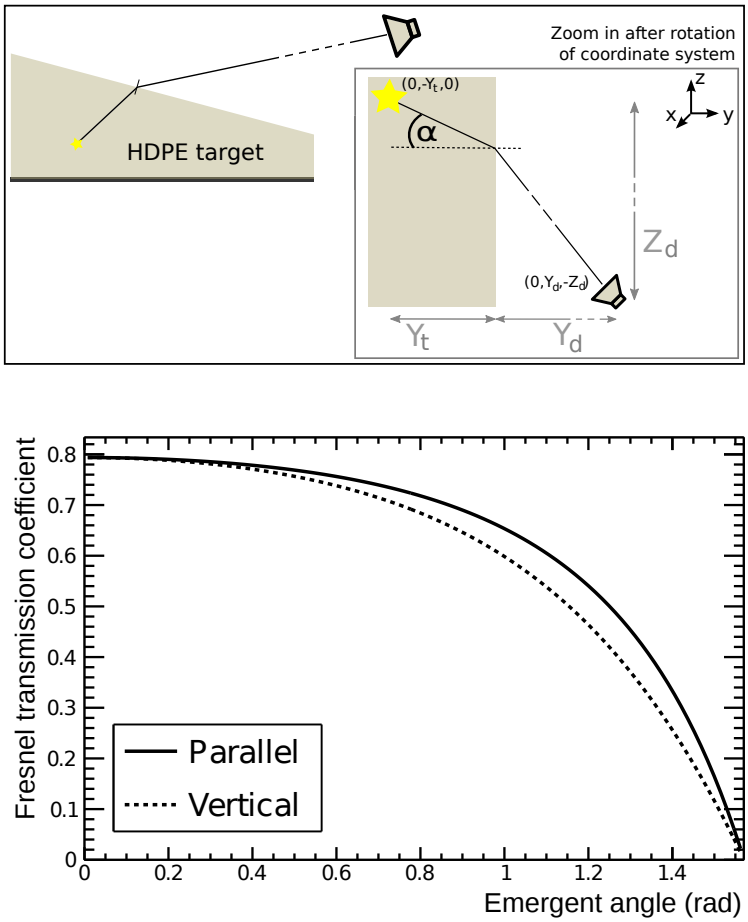

Figure 32: Top: Sketch of the experiment geometry for the calculation of the point of refraction at the upper slanted target surface. Bottom: Values of the Fresnel transmission coefficient for the electric field components parallel and perpendicular to the plane of incidence in dependency on the emergent angle. Both plots are published in [88].

refraction and α the angle of incidence. In the simulation all parameters are known. They can be used to calculate the point of refraction numerically. Equation 26 is used for every track and antenna combination, requiring that the line of sight intersects at the upper target surface. Once the point is known, it is possible to calculate the incident and the emergent angle to the normal of the upper target surface and the corresponding Fresnel transmission coefficients for the vertical and horizontal polarisation components of the electric field with respect to the plane of incidence. This leads to the transmitted electric field

$$\vec{E}_{ant} = (\vec{E}_{em} \cdot \hat{\vec{r}}_{\perp,\,in}) \cdot t_{\perp} \cdot \hat{\vec{r}}_{\perp,\,out} + (\vec{E}_{em} \cdot \hat{\vec{r}}_{||,\,in}) \cdot t_{||} \cdot \hat{\vec{r}}_{||,\,out}. \tag{27}$$

The parameter $\vec{E}_{em}$ is the electric field emitted by the track, $\hat{\vec{r}}_{\perp}$ the vector which is perpendicular to the plane of incidence (*in*) as well as after being refracted at the boundary (*out*) and $\hat{\vec{r}}_{||}$ is the vector lying in the plane. The factors $t_{\perp}$ and $t_{||}$ are the corresponding Fresnel transmission coefficients [84] for the perpendicular and parallel polarisation components, respectively. The time t_{prop} for the signal propagation from track to antenna is obtained directly from using the point of refraction and is given by:

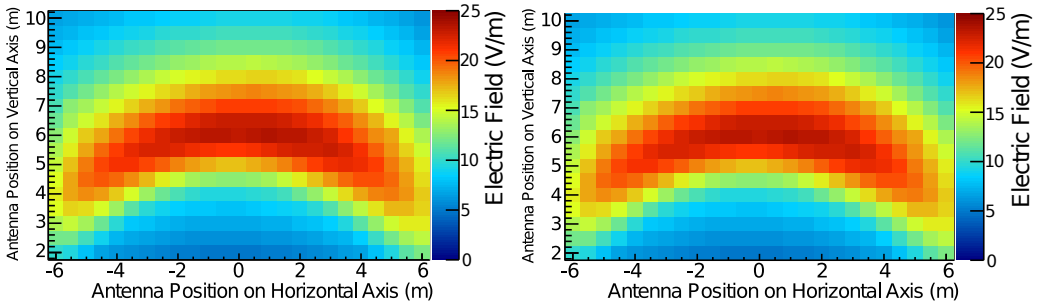

Figure 33: Total peak amplitude of the electric field for a 2D antenna array using the endpoint formalism: Left: Total electric field for a magnetic field of a strength of 0 G. Right: Total electric field for a magnetic field of a maximum strength of 970 G, published in [88].

$$t_{prop} = n_{\text{HDPE}} \cdot \frac{d_{\text{HDPE}}}{c} + n_{\text{Air}} \cdot \frac{d_{\text{Air}}}{c} \tag{28}$$

with the distance between track and point of refraction d_{HDPE} and the distance between point of refraction and antenna d_{Air}. The time t_{prop} has then to be added to the time when the signal is emitted by the track.

5.3.4.1 Diffraction at the upper target surface

Since the top surface of the target acts as a diffractive slit with a width of 60 cm which is smaller than the length of the target, the low frequencies around 300 MHz can be affected by diffraction. Since this is not included, the simulations modestly overestimate the resulting electric field at low frequencies [80].

5.4 APPLICATION OF THE SIMULATION TO THE T-510 EXPERIMENT

In the SLAC T-510 experiment one can manipulate the intensity of the signal strength in the horizontal polarisation component of the electric field by changing the strength of the magnetic field along the vertical axis [80]. Thus, it is possible to study the influence of the magnetic field on the emission of the radio signal. For the experiment it is expected that the measured electric field strength in the horizontal polarisation component rises linearly with rising magnetic field strength, due to the (geo-)magnetic effect, whereas the signal in the vertical polarisation component due to the Askaryan effect should be independent of the induced magnetic field.

First, the electric field in the time domain has been calculated using the endpoint formalism for an array of antenna locations with positions in 0.5 m steps and with a primary electron energy of 4.35 GeV. The distance to the entry point of the electrons in the target is about 13 m. To investigate the effect of a magnetic field on the radio signal, a magnetic field using the values from the measured magnetic field map, which has the maximum strength of up to 970 G for an applied current of 2400 A in the vertical direction perpendicular to the electron beam, is switched on in the Geant4 simulation.

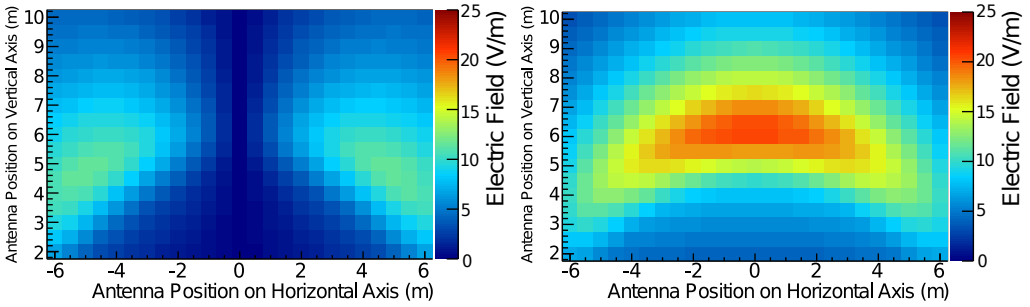

Figure 34: Peak amplitude of the electric field for a 2D antenna array using the endpoint formalism for a magnetic field of a strength of 0 G: Left: Horizontally polarised component. Right: Vertically polarised component.

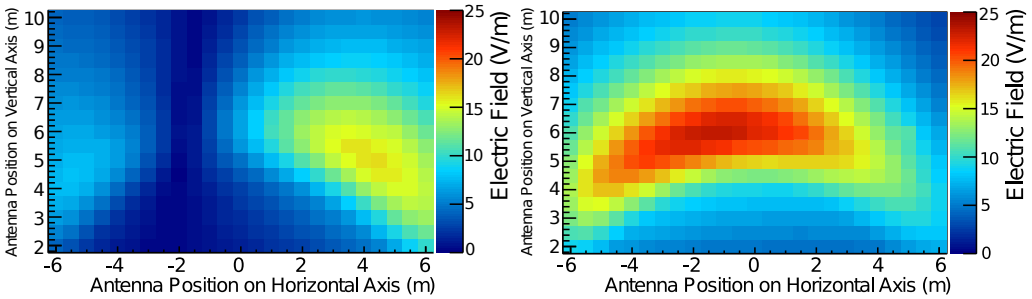

Figure 35: Peak amplitude of the electric field for a 2D antenna array using the endpoint formalism for a magnetic field of a maximum strength of 970 G: Left: Horizontally polarised component. Right: Vertically polarised component. Both plots are published in [88].

For no induced magnetic field and for the maximum strength of 970 G, the resulting maximum peak amplitudes of the electric field are shown in figure 33. The positions of the maximum values for the peak amplitude of the signal form a strong Cherenkov ring, whose position agrees with the expectation given by the refractive index of $n_{\text{HDPE}} = 1.52$ and $n_{\text{Air}} = 1.0003$. The finite target size leads to a cut-off of the Cherenkov ring on both sides. The more elliptical than circular appearance of the ring is caused by the refraction at the slanted target surface. Switching on the magnetic field leads to an asymmetric rise of the total signal amplitude on the ring structure to one side. The impact of the (geo-)magnetic effect is observable especially if the electric field is split up into the horizontally and vertically polarised component (compare Fig. 34 to Fig. 35). An induced magnetic field leads to a shift of the peak amplitude distribution in both polarisations on the Cherenkov ring.

The results for the “ZHS” formalism are shown in Fig. 36. They are nearly identical to those for the endpoint formalism.

5.4.1 Transition Radiation

Charged particles crossing a boundary of media with different refractive indices produce transition radiation, in this case at the boundary of the lead pre-shower to the HDPE target. This leads to a possible additional source of radiation which can be estimated with Geant4 simulations using the endpoint formalism (see Chapter 3.1.1): The steps in the simulation

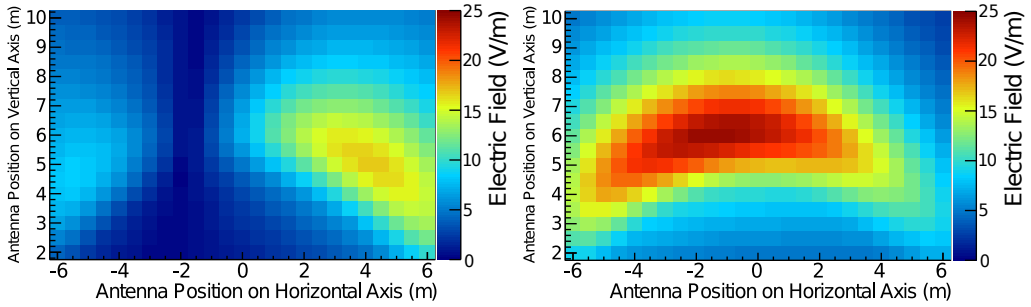

Figure 36: Peak amplitude of the electric field for a 2D antenna array using the ZHS formalism for a magnetic field of a maximum strength of 970 G: Left: Horizontally polarised component. Right: Vertically polarised component.

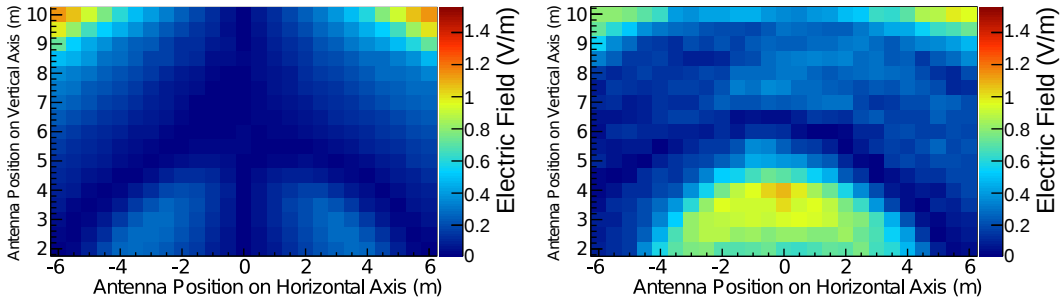

Figure 37: Contribution of transition radiation to the peak amplitude in the time domain for a magnetic field strength of 970 G: Left: Horizontally polarized component. Right: Vertically polarized component. These results are published in [88].

program are limited by the boundary of the current volume. This means that the step ends exactly at the boundary of the pre-shower. The electric field produced by steps in the metal pre-shower can not escape. The following steps of the particle track start directly in the HDPE target at the boundary. The produced electric field produced at its start point represents the contribution to the signal from the expected transition radiation [52].
A shower with 10,000 primary electrons with an energy of 4.35 GeV was simulated to reduce statistical fluctuations. The absolute contribution of the transition radiation to the signal of the whole shower for a 2D antenna array at about a distance of 13 m to the entry point of the beam is shown in Fig. 37. Since the magnetic field already starts to affect the shower during the pre-shower stage, a small asymmetry in the signal distribution is observable.

The relative contribution by the transition radiation to the radio signal strength is about 1% for the horizontally as well as for the vertically polarised components for antenna position close to the Cherenkov angle (compare the absolute scale to Fig. 35), the impact of transition radiation is thus negligible for the this study.

5.4.2 Comparison of simulation results using the endpoint and the ZHS formalisms

Since the calculation of the radio signal from a particle shower can be done in parallel with both formalisms, a direct comparison of their results can be performed to study possible differences due to approximations made in the formalisms.

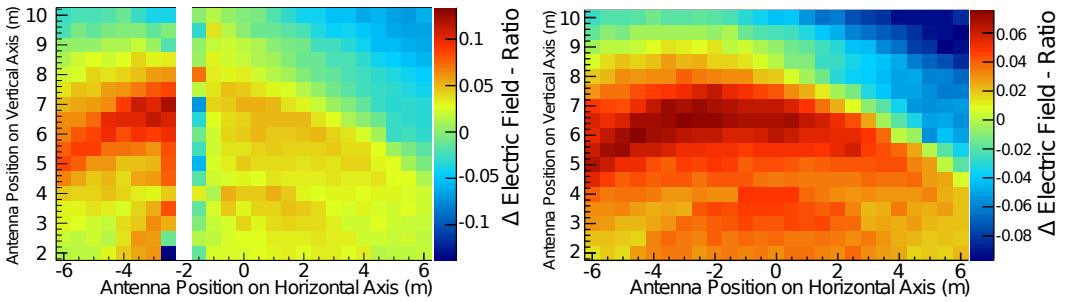

Figure 38: Relative deviation of the peak amplitude in the time domain defined as $\frac{E_{\mathrm{ZHS}} - E_{\mathrm{endpoint}}}{E_{\mathrm{ZHS}}}$ for a magnetic field strength of $B = 970\,\mathrm{G}$: Left: Horizontally polarised component. Antenna positions with negligible signals have been excluded in the comparison (white area). Right: Vertically polarised component. Both plots are published in [88].

Figure 38 (left) shows the 2D distribution of the relative deviation of the peak amplitude in the time domain between the endpoint formalism and the ZHS formalism for the maximum magnetic field strength of 970 G using the realistic field map and a primary beam energy of 4.35 GeV. A ring structure is still visible in the distribution. Despite only small fluctuations, no systematic offset between the results of the two formalisms can be observed. However, the comparison shows that the deviations in the horizontally (left) and vertically polarised components (right) depend on the position of the antenna and that the endpoint and ZHS formalisms lead to the best agreement in the area where the Cherenkov cone is expected if a magnetic field is applied.

This leads to the conclusion that the formalisms reproduce the contribution due to the magnetic effect in a slightly different way. Furthermore, inside the Cherenkov ring the ZHS formalism leads to slightly higher results and the endpoint formalism predicts slightly higher amplitudes outside the ring. Where these differences come from has to be studied in more detail. On the basis of the T-510 measurements a differentiation between both formalisms can not be obtained due the systematic uncertainties in the experiment.

5.4.3 Cherenkov-like effects reproduced by the simulation

As already described in Section 3, at the Cherenkov angle the emission gets enhanced since the radiation emitted from the whole particle shower arrives simultaneously (see sketch in Fig. 9). The emission is compressed in time and the pulses become very narrow, being coherent up to frequencies in the GHz region.

To demonstrate that this is also valid for the simulations, the radio emission from particular parts of the target were calculated. The target was sliced into the parts $0-50\,\mathrm{cm}$, $50-100\,\mathrm{cm}$, $100-150\,\mathrm{cm}$, $150-200\,\mathrm{cm}$ and $200-400\,\mathrm{cm}$ from the target beginning along the beam line. Fig. 39 shows the horizontally polarised (left) and the vertically polarised component (right) of the calculated electric field based on the endpoint formalism. The simulations for three different antenna heights, consisting of one position inside (bottom), one on (middle) and one outside (top) the Cherenkov ring, are bandpass-filtered to $300-1200\,\mathrm{MHz}$. The color code represents the part of the target and the particle shower, respectively, from

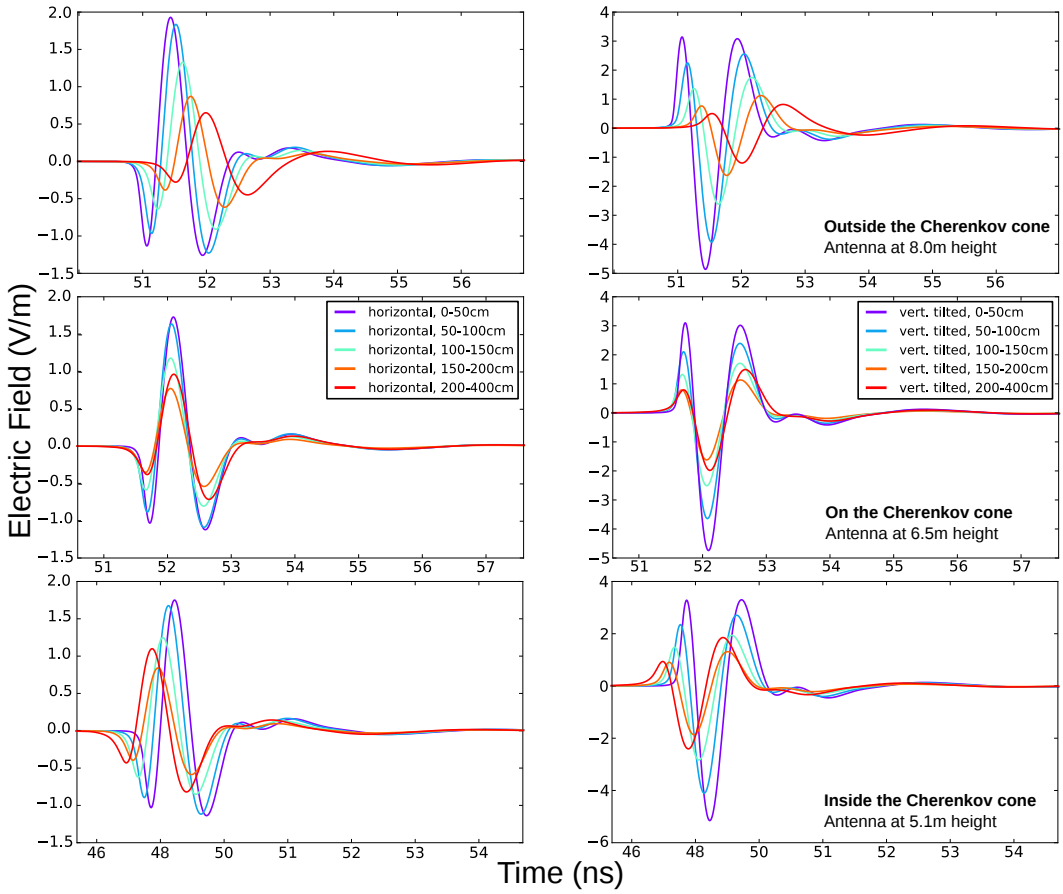

Figure 39: Testing Cherenkov-like effects using the endpoint formalism: Horizontally (left) and vertically polarised (right) components of the electric field produced of a "sliced" particle shower in a magnetic field with the strength of $B = -970\,\mathrm{G}$ for different antenna heights (the heights are from the top to the bottom: 8.0 m, 6.5 m and 5.1 m) are shown, using the endpoint formalism and filtered from $300 - 1200\,\mathrm{MHz}$. In addition to different produced electric field strengths, a reversal for the arrival times of the radio signal produced in each "slice" is observable while crossing the Cherenkov cone.

which the radio emission is produced. Here, the violet color stands for the early part and red for the later part of the particle shower.

For the antenna position on the Cherenkov ring at 6.5 m height the radio emission from all the parts of the particle shower arrives simultaneously and can add up at the antenna to a sharp pulse. For the position at 5.1 m height, "inside" the Cherenkov cone, a time ordering in the arrival time of the radio signal from the different particle shower slices is visible. The radio emission of later parts of the shower arrives earlier than from the beginning of the shower which agrees with the geometrical expectations. In comparison, for the antenna height at 8.0 m, meaning after crossing the Cherenkov angle, the time ordering of the arrival times of the radio signal of each slice is reversed and the emission of the early shower parts arrives first at the antenna as expected.

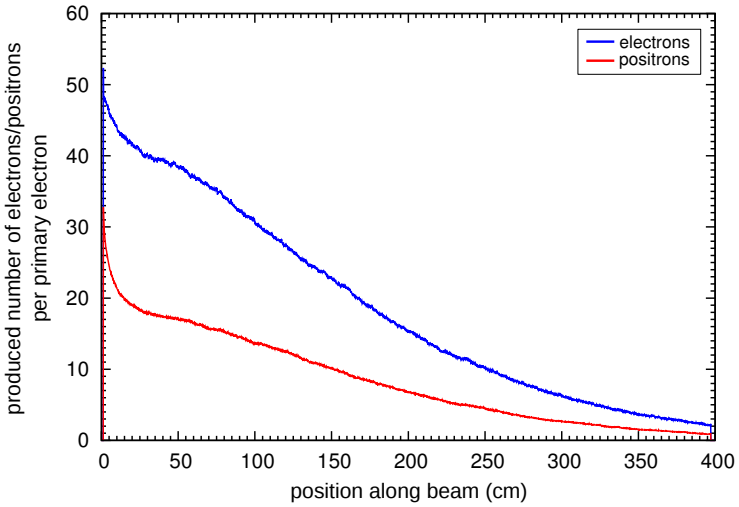

Figure 40: Longitudinal distribution of the simulated steps of the shower electrons and positrons in the target along the beam line for an magnetic field of $B = 970$ G, normalised to the number of simulated primary electrons of an energy of 4.35 GeV (1 mm binning).

5.4.3.1 Position of maximal radiation

Another aspect which can be observed in Fig. 39, for all three antenna positions as well as for both polarisation components, is that most of the radiation comes from the beginning of the target and less from the target end.

Due the lead pre-shower of a width of 2 radiation lengths the shower contains the highest number of particles close to the entering point of the beam line to the target. This is confirmed by plotting the number of electrons and positrons created in the simulations in dependency of their position in the target (see. Fig. 40). A small bump in the distribution of electrons is visible at about 50 cm. Comparing Fig. 39 and Fig. 40 leads to the conclusion that the signal strength of the radio signal and the number of electrons and positions are closely connected. This becomes important later in Chapter 6.3.

6 COMPARISON OF MICROSCOPIC SIMULATIONS OF RADIO EMISSION TO MEASURED DATA

In the context of this thesis, principle ideas, as presented in this chapter, as well as some figures and preliminary results, were already published in:

- A. Zilles for the SLAC T-510 collaboration, “Modeling of radio emission from a particle cascade in a magnetic field and its experimental validation” in the proceedings of the 7th Acoustic and Radio EeV Neutrino Detection Activities (ARENA 2016) [92],
- K. Belov et al., “Accelerator measurements of magnetically-induced radio emission from particle cascades with applications to cosmic-ray air showers”, in Phys. Rev. Lett. 116, 141103 (2016) [80].

In this chapter, the results of the simulation using the endpoint and the ZHS formalisms (see Chapter 5) are compared with the measured data of the SLAC T-510 experiment (see Chapter 4). Since there is no antenna response model etc. included, first the simulations are convolved with the detector response of the T-510 antennas.

6.1 CONVOLVING THE SIMULATIONS WITH THE DETECTOR RESPONSE

In the antennas, the signal in the vertically polarised channel leaks into the horizontally polarised channel at about a 25 % level [81]. To eliminate the leakage, the difference in the signal for the two magnetic field directions, field up (V_{B+}) and field-down (V_{B-}), was analyzed. This means that the cross-talk of the antennas is removed for the horizontally polarized component by averaging the waveforms with opposite polarity in the current flowing through the magnetic coils. To remove extraneous noise, a data window of ± 10 ns around the peak ($\sim$ 4 ns) was chosen for the spectral comparison. For a direct comparison of the simulation results from the endpoint and ZHS formalisms with the measured voltages, the simulations are convolved with the measured system response of the cables and filters for each channel and the effective height of the antennas. At the antennas, the voltage in the time-domain is described by the convolution

$$V(t) = h_{\text{eff}}(t) \circ h_{\text{sys}}(t) \circ E(t) \tag{29}$$

with the antenna impulse $h_{\text{eff}}(t)$, the system impulse response due to filters and cable losses $h_{\text{sys}}(t)$ and the simulated electric field $E(t)$. This is equivalent to the multiplication of the effective height, $h_{\text{eff}}(t)$, the system $h_{\text{sys}}(f)$ and the electric field in the frequency domain. In Fig. 41 (left) the effective height of the antennas as a function of frequency for various angles to the boresight of the antenna is shown. The relative gain of the antennas varies by 3.7 dB for the vertically polarised channel and by 2 dB for the

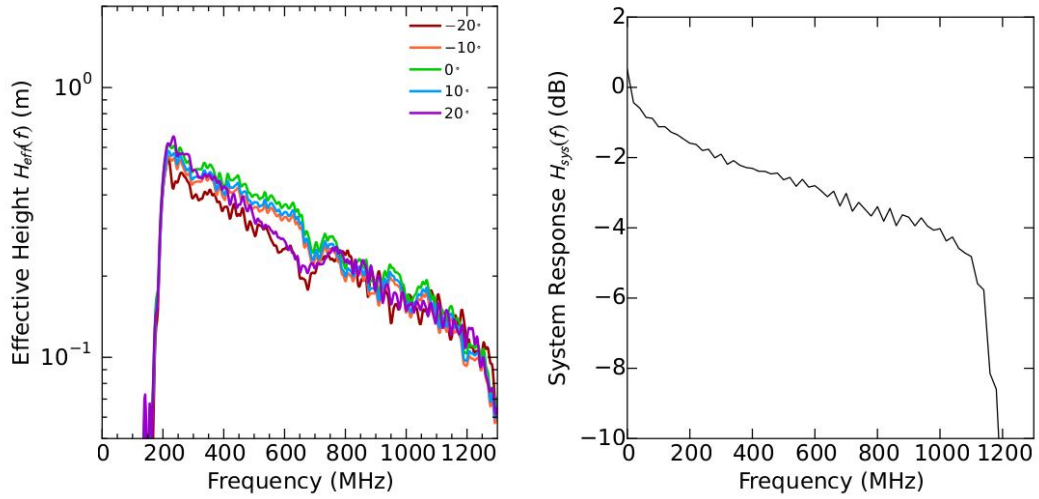

Figure 41: Left: Behavior of the effective height, $H_{\text{eff}}(f)$, for several elevation angles relative to the bore-sight of the antenna [81]. Right: An example channel system response $H_{\text{sys}}(f)$ including cables and filters of the SLAC T-510 experiment [81].

horizontally polarised one. The sharp sensitivity loss shown in Fig. 41 (right) is driven the system response dominated by the 1250 MHz low pass filter.
In addition the simulations are down-sampled to 10 GHz while the measured data is sampled with 5 GHz.

6.2 COMPARISON OF THE SIMULATION RESULTS USING THE ENDPOINT AND THE ZHS FORMALISM TO MEASURED DATA

For a first comparison of simulations and data, the antenna position on the Cherenkov ring at a height of 6.5 cm was chosen. At this position, the vertical component of the antenna measures the Askaryan component and the horizontal component measures the magnetic component of the radio signal (compare to Chapter 4.1.4). Thus, both effects can be studied separately, as shown in Fig. 42. As already expected from Fig. 38, the peak amplitude predicted by the two formalisms agrees within 4.1% in the horizontally polarised component and within 4.9% in the vertically polarised component, compared to the electric field calculated using the endpoint formalism. In the comparison with the simulated electric field, the peak amplitude of the measured data for the same antenna position exceeds the simulations in both cases by about 30% in the time domain: for the horizontally polarised component, the measured peak amplitude exceeds the predicted amplitude derived from the endpoints formalism by 34.4% and for the results using the ZHS formalism by 33.7%. For the vertically polarised component, the peak amplitude of the data exceeds the simulated one by 31.1% for the endpoint formalism and by 27.5% for the ZHS formalism. The excess is also observable in the frequency domain for measured frequencies from $300 - 1100$ MHz (see Fig. 42, bottom).
Since both, the ZHS and endpoint formalisms, are implemented in Geant4 in parallel, the simulated results can be compared without any shower-to-shower fluctuations or impacts of the chosen models for any interaction. The difference in their peak amplitudes of the time traces for an antenna position at the Cherenkov cone is within 5% for both polarisation

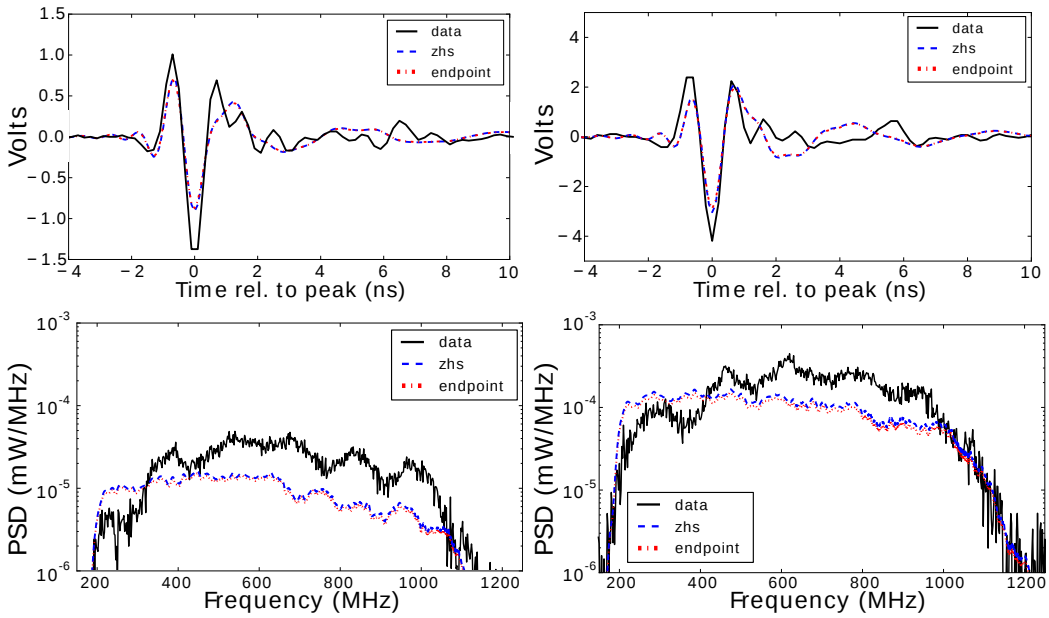

Figure 42: Comparison of the horizontally (left) and vertically polarised (right) component for an antenna position at 6.5 m height: time traces (top) and frequency domain (bottom) without inclusion of reflections.

which leads to the conclusion that the two formalisms deliver consistent results at that level. The discrepancy in the peak amplitudes between the simulations and the data is significantly larger which limits the ability to distinguish between the results for the ZHS and endpoint formalisms.

6.3 IMPACT OF INTERNAL REFLECTIONS

This apparent discrepancy between the simulated results and the measured data can be explained by internal reflection at the bottom surface of the target as a systematic uncertainty in the experiment. Since the frequency-depending reflection characteristics of the target-to-blanket boundary are not known for frequencies < 1 GHz (compare to Chapter 4.1.2), an implementation of the reflection in the simulation was not possible. A first attempt to achieve information about the reflectivity of the blanket was performed by fitting the simulations to the data with the refractive index and the signal amplitude as free parameters [93]. This returned an inconsistent value for the refractive index for different antenna heights.

To show that the internal reflection at the bottom surface is a valid explanation for the discrepancy between the simulated results and the measured data, a simpler attempt to model the reflection is made in the following:
The reflection is handled as a total reflection at the bottom boundary of the target without any frequency dependence.
Since the convolution of the simulated signal with the detector response is a linear operation, only the simulated “direct” signal needs to be convolved.

Fig. 43 shows schematically the ray tracing in the T-510 experiment. The direct radio signal is emitted at an angle of $\theta_C = 49.2°$ given by the refractive index of the target material

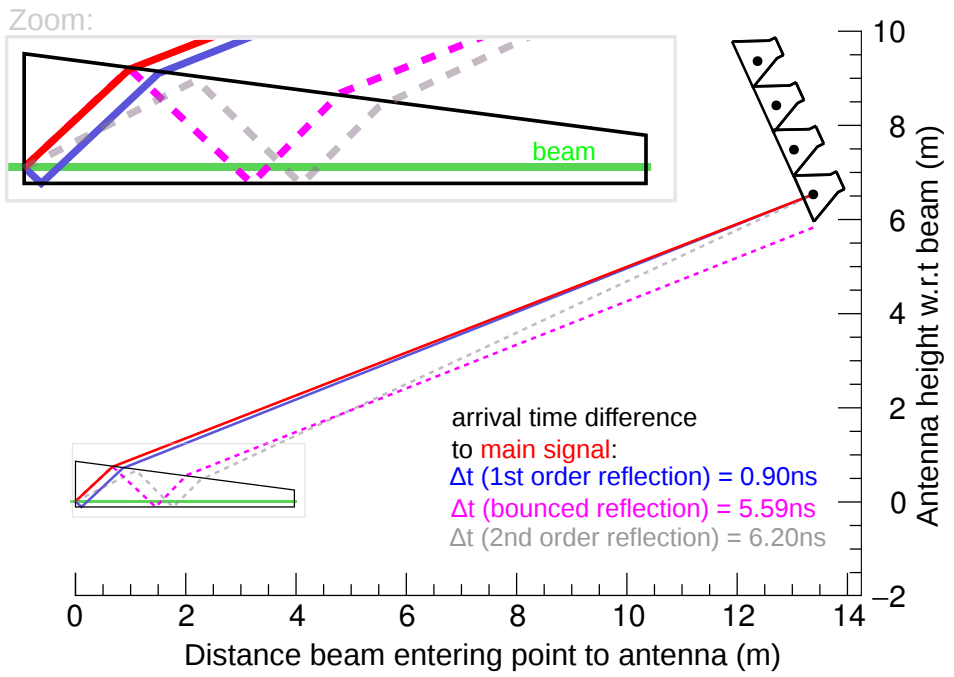

Figure 43: Internal reflection in the target: ray tracing of internal reflections of different orders to estimate their impact on the radio signal detected by an antenna.

($n_{\text{HDPE}} = 1.53$). Most of the signal hitting the upper slanted surface of the target can escape, while a small part gets reflected. Since the radio signal is emitted radially, also radiation towards the bottom surface of the target is emitted at an angle of $\theta_C = 49.2°$. Based on the unknown properties of the RF absorbing blanket, the worst-case scenario of a total reflection at the bottom target surface is assumed. This means that the signal is reflected with the same amplitude (reflection coefficient $R = 1$) as the incoming one but with a flipped sign as illustrated in Fig. 44.

The reflection coefficient and the flip of the sign for the horizontal component (E'_{H} to E''_{H}) is given by the corresponding Fresnel coefficients. For a non-magnetic, dielectric medium the Fresnel coefficient reduces to [51]:

$$\frac{E''_{\text{H}}}{E'_{\text{H}}} = \frac{n_1 \cos(\theta') - \frac{\mu_1}{\mu_2}\sqrt{n_2{}^2 - n_1{}^2 \sin(\theta')}}{n_1 \cos(\theta') + \frac{\mu_1}{\mu_2}\sqrt{n_2{}^2 - n_1{}^2 \sin(\theta')}} = \frac{n_1 \cos(\theta') - \sqrt{n_2{}^2 - n_1{}^2 \sin(\theta')}}{n_1 \cos(\theta') + \sqrt{n_2{}^2 - n_1{}^2 \sin(\theta')}}. \quad (30)$$

With $\mu_1 = \mu_2 = \mu_0$, assuming a refractive index of the blanket which is larger than the one of the target ($n_1 = n_{\text{HDPE}}$ and $n_2 = n_{\text{blanket}}$) and an incoming angle of $\theta' = 40.8°$ to the normal of incidence returns a ratio of the incoming signal to the reflected on of $-1 \geqslant \frac{E''_{\text{H}}}{E'_{\text{H}}} \geqslant 0$. A similar calculation can be done for the vertical component of the emitted signal. It returns a ratio of $0 \leqslant \frac{E''_{\text{V}}}{E'_{\text{V}}} \leqslant 1$. But the vertical component acquires a phase jump of π for the emission towards the bottom surface just by geometry, as shown in Fig. 44.

Since the angle of the radiation which can escape after the reflection on the bottom does not differ appreciably from the Cherenkov angle, it is assumed that the transmission coefficient at the upper surface for the reflected emission is equivalent to the one of the direct

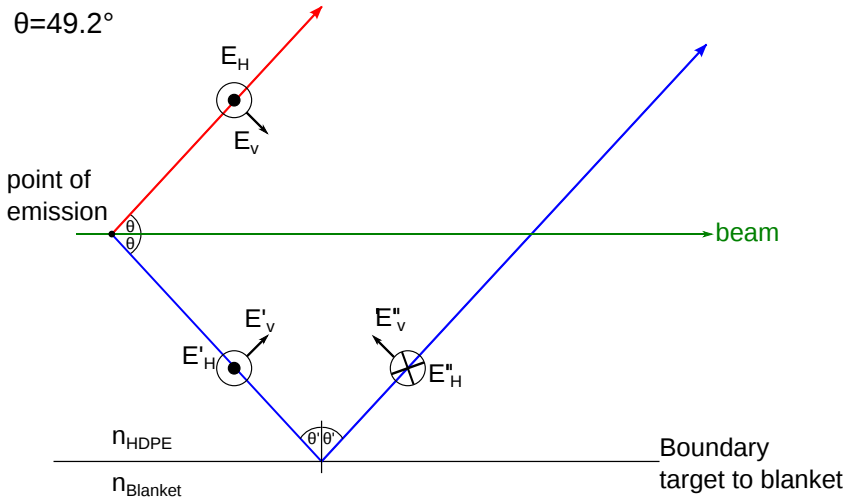

Figure 44: Illustration of the idea to split up the produced electric field into a horizontally polarised component (E_H) and a vertically component (E_V). It is also shown that the horizontally polarised component experience a phase jump at the boundary of the target to the RF absorbing blanket.

signal.

Finally, the direct and the reflected signal can be added up, taking into account the polarity of both signals and the time difference in the arrival time at the antenna given by geometry. The difference in the arrival time of the direct and the reflected signal can be derived by ray tracing (see Fig. 43), again assuming that the blanket has a much higher refractive index than the target. Since most of the radiation arriving at the antenna is coming from the beginning of the target (compare to Fig. 39), the entry point of the beam in the HDPE target is chosen as the reference point for the ray tracing.

For the antenna position at a height of 6.5 m the time difference between the direct and the reflected signal is about 0.9 ns which means that the main and the reflected signal overlap and cannot be resolved. The next order of reflection (see Fig. 43, pink dashed line) already has a time difference to the direct signal of about 5.6 ns and would be measured at another antenna position. The second-order reflection (gray dashed line) has a time difference of 6.2 ns and is thereby clearly separated from the direct signal in time.

In Fig. 45 (top), the bump originated from the second-order reflection is visible in the data trace at about 6.2 ns later than the peak pulse, but with a much smaller amplitude than the main peak. This is a validation of the geometrical concept and shows that all higher-order reflections have a much lower amplitude due to the transmission coefficients and are therefore negligible. This contribution can also be simply windowed out, as illustrated in Fig. 46. Such a windowing results in a disappearance of the modulation in the power frequency spectrum of the data with a $\Delta f \simeq 150$MHz beat [80]. Since the time trace is artificially cut, information in the radio signal is lost which could explain the missing suppression of the high and low frequencies.

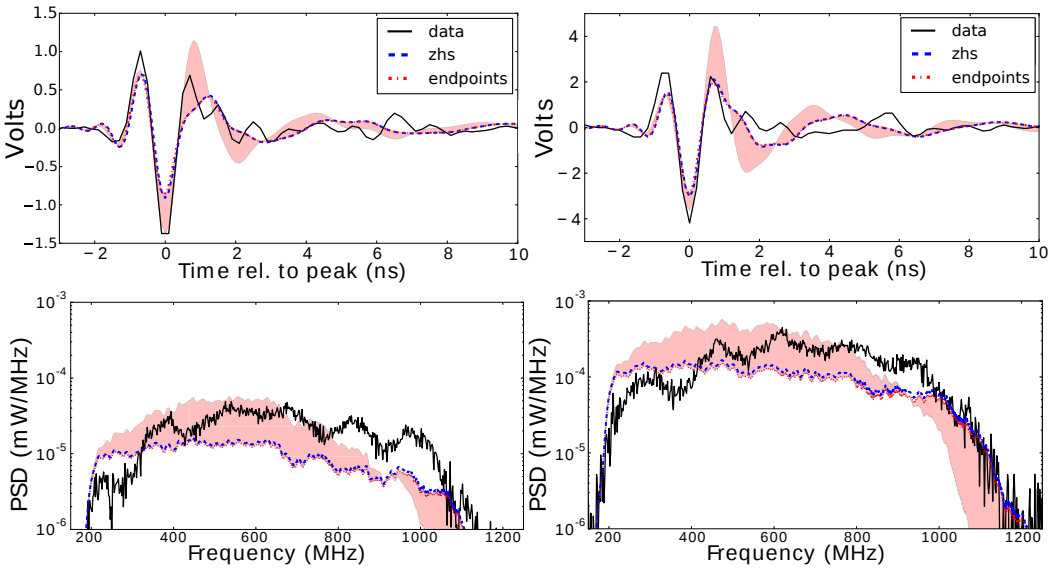

Figure 45: Horizontal (left) and vertical (right) polarisation for an antenna position at 6.5 m height: time traces (top) and frequency spectra (bottom) are shown including reflection at the bottom surface in comparison to measured data (black lines). To compare the time traces, the simulated direct signal (colored lines) and the signal including the reflection on the bottom surface (red band) were shifted to overlap with the data's peak amplitude.

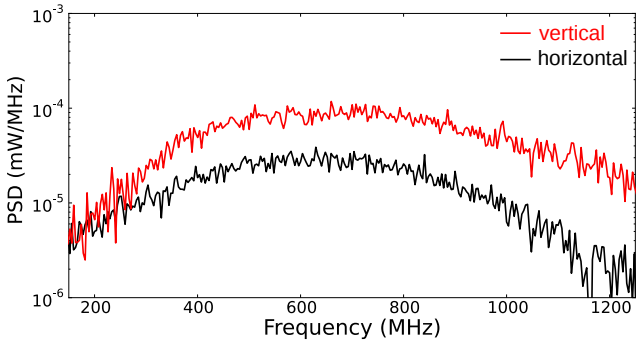

Figure 46: Frequency spectrum of horizontally (black) and vertically (red) polarised component of the radio signal for an antenna position at 6.5 m. Here, the bump originated from the second-order reflection at about 6.2 ns later than the main peak is windowed out in time.

Fig. 45 shows the radio signals of the data measured by an antenna position at the Cherenkov cone in comparison with the corresponding convolved simulations, based on the endpoint and the ZHS formalisms. Here, the red band represents the range of solutions between the simulated pulse with and without including the reflected pulse at the bottom target surface, as described above. For the time domain (left) the simulated signals including the reflection can describe the measured peak amplitudes very well for both polarisations. For the vertically polarised component the measured pulse exceeds the simulated one including the reflections by 5% in the case of the endpoints formalism and 11% for the ZHS formalism. The difference in the simulated peak amplitude of the two formalisms to each other is 5% which does not differ from the simulated results without inclusion of reflections. For the horizontally polarised component the agreement is even better. The data exceeds the resulting peak amplitudes of the simulations based on the endpoint formalism by 0.4%, based on the ZHS formalisms by 3%.

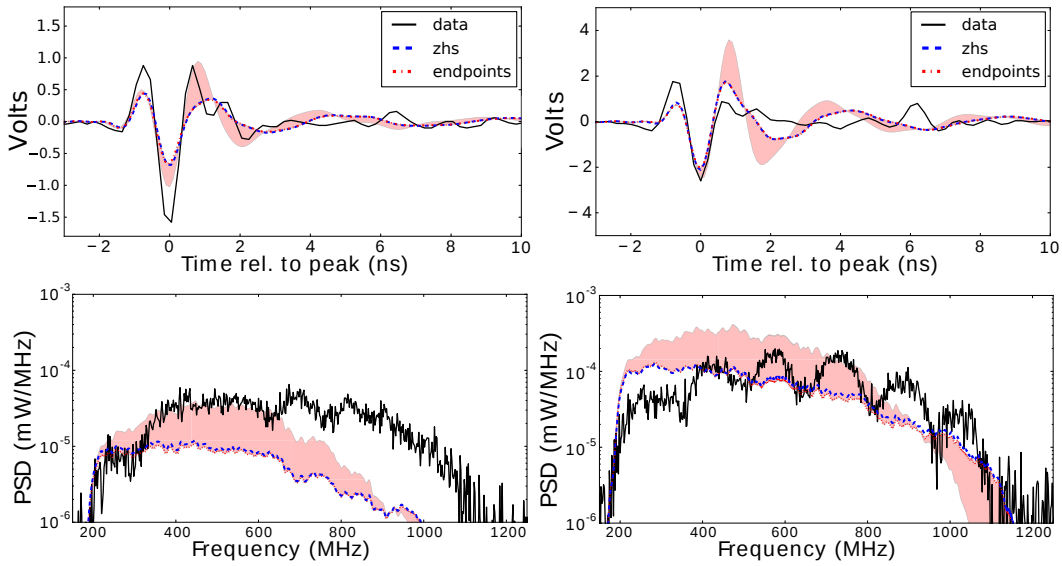

Figure 47: Horizontal (left) and vertical (right) component for an antenna position at 4.1 m height (inside the Cherenkov cone): time traces (top) and frequency domain spectra (bottom). The red band describes the impact of the internal reflection in the simulated result.

The modeling of the reflections which will overlap with the main signal can reproduce the peak amplitudes for both polarisations in the time domain. Here, it could be shown that the internal reflection is the dominant uncertainty in this experiment and its impact can be handled as a systematic uncertainty.

However, the after-pulse of the radio signal at 0.9 ns after the main pulse in the time domain is predicted to be larger than measured. Also in the frequency domain, this observation is confirmed. A comparison of the simulated and the measured frequency spectra led to the conclusion that the assumption of the total reflection for all frequencies is too simple, since the simulations including the modeled reflection show a strong suppression of the signal for high frequencies. Such a suppression is not expected for high frequencies. In the upper range of measured frequencies the blanket under the target should absorb a part of the radiation emitted towards the upper target surface (compare to Fig. 18). This means the assumption of a constant refractive index and a worst-case scenario of frequency-independent total reflection is oversimplified.

Fig. 47 shows a comparison of the measured data and the corresponding simulations for both polarisations for an antenna position at a height of 4.1 m and Fig. 48 a comparison for an antenna position at 8.4 m. For both heights, inside and outside the Cherenkov cone, the too strong suppression of high frequencies in the simulations due to destructive interference at the antenna is observable for both polarisations. While the peak amplitudes of the vertically polarised component can be nicely described by the simulation including the reflections, the peak amplitude of the horizontally polarised component is underestimated for the position inside the cone and slightly overestimated outside the cone.

In summary, a comparison of the simulations and the measured data shows a difference

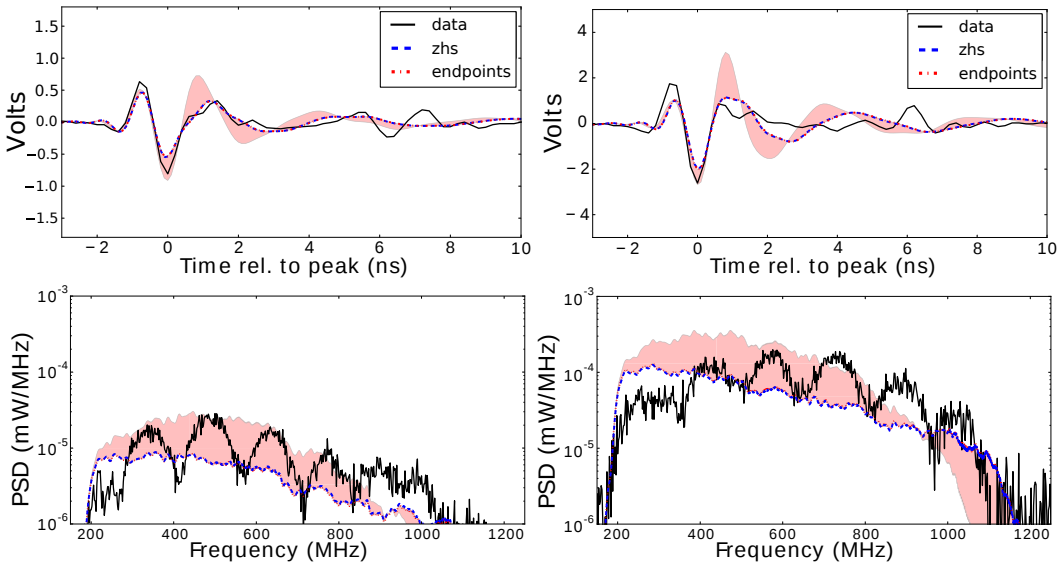

Figure 48: Horizontal (left) and vertical (right) component for an antenna position at 8.4 m height (inside the Cherenkov cone): time traces (top) and frequency domain spectra (bottom). The red band describes the impact of the internal reflection in the simulated result.

in the peak amplitude in the time domain of roughly 30%[1] for an antenna position at the Cherenkov cone. It could be shown that the impact of an internal reflection of the radio signal at the bottom surface of the target leads to an amplification of the measured signal of the same level. Since the reflection properties of the RF-absorbing blanket are not known, a oversimplified assumption has been used to model the impact of reflections, but a consistent description could not be achieved. Finally, after performing the experiment, it turned out that the used RF-absorbing blanket was not suitable because the reflection properties of the blanket were not known in the relevant frequency range.
Nevertheless, it is clear that a follow-up experiment in which the reflections at the bottom surface are fully understood is needed in order to reduce the uncertainty due to reflections in the comparison of the results of microscopic modeling of the radio emission from a particle shower to measured data (see Chapter 6.7).
Internal reflections of the radio signal at other surfaces as the target surface where the beam enters the target are neglected in this study.

In the following, if needed, the impact of the internal reflection of the signal at the bottom surface in the target, as discussed in this section, will be indicated as a red band on top of the simulation results for the endpoint formalism respectively as blue band on top of the simulation results for the ZHS formalism.

6.4 INFLUENCE OF THE MAGNETIC FIELD ON THE RADIO EMISSION

The time-variation of the transverse current of a particle shower is assumed to result in a radio signal. The T-510 experiment can test this hypothesis by reducing the radio signal component induced by the magnetic effect in the measured horizontally polarised compo-

1 Please, note that the value for the discrepancy between the measured and the simulated peak amplitude given in [80] only refers to the horizontal component.

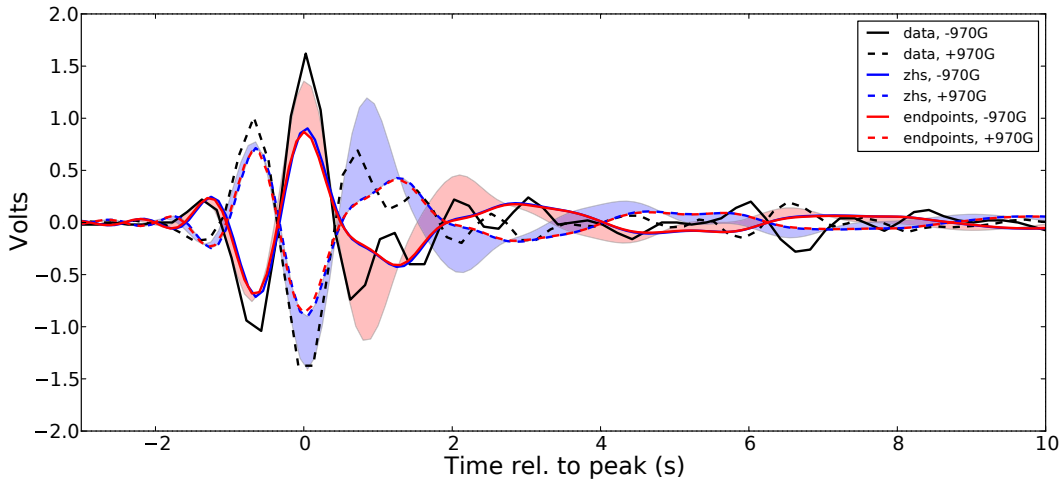

Figure 49: Horizontally polarised component of the radio signal detected by an antenna position at 6.5 m height above the beam line. The component performs a sign flip if the magnetic field induced in the target changes its direction. The time traces were shifted so that the peaks overlap each other. The red band indicates the possible impact of the internal reflection at the bottom surface for the endpoint formalism, the blue band for the ZHS formalism.

nent via manipulation of the induced magnetic field strength and its direction.

The setup of the magnetic coils is designed to create a strong magnetic field perpendicular to the electron beam also. The direction of the field (up and down) can be changed to its opposite by flipping the induced coil's current.

Fig. 49 shows the measured time traces of the horizontally induced component for both magnetic field directions, equivalent to $+970\,\mathrm{G}$ and $-970\,\mathrm{G}$ for an antenna position at a height of 6.5 m. Obviously, the polarity of the measured signal flips when the direction of the magnetic field flips which is also consistently reproduced by the simulations. The maximal amplitude of the signal is not changing, within possible run-to-run fluctuations and sampling effects.
Indicated as the blue (ZHS) and the red band (endpoint), the influence of the internal reflection as discussed in section 6.3 will increase the signal strength for both magnetic field directions in the time domain, but not change their polarity.
For the geometry of the SLAC T-510 experiment, the vertically polarised component of the radio signal is expected to be not affected by the reversed magnetic field direction (see Fig. 50, top right). This assumption turned out to be not correct as explained later.

The flip of the signal polarity of the horizontally polarised component leads to the conclusion that the transverse current of particles in the target, which is assumed to be responsible for radio emission detected in the horizontal channel of the antenna, flows into the opposite direction.

As introduced in Section 4.2 the T-510 experiment is designed to deliver a comparable ratio of the signal strength induced by the Askaryan and the magnetic effect. Since both components of the signal can be distinguished as the Askaryan-induced signal is measured in the vertically polarised component of the antenna (V) and the magnetically induced sig-

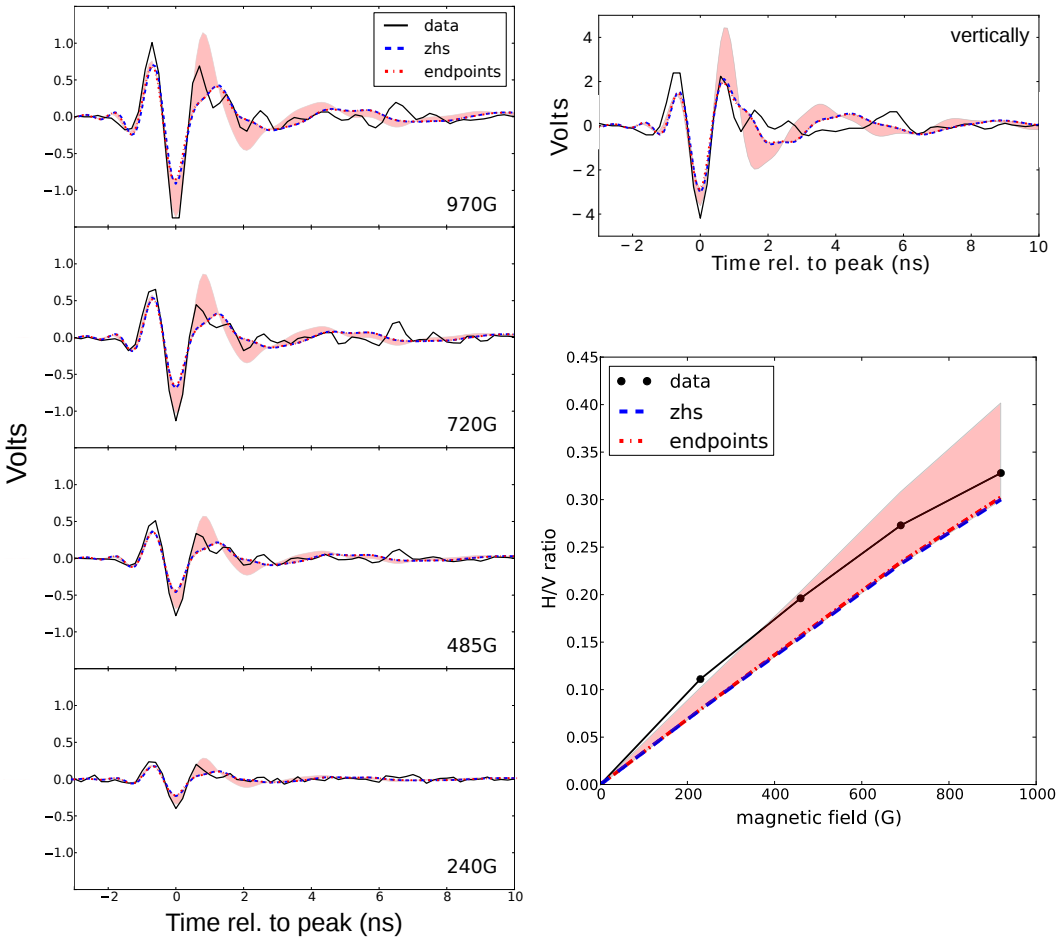

Figure 50: Left: Times traces of horizontally polarised component for different magnetic field strengths. Right, top: Times traces of the vertically polarised component for a magnetic field strength of 970 G (as already shown in Fig. 45). Right, bottom: Ratio of the peak amplitude of the horizontally polarised component to the vertically polarised one for different magnetic field strengths. The red band represents the impact on the simulated H/V ratio by including the reflection. Plot is published in [92] (slightly modified).

nal in the horizontally polarised component (H), the ratio of the peak amplitudes measured in the horizontal and vertical channel, H/V, is studied.

It is expected that the peak amplitude in the horizontally polarised component scales with the magnetic field strength B due to deflection of the shower electrons and positrons and the vertically polarised component is constant as long as the density ρ of the medium stays constant. Fig. 50 (left) shows the time traces of the horizontally polarised component measured by an antenna position at a height of 6.5 m for different maximal induced magnetic strength of $B = 240\,\text{G}, 485\,\text{G}, 720\,\text{G}$ and 970 G. The peak amplitude of the measured time traces as well as the simulated ones rises with an increasing magnetic field strength, as expected. The assumed impact of the internal reflections indicated as the red band also gives a good description of the measured magnetic field dependency of the radio signal. In Fig. 50 (bottom right) the ratio of the peak amplitudes of the horizontally polarised component to the vertically polarised one for the different applied magnetic field strengths is shown. For a linear fit the difference in slope between data and simulation is 20% as performed in [80]. Assuming a possible impact of internal reflection as shown as a red band,

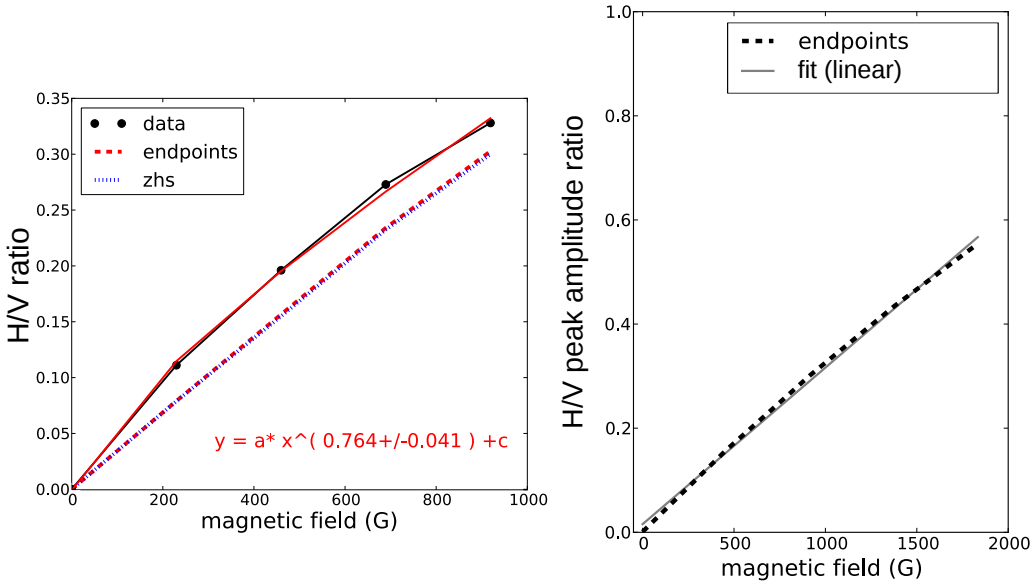

Figure 51: Left: Power-law fit to the H/V ratio for the measured data does not returns an exponent consisting with a linear scaling with the magnetic field strength. Right: A linear function can also not describe simulation results, which are just filtered to $300 - 1200$ MHz. They also contain results for higher magnetic field strengths than in the measurements.

the agreement of the measured and simulated slopes are within the systematic uncertainty due to the reflections. Nevertheless, both, the H/V ratio for data and for simulations, are rising with an increasing magnetic field strength, as expected.

This is an evidence that the transverse current generates the magnetic radio emission.
As described in Chapter 4.2, according the induced ratio B/ρ, the H/V ratio should scale linearly with the magnetic field strength B. But in Fig. 50 (bottom right) a flattening of the measured ratio for the higher magnetic field strengths is observable.
To check this, a fit of a power-law function $y = a \cdot x^b + c$ to the data and the simulations is performed (see Fig. 51). If the ratio scales linearly with an increasing magnetic field strength the exponent b would be 1.
For the simulations using the endpoint formalism the fit returns $b = 0.96 \pm 0.02$ and a value for c consistent with 0 for the direct signal as well as for the one including the impact of internal reflection on the signal. For the ZHS formalism the fit returns a value of $b = 0.95 \pm 0.3$ for the direct signal and 0.98 ± 0.02, respectively, including the impact of an internal reflection, as well as a value for c consistent with 0. These values for the exponent are consistent within their errors to the expectations from a linear scaling. In contrast, a power-law fit to the measured H/V ratio yields a value of the exponent $b = 0.76 \pm 0.04$ which emphasizes a non-linear scaling of the radio emission in dependence of the magnetic field strength (see Fig. 51).
To study this effect in more detail, simulations for a two times higher maximal magnetic field strength of $B = 1940$ G were produced. Since there are no experimental measurements, in the following these simulations are not convolved with detector effects etc. nor internal reflections are included. The simulations are thus filtered from $300 - 1200$ MHz.
The H/V ratio for the simulations, including also the higher magnetic field strengths, are shown in Fig. 53 (left). Also here, a flattening of the ratio for higher magnetic field strengths

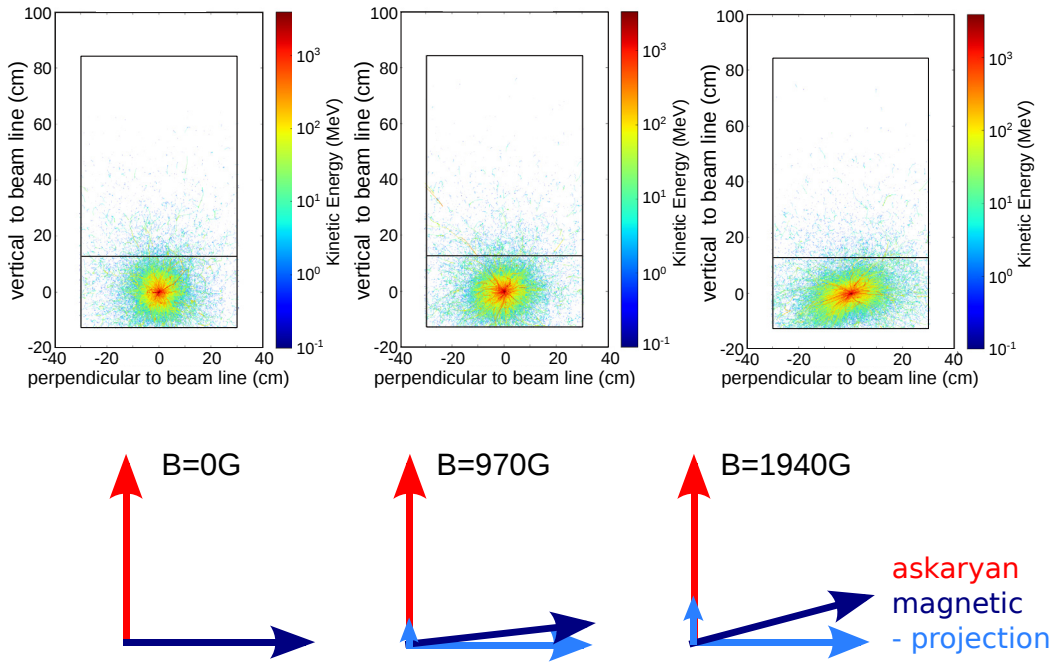

Figure 52: Top: Distribution of particle tracks inside the target for magnetic fields with different strengths: 0 G (left), 970G, G (center) and 1940, G (right). The color-code represents the kinetic energy of the particles. Bottom: Sketch of the orientation of the electric field vectors originating from the Askaryan (red) and the magnetic effect (blue). The light blue vectors represent the projection of the magnetic emission component to the vertical and horizontal channels of the antenna for the different magnetic field strengths.

is observable, emphasized by a power-law fit not reproducing an exponent consistent with $b = 1$.

There are some possible explanations for this non-linear scaling of the ratio: For example, there could be a new effect not observed so far such as a possible saturation of the lateral drift velocity of the particle for rising high magnetic fields. This seems to be an explanation for effects found in simulation studies for air shower measurements [94].
Another explanation would be that due to the strong magnetic field high-energetic particles are deflected out of the target and do not contribute to the radio emission measured at the antenna position. This can be easily tested using the simulations. Fig. 52 shows the distribution of particles in a shower in dependence on their kinetic energy (color-code) induced by electrons with an energy of 4.35 GeV for a magnetic field strengths of 0 G, 970 G and 1940 G, as viewed from the point of the target surface where the particle beam enters. This demonstrates that it is expected that most of the shower is included in the target and no high-energetic particles are escaping.
Besides the spreading of the shower for an induced magnetic field strength of 1940 G, also a rotation of the whole shower is observable. This leads to a third hypothesis for the flattening of the H/V ratio. The rotation of the shower leads to the conclusion that also the electric field vectors of the emitted magnetic radio emission can be rotated. In that case the contribution from the Askaryan and the magnetic effect to the electric field can not be separated anymore: The horizontally and vertically polarised components are not independent of each other.

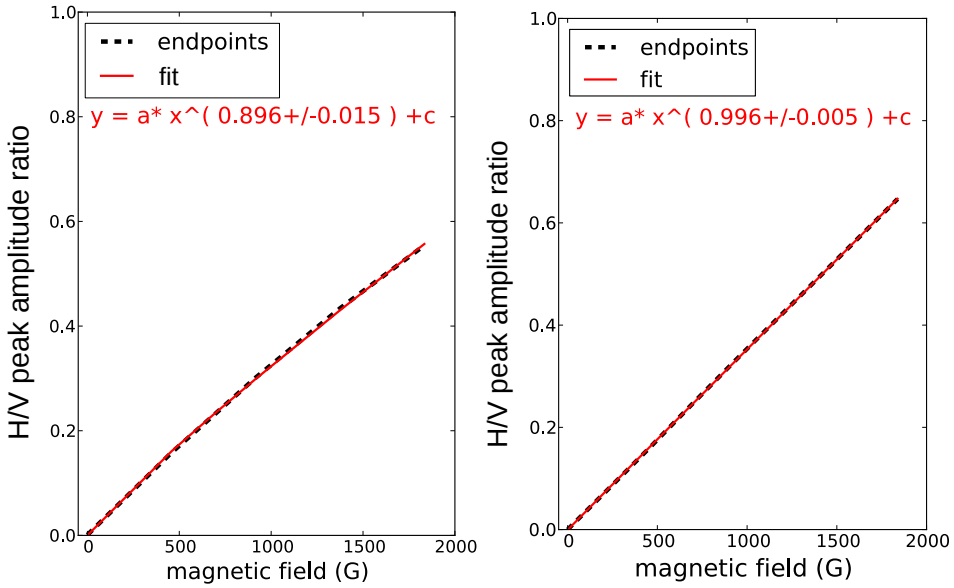

Figure 53: Power-law fit to the H/V ratio for simulations, filtered from $300 - 1200$ MHz: Left: Simulation including the measured magnetic field map scaled to different magnetic field strengths. Right: Simulation including a uniform magnetic field map, pointing into the vertical direction perpendicular to the beam line and scaled to different magnetic field strengths.

The Askaryan radiation is still radially oriented around the shower axis, but the magnetic radiation is linearly polarised along the direction of the Lorentz force, given by $\vec{v} \times \vec{B}$ (see Sec. 3). Therefore, the emission due to magnetic field is not just measured in the horizontally polarised component of the antenna. It is measured as a projection into the horizontal component as well as in the vertical component. So, the signal in the horizontal component is observed to be slightly smaller than expected. The signal is decreasing with higher magnetic field strength and a larger shower rotation, as indicated in Fig. 52 (bottom).

This hypothesis can be tested by running simulations with a uniform magnetic field with a field vector pointing to the vertical direction perpendicular to the beam. The particle distribution for a magnetic field strength of 1690 G in Fig. 54 does not show a rotation of the shower, but just a spreading of the shower perpendicular to magnetic field direction. This magnetic field strength was chosen since is it two times larger than the average measured magnetic field strength of $B = 845$ G along the beam line in the realistic three-dimensional setup. The resulting H/V ratio for different magnetic fields are shown in Fig. 53 (right). A power-law fit returns an exponent $b = 0.99 \pm 0.01$ which is consistent with an exponent of $b = 1$ for a linear scaling of the H/V ratio depending on the magnetic field strength.

This is a clear evidence that the realistic magnetic field leads to a rotation of the particle shower. Although the measured magnetic field distribution has its largest contribution vertical to the beam direction, it consists also of small contributions to the magnetic field towards the horizontal and the along-the-beam-line direction so that the showers electrons and positrons are not only deflected into the perpendicular direction to the beam line. In total, this leads to a misalignment of the horizontally polarised radiation emitted by the magnetic effect to the horizontal channel of the antenna. The magnetic emission is measured

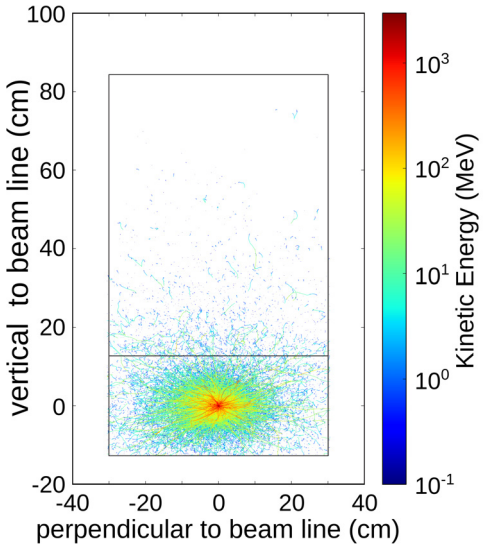

Figure 54: Distribution of particle tracks inside the target for a uniform magnetic field strength of 1690 G in vertical direction to the beam line. The color-code represents the kinetic energy of the particles.

as a projection into the horizontal as well as vertical antenna channel whose signal are then not independent anymore. An additional point is that the magnetic field strengths are just measured at beam height. This means that the distribution above and under this height are just assumed to be consistent with the measured value and could have an additional effect on the results for the scaling of the radio signal with the magnetic strength.

Based on the measurements, it could just be shown that with rising magnetic field strength also the signal strength of the emission related to the magnetic effect increases. This could also be predicted using the endpoint and ZHS formalisms. The expected linear scaling could not be confirmed due to the rotation of the particle shower in the realistic magnetic field and therefore the rotation of the electric field vector of the magnetic emission.
The impact of the internal reflection could intensify the effect of flattening of the H/V ratio in the measurements. Simulations including first reflection, as shown in Fig. 50 (bottom right) as a red band, leads to a higher H/V ratio in the simulations. This error band due to reflection includes the data. But, the impact of reflection at the bottom target surface is handled similarly for the horizontally and vertically polarised component. As already discussed, the assumptions of a a total reflection for all frequencies is too simple since the impact of the internal reflection is not fully understood.

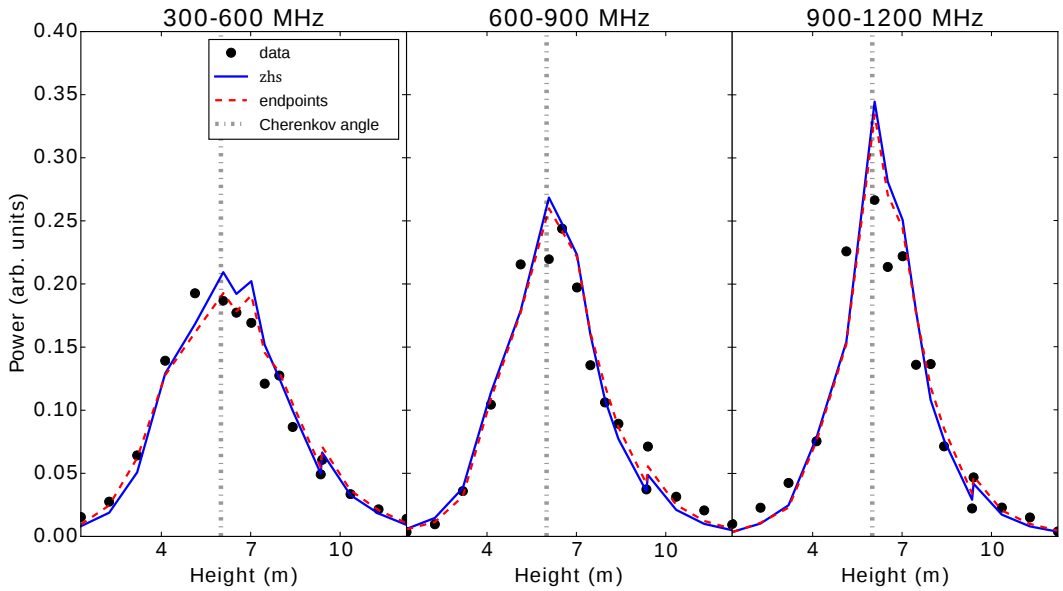

Figure 55: Scan of the vertically polarised component along the vertical axis for three frequency bands at 970 G without inclusion of the reflections, normalised by its total power [95]. Here, each curve is normalised to the area under each curve. The gray, dashed line indicates the expected position of the Cherenkov peak.

6.5 A SCAN OF THE CHERENKOV CONE

Several aspects indicate that the radio emission from a particle shower forms a cone as already introduced in Chapter 3. A scan across the Cherenkov cone to measure the angular radiation pattern was already performed in a former experiment [41] showing that radiation by a particle shower in a dense medium due to the Askaryan effect forms a cone with its peak at the position according to the refractive index of the medium.
To measure the angular radiation pattern in the SLAC T-510 experiment, a scan along the vertical axis with respect to the beam was performed by placing the antenna tower at different heights.
Fig. 55 and Fig. 56 show the power profile for the vertically as well as the horizontally polarised component of the radio signal along the vertical axis for the measured data and the simulations, split up in different frequency bands. Each power profile is normalised to the area under each curve.

Fig. 55 shows a comparison of the measured data of the T-510 experiment with results from microscopic simulations for different frequency bands. It is observable that the vertically polarised component dominated by the Askaryan emission forms a Cherenkov cone whose peak position at a height of 6.5 m to the beam line is in agreement with the theoretical expectations. The Cherenkov cone and the expected peak position are also observed in the simulated results, based on the endpoint formalism as well as the ZHS formalism. The horizontally polarised component of the radio signal which is assigned to the magnetic effect forms also a Cherenkov cone as shown in Fig. 56 for different frequency bands. The measured peak position of 6.5 m is consistent with the predictions by the simulations which reproduce a Cherenkov cone for the horizontally component as well.

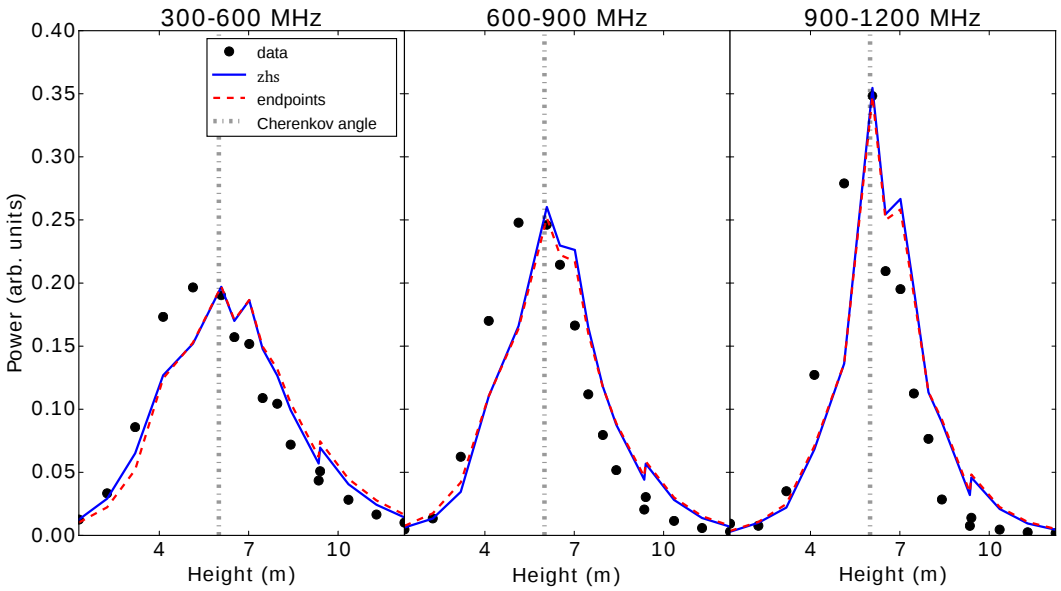

Figure 56: Scan of the horizontally polarised component along the vertical axis for three frequency bands at 970 G without inclusion of the reflections (adapted from [80], modified). Here, each curve is normalised to the area under each curve. The gray, dashed line indicates the expected position of the Cherenkov peak.

This agreement of the simulations with the data for both polarisations leads to the conclusion that the first-principle simulations can reproduce typical effects which are expected from radiation, like the Cherenkov-like effects. The prediction of the peak position by the simulations agrees with theoretical expectations of 6.5 m as well as with the measured position. This shows that the refractive index of the medium of the shower development as well as of the radio signal propagation is important for an accurate modeling of electrodynamics.

For both polarisations the scan of the Cherenkov cone is split up into the frequency bands of $300 - 600$ MHz, $600 - 900$ MHz and $900 - 1200$ MHz. In that way, it is observable that the width of the single Cherenkov cones for the vertically as well for the horizontally polarised components scales with the inverse of the frequency ($1/f$) so that the Cherenkov ring becomes better defined for higher frequencies. The narrowing of the measured cones shows that the emission is coherent up to high frequencies (see Chapter 3). The reproduction of this frequency behavior underlines the ability of microscopic simulations to predict radio emission from particle showers.

The comparison of the measured data and the simulations shows an accurate prediction of the absolute scale of the radio signal with different systematic uncertainties compared to air shower experiments. Nevertheless, a slight asymmetry of the cones, visible as a shift between the measured cone and the simulated cones, is observable. This could be explained by diffraction effects in the target, whose impact would change with the height of the antenna, as well by the internal reflections at the bottom surface which seem to depend on the frequency and the incident angles. Both effects are not included in the simulations.

Since it has been already shown that the modeling of the impact of the internal reflec-

tions at the bottom surface is based on too simple assumptions, the impact of reflections as described in Section 6.3 for the single antenna positions is not included in this comparison.

6.6 POLARISATION CHARACTERISTICS OF THE RADIO SIGNAL FROM PARTICLE SHOWERS

Since the radiation from a particle shower is produced by the Askaryan and the magnetic emission mechanisms (see Section 3) their two components to the radio signal can possible originate from different parts of the shower. In other words, since the relative strength of the two contributions is not constant in time, it is expected that their peaks in amplitude do not arrive simultaneously at the observers position so that they are not in phase [56].
The electric field vector, which would generally trace a line in the plane perpendicular to the shower if the radiation coming from the two emissions mechanisms were in phase, will trace an ellipse for particular positions where the emission from Askaryan and magnetic effect is not completely aligned. This means that in general the radio emission from particle showers is expected to have an elliptical polarisation which is a mix of linear and circular polarisation, as also predicted by simulations [56]. LOFAR [49] could prove this effect experimentally for air showers.
Whether this asynchronisation of the peak arrival time of the two mechanisms can be also predicted correctly using the endpoint or ZHS formalism was checked in the following:

The measured signal is sampled with 5 GHz which leads to a time binning of 0.2 ns while the convolved simulations are sampled with 10 GHz which leads to a time binning of 0.1 ns. In Fig. 57 the evolution of the amplitude with time of the vertical component against the one of the horizontal component for the data measured at an antenna height of 6.5 m to the beam and the corresponding convolved simulations are shown. For the measured data as well as the convolved simulations, the electric field vector traces an ellipse which indicates that the radio signal from the particle shower is elliptically polarised. For the simulations, this behavior is also observable when including the internal reflections. For a closer look, Fig. 58 shows a comparison for the measured and simulated time traces of both signal components. After determining the arrival times of the peak amplitudes of each component at the antenna, one notices that there is a time shift of 0.4 ns between the data peak in the vertical component and the data peak in the horizontal component with the horizontally polarised part of the radio signal arriving first at the antenna. As already visible, for the convolved simulations the vertically polarised signal arrives first. For the simulations using the endpoint formalism the time difference between the vertically and the horizontally polarised component is 0.3 ns while for the simulations using the ZHS formalism it is even larger with 0.5 ns. These time differences do not change when the internal reflection is included.
So, there seems to be a small time shift between both components of the radio signal in the data as well as in the convolved simulations even if it is expected that the radio emission of the whole shower arrives at the Cherenkov angle simultaneously. In addition, open questions are why the arrival times of the single components are reversed for the data and the simulations and why there is a difference between the endpoint and the ZHS formalism.

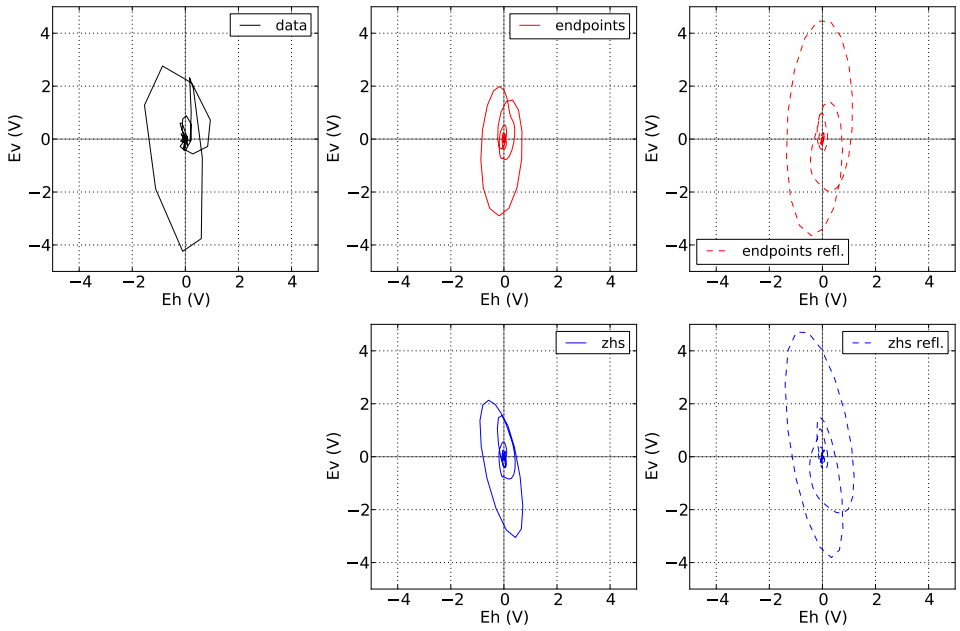

Figure 57: The time-dependence of the electric field vector for measured signals and convolved simulations: Vertically polarised component (Ev) vs. horizontally polarised component (Eh). Left: Measured signal at an antenna height of 6.5 m. Center: Convolved simulations for the endpoint (red) and the ZHS simulations (blue). Right: Convolved simulations including the reflection at the bottom target surface.

These questions led to a follow-up analysis of the the arrival times of the peak amplitudes of the measured data for different antenna heights (see Fig. 59). It appeared that the time difference for the vertical and horizontal component measured with the 4 antennas of the antenna tower have always an offset in time. While for the antennas 1 and 2 the horizontally polarised component of the radio signals seems to arrive first, in the antennas 3 and 4 the vertically polarised component is measured to be first. In addition, there seems to be not a constant offset, but it seems to depend on the antenna height as well. It turned out that the lengths of the cables connected to the two channels of each antenna are not exactly known which could lead to an artificial time shift in the data. It is also not clear whether the two used oscilloscopes for data taking, with a resolution of 0.2 ns, handles the measured signals slightly different. A measurement of the delays between the horizontal and the vertical channel at the antennas returned a time difference of 65 ps which is negligible.

Hence, the time calibration of the experiment is not precise enough to study the polarisation of the signals. It is unclear if the observed degree of elliptical polarisation is an inherent feature of the emission or possibly an artifact of the measurement.

Also, the detector description which goes in the convolution of the simulations, is not able to reproduce the effect of the timing as observed in the data. In addition, due to the time

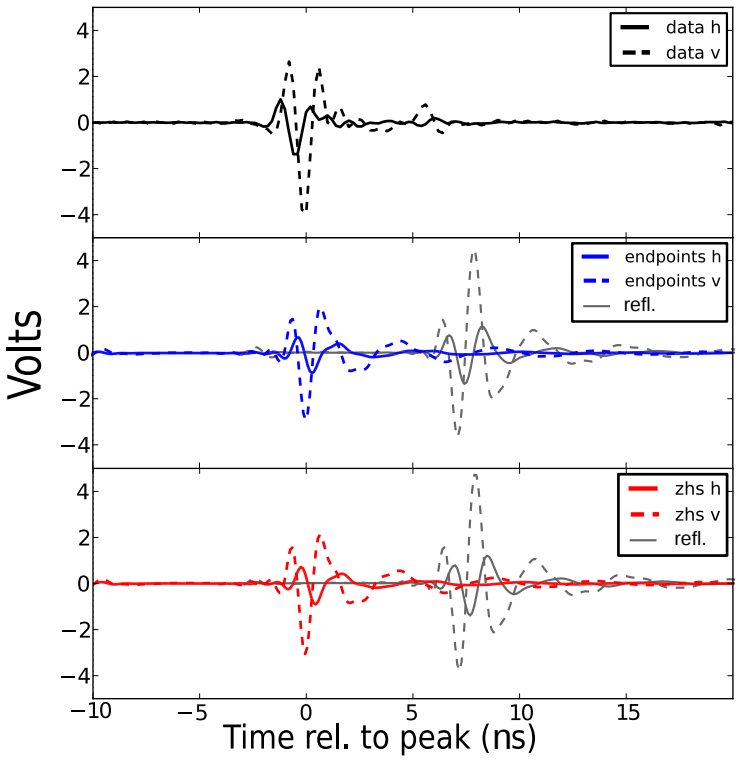

Figure 58: Comparison of the time traces measured at an antenna height of 6.5 m to the corresponding convolved simulations. The time traces for the simulations including the internal reflections (gray) were shifted by a few ns for a better separation.

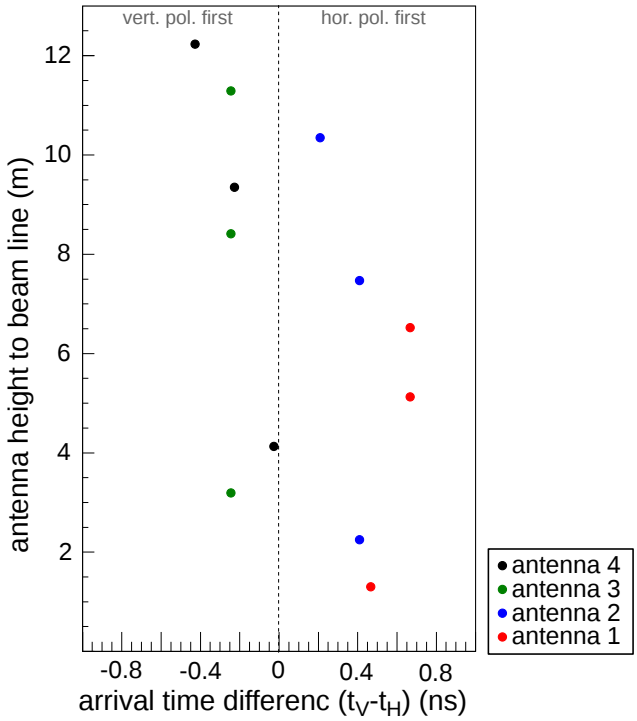

Figure 59: The difference in the peak arrival time of the single components for the different antenna heights. The colors represent the particular antennas at the antenna tower.

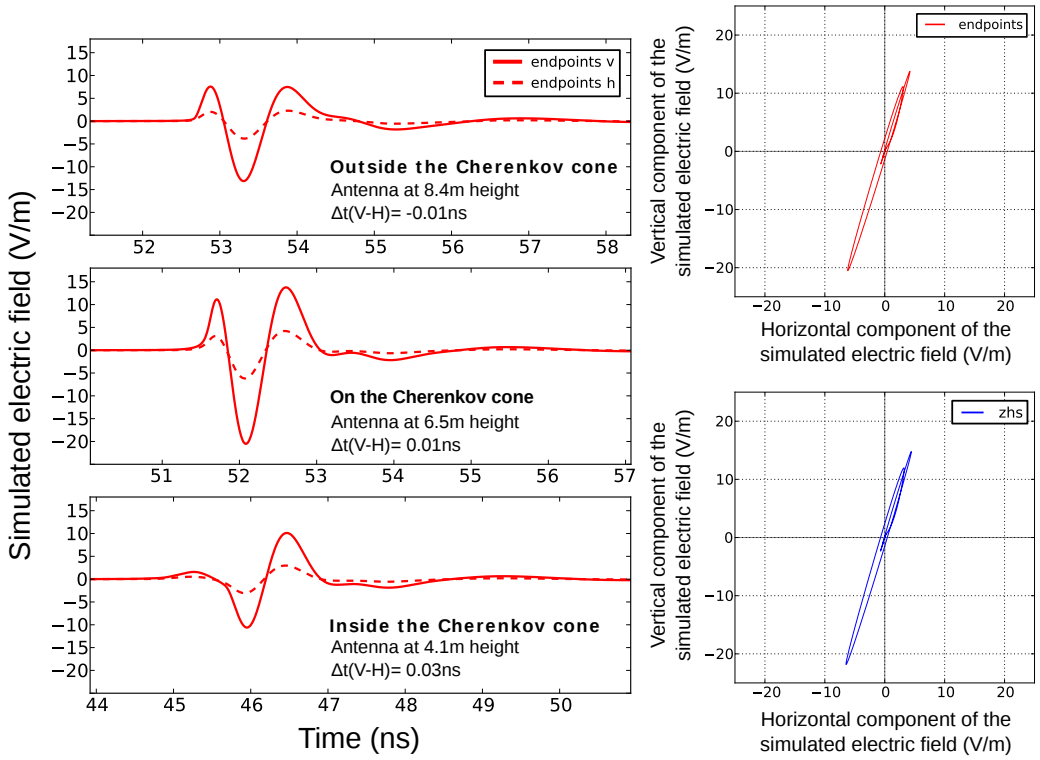

Figure 60: Left: Simulation using the endpoint formalism, filtered to 300 – 1200 MHz filtered. Time traces of the vertically (v) and horizontally (h) polarised components for different antenna heights. Right: Simulation using the endpoint (top) and the ZHS formalism (bottom) showing the time evolution of the vertical component over the horizontal one.

differences it seems that the simulations using the ZHS formalism and using the endpoint formalism are handled differently. This could be located for example in the derivation of the electric field from the vector potential for the ZHS formalism.

This point is emphasized by looking at the simulated times traces, just filtered to 300 – 1200 MHz and a time binning of 0.01 ns (see Fig. 60, left center). For an antenna on the Cherenkov cone, the peak amplitude of the vertically polarised component arrives 0.01 ns later than the one of the horizontally polarised component, for the simulations done with the endpoint formalisms as well as for the ZHS formalism. So, the discrepancy as observed for the convolved simulations is not present when the pure simulation results without the simulated detector response are studied. Fig. 60 (right) also shows the time evolution of the simulated amplitude of the vertical component against the horizontal component for both formalisms. Here, the electric field vector traces a line as expected for an antenna on the Cherenkov cone. Both components of the radio signal arrive simultaneously. The radio signal is linearly polarised and does not include a significant contribution of a circularly polarised component. The elliptical polarisation of the measured radio signal thus seems to be just an artifact of the measurements.
In a more detailed study, it is shown that the time difference of 0.01 ns originates from the magnetic field and is not an artifact of the time-binning of 0.01 ns in the simulations. Fig. 61 shows the time traces for the vertically and horizontally polarised components measured by an antenna at 6.5 m height for induced magnetic fields with different strengths. For a

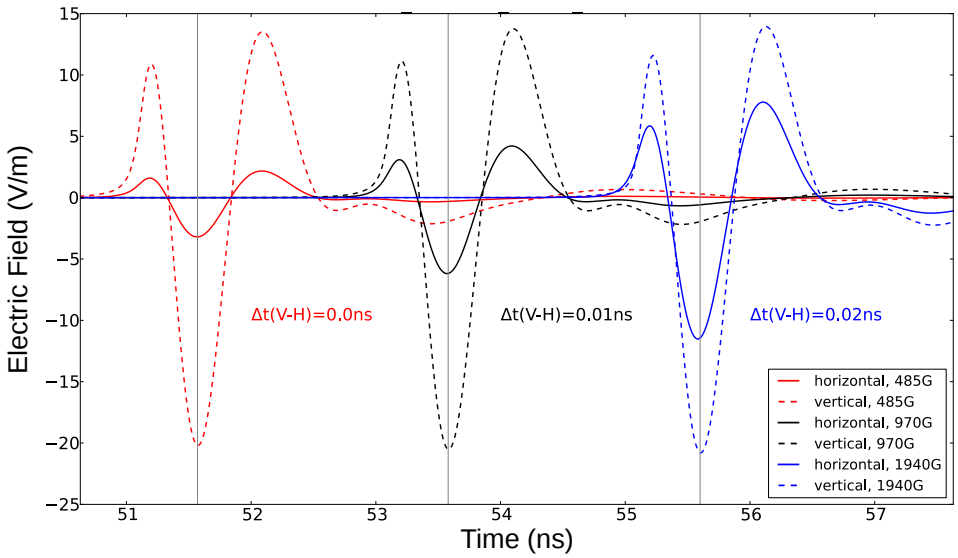

Figure 61: Simulations using the endpoint formalism, filtered to 300 – 1200 MHz: time traces for the horizontally and vertically polarised component for an antenna position on the Cherenkov cone. The time traces for different magnetic field strengths are shifted in time to each other. The vertical lines mark the peaks for the single vertically polarised components.

magnetic field strength of 485 G there is no difference in the arrival times for the two components, while for a magnetic field with strength of 1940 G there is a difference of 0.02 ns. This leads to the conclusion, that the induced magnetic fields leads to a shift in time of the single components of the radio signal. But the effect on a level of $1/100$ ns should not be overvalued.

Another interesting aspect to study is the behavior of the arrival time of the two components while crossing the Cherenkov cone (see Fig. 60). For an antenna position inside the Cherenkov cone, it can be observed that the horizontally polarised component arrives first. As for an antenna position at 4.1 m the time difference for the peak amplitude of the vertically polarised component to the horizontally polarised one is 0.03 ns. Outside the Cherenkov cone the arrival times are reversed. For an antenna position at 8.4 m the time difference for the peak amplitudes of the vertically polarised component to the horizontally polarised one is 0.01 ns and the vertically polarised component arrives first. This was expected since outside the cone the emission from the target starting point should arrive earlier and inside the emission from the target end should arrive first. This is consistent with the results discussed in Chapter 5.4.3.

Due to the fact that the particle shower develops at space scales of meters the differences in time are minimal and not significant with respect to the resolution of time measurement. In particular, these time differences at scales of $1/100$ ns are not detectable so that this study can be just performed at the simulation level. Furthermore, the SLAC T-510 experiment was not designed to be a time precision experiment, but to compare the scales of the electric field strengths. Therefore, no final conclusion can be made.

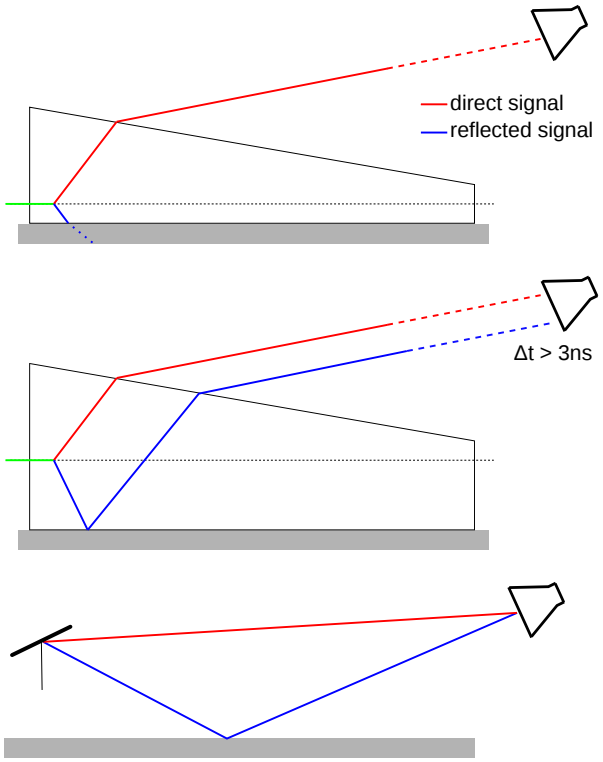

Figure 62: Possible setups for future measurements to reduce the uncertainty in the comparison to simulations due to internal reflections. The red line represents the direct signal while the blue line shows the propagation of the reflected signal.

6.7 IDEAS FOR FUTURE EXPERIMENTS TO IMPROVE THE MEASUREMENTS AND ITS COMPARISON TO SIMULATIONS

For the SLAC T-510 experiment, it turned out that the incomplete understanding of the internal reflections at the bottom surface of the target led to the main limiting factor in the comparison of the measured data with the simulations. A fully consistent inclusion of the reflections in the simulations of the signal is not possible since the reflection characteristics of the blanket which lay under the target are not known at the relevant frequencies below 1 GHz.

To reduce the current uncertainty of about $30-35\%$ in the comparison of the peak amplitudes, additional measurements are needed. There are various ideas (see Fig. 62):
The same experiment could be repeated, just replacing the current blanket by an absorber with known qualities. Even if not all emission radiated towards the bottom surface would be absorbed, a treatment in the simulations would be possible. Another idea is to design a new, larger target ensuring that the direct and the reflected signal are clearly separated in time when arriving at the antenna so that they do not overlap and the reflections can be windowed out. A third idea is to measure the characteristics of the existing blanket. This can be done by using e.g. a dipole antenna which produces a well-known radio signal. A horn antenna can be used as an detector which will measure the direct signal from the dipole antenna as well as the reflected signal coming from the blanket. The two measured signals can be compared to each other and the effect due to reflections can be isolated. The

challenge is to scan all frequencies included in the SLAC T-510 analysis, also for different angles, i.e., different antenna heights (compare to Chapter 6.3).
If the reflection properties for all these parameters would be known, they could be included directly in the simulations.

6.8 SUMMARY AND CONCLUSION

The SLAC T-510 experiment is the first experiment which provided a laboratory benchmark for radio frequency radiation from electromagnetic cascades under the influence of a strong magnetic field. The measured radio emission from a well-defined particle shower, with known primary energy and known beam charge, developing in a well-defined target of known geometry was compared to predictions from microscopic simulations which rely on first principles of electrodynamics and have no free parameters. These simulations were prepared and performed in the context of this thesis. The parameters of the experiment such as the target material and the strength of the magnetic field were chosen in such a way that the results of the comparison of data and simulations can be scaled to the relevant frequency ranges for air shower detection. While this experiment does not exactly replicate the physics of an extensive air shower, a good agreement of the predictions and the measurements insures the applicability of the conclusions to air shower detection. In addition, since this experiment was a fixed target experiment using a known electromagnetic shower, it can confirm the validity of the prediction of microscopic calculations with different systematic uncertainties than air shower measurements like uncertainties in the hadronic interaction models.

The two formalisms, the endpoint and the ZHS formalism, which were included in the detailed simulation study for the SLAC T-510 experiment, could reproduce the electric field strength for the antenna positions consistently within 5%. Implemented into the particle simulations in parallel, it is shown that these two formalisms agree with each other. A comparison to measured data led to the conclusion that both models can predict the absolute scale of the radio signal produced by a particle shower accurately within the uncertainties of the experiment of roughly 30%.
In addition, it is also demonstrated that an internal reflection at the bottom surface explains the apparent discrepancy of the measured data to the predictions. The reflection is found to be the dominating uncertainty of the experiment. Since currently the assumptions on the reflection for its inclusion in the comparison of the data and the simulations are too simple, a follow-up study is needed to reduce the experimental uncertainties.

Nevertheless, the SLAC T-510 experiment could prove the transverse current of particles in the target to be responsible for radio emission. By reversing the direction of the induced magnetic field, the radio signal component assigned to the radio emission produced by the magnetic effect flipped its polarity as well.
In addition it could be demonstrated that the radiation in this component grows with a rising magnetic field strength. From theory (see Chapter 4.2) the scaling is expected to be linear which was not observed in the data and the simulations. Based on the simulation study, this could be explained by the non-uniformity of the magnetic field as well as the impact of

the internal reflections on the signal.

The SLAC T-510 experiments also measured a Cherenkov cone for the vertically as well as for the horizontally polarised component of the radio emission which was also reproduced by the simulations. The peak positions of the measured and the simulated cones agree with the geometrical expectation. This emphasizes the importance of the refractive index in the accurate modeling of radio emission from particle showers. In addition a narrowing of the cones for higher frequencies is observed which is also predicted by the simulations. This shows the ability of microscopic simulations to predict radio emission from particle showers.

The comparison of the measured data and the convolved simulations indicated that the radio emission from the particle shower might be elliptically polarised as already observed in air showers. This could not be proven to be true. Since simulations only undergone a bandpass filter and no detector simulation showed a linear polarisation with no significant contribution of a circular polarisation, the conclusion is that the elliptical polarisation is just an artifact of the measurement and is introduced by the convolution of the simulations with the detector response. The SLAC T-510 experiment was not planned to be a precision experiment in timing so that there is a high possibility that the time shift between the horizontally and vertically polarised components is due to small differences in the cable lengths.

The SLAC T-510 experiment in comparison with its detailed simulation, which was performed in the scope of this thesis, could provide a strong evidence that simulations based on electrodynamics can be used to reliably predict the radio emission of extensive air showers. Since the implementation of the endpoints formalism in Geant4 is equivalent to the CoREAS code, also the application of the CORSIKA plug-in was tested implicitly. The large uncertainty of the experiment of roughly 30% is not yet competitive with air shower measurements, but a follow-up experiment can reduce them significantly.

For the interpretation of the measured data of air-shower experiments a reduction of the uncertainties in the predictions of the radio signal is necessary, especially for future high-precision experiments in the radio detection of cosmic rays such as the SKA1-low antenna array which will sample the radio footprint on ground with extreme resolution.

7 GOING TO EXTREME PRECISION MEASUREMENTS: DETECTING COSMIC RAYS WITH SKA1-LOW

In the context of this thesis, principle ideas, as presented in this chapter, as well as some figures and preliminary results, were already published in:

- T. Huege et al. "Enabling detection of cosmic ray air showers with SKA-low", Engineering Change Proposal submitted to the SKA organisation [96],
- T. Huege et al., "High-precision measurements of extensive air showers with the SKA" in the proceedings of the 34th International Cosmic Ray Conference (ICRC 2015) [97],
- T. Huege et al.,"Ultimate precision in cosmic-ray detection - the SKA" in the proceedings of the 7th Acoustic and Radio EeV Neutrino Detection Activities (ARENA 2016) [98],
- A. Zilles, S. Buitink and T. Huege, "Initial simulation study on high-precision radio measurements of the depth of shower maximum with SKA1-low" in the proceedings of the 7th Acoustic and Radio EeV Neutrino Detection Activities (ARENA 2016) [99].

With minor engineering changes, the phase 1 of the low-frequency part of the future Square Kilometre Array can be easily enabled for air-shower detection and can then perform high-precision measurements of the mass composition of the cosmic ray flux in the energy region of about $\approx 10^{16} - 10^{18}$ eV. The accessible energy range arises since for low energies the radio signal is dominated by the Galactic noise and for higher energies the effective area is too low for reasonable statistics.

In the context of this thesis, the potential of air-shower detection with SKA1-low was evaluated on the basis of simulations. An already developed and already successfully tested method for the reconstruction of the mass composition of cosmic rays as used by LOFAR will be used. Adapting this method, first results demonstrate that a reconstruction of the shower maximum, a parameter which is sensitive to the mass of the primary particle, can be determined with a mean uncertainty of less than $10\,\mathrm{g/cm^2}$ ($\sim 20\,\mathrm{g/cm^2}$ for fluorescence light detection [36]) so that a decomposition of the flux of cosmic rays in the transition region of Galactic to Extragalactic origin into individual elements seems to be feasible. Besides a precision study of transition from a Galactic to an Extragalactic origin of cosmic rays, measurements on hadronic interaction, such as the proton-air cross section, and on air shower physics beyond LHC energies can be performed with high precision since a separation of proton and helium nuclei seems to be feasible. In addition, since SKA1-low will sample the radio footprint on the ground in a detailed way, a "tomography" of the air shower by using near-field interferometry seems feasible as well. In addition to precision measurements of extensive air showers, this will allow to study the physics of thunderstorms and their connections with air showers.

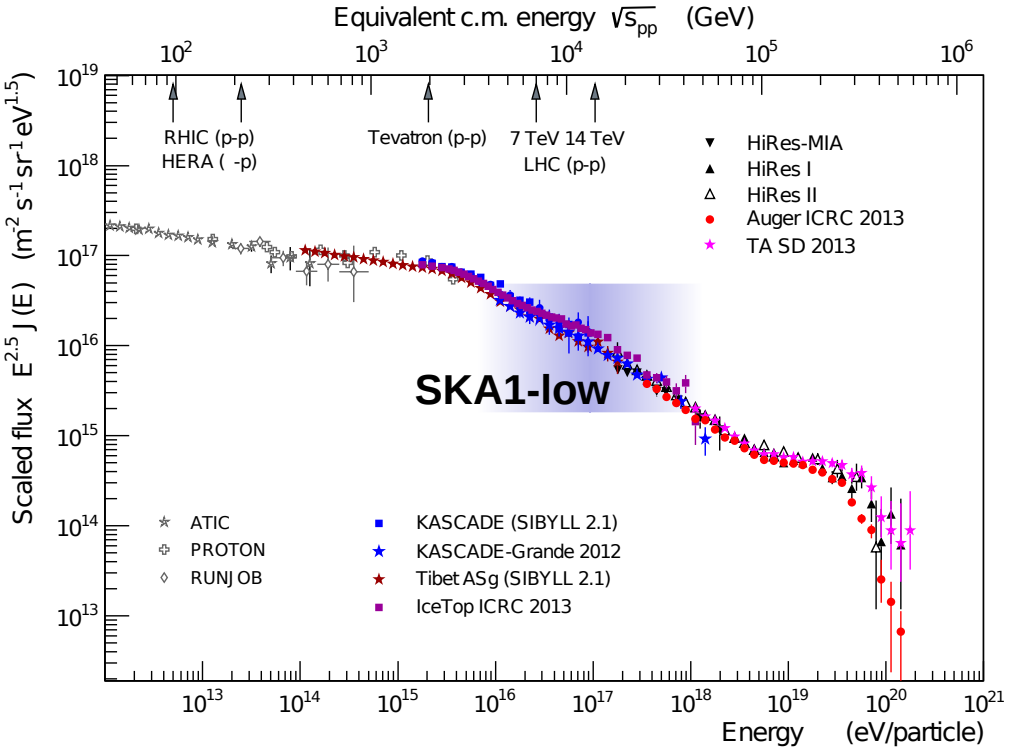

Figure 63: The energy spectrum of cosmic rays (compilation from [15], modified). The SKA will be able to measure the air showers induced by primary particles of the energy of $10^{16} - 10^{18}$ eV.

7.1 EXPERIMENTAL SETUP

The low-frequency core of the future Square Kilometre Array (SKA-low) will be located in West-Australia at an altitude of about 370 m. There, the Earth's magnetic field has a strength of 55.5 μT and is inclined by 60°. With almost 70.000 antennas on an area of less than 0.44 km^2 in a circle with diameter of 750 m, it will be the densest antenna array of the world. The dual-polarised antennas with North-South and East-West polarisation will be sensitive to frequencies from 50 – 350 MHz. The sampling rate of SKA-low is 800 MHz. Phase 1 of the low-frequency part of SKA (SKA1-low) will be built as of 2018 with the planned completion in 2023. The first operation is planned for 2020. Some technical design modifications in the data-acquisition system and the deployment of a simple particle-detector array for triggering are necessary to enable SKA1-low for cosmic ray detection. More details can be found in Section 7.1.1.

Information on the preliminary design of the SKA1-low core can be found in the configuration report by the SKA organisation [100]. The design of the core is provided by the defined goals of SKA1-low in the field of radio astronomy. Therefore, a production of a multi-level hierarchical station design is required. This is performed by tiling elements having a prime number of edges avoid any 180° rotation symmetry.

The smallest unit is formed on a pentagonal area with an diameter of about 10 m, the

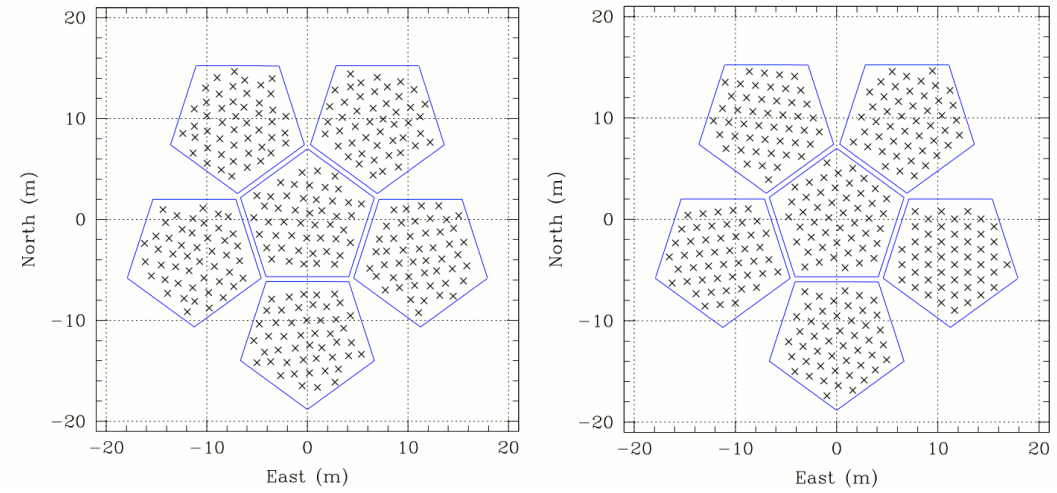

Figure 64: Two possible layouts for a station [100]. Six sub-stations form one station, either including randomisation of the antenna positions within a sub-station (left) or using a non-aligned triangular grid (right). The antennas within a sub-station have a mean separation of roughly 1.5 m.

so-called sub-station. It is highly packed consisting of 48 antennas in total. For the positioning of the antennas there are two different layouts, both assuming a mean distance of about 1.5 m in-between the single antennas. This corresponds to $\lambda/2$ at 100 MHz. One option is to distribute the antennas randomly in the pentagon, the other one is to choose a triangular grid structure (see Fig. 64). Six sub-stations form a so-called station with one sub-station as a central station surrounded by five other ones. Such a sub-station covers an area with a diameter of about 30 m. Following this schema, six of these stations are arranged as one so-called superstation (see. Fig. 65) with one station in the center and five stations positioned around it. A superstation has a diameter of about 90 m.
In total the core of SKA1-low, displayed in Fig. 66, consist of 40 superstations which leads to a total number of antennas of 40 (superstations) $\times$6 (stations) $\times$6 (sub-stations) $\times$48 antennas $=$ 69120 SKA1-low antennas.

For simplicity, in the following simulation study, the regular positioning of antennas in a sub-station is chosen as the presumed layout for the future SKA1-low array. Whether the antenna positions are randomised or regularly distributed in a sub-station is not expected to have any significant effect on the measurements of an air shower as long as the antennas measuring a signal are homogeneously distributed with respect to the radio footprint on ground.

7.1.1 Engineering changes

Since SKA1-low was designed as a radio astronomy telescope, some engineering changes are needed to enable SKA1-low for air-shower detection.
All required changes to the original SKA1-low design are listed and discussed in [96]. Here, a summary of the most important changes are given.

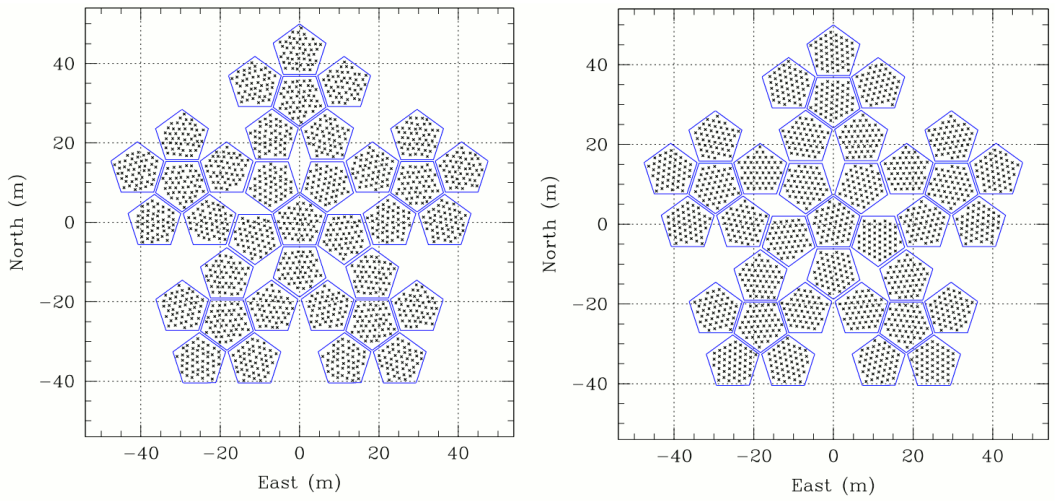

Figure 65: Two possible layouts for a superstation [100]. Six stations form one superstation, either including randomisation of the antenna positions within a sub-station (left) or using a non-aligned triangular grid (right).

7.1.1.1 Triggering with particle detectors

For the follow-up analysis of the SKA1-low analysis, the measured raw data for an air shower event, coming from the Analog-to-Digital Converters (ADCs) without any additional precessing step such as channelising, is needed. Buffers at the single antennas will store the raw data until a trigger from the particle detector array is received.

A powerful real-time analysis of the SKA1-low data would be required to perform a radio-only trigger on air shower events for the read-out of the antenna data. This would require a higher detection threshold to be efficient and pure, and would probably lead to a high rate of false positive triggers.

A particle detector array is a straight-forward option to provide a pure trigger designed to become efficient at 10^{16} eV. At this energy, and for an instrumented area of 1 km^2, the expected trigger rate is about 1 event in 60 seconds with a Poissionian time distribution.
The future particle detector array is planned to have 180 detection modules, originally used in the former KASCADE experiment [3]. The array will cover the whole SKA1-low core on a semi-regular grid, trying to achieve distances of roughly 50 m between the modules. A possible layout is shown in Fig. 67 (left). The radius of the whole array will exceed the one of the SKA1-low core by about 200 m to optimise the trigger rate, and extend the effective area of SKA1-low as a cosmic ray detector to roughly 1 km^2 so that also air-shower events having an impact position outside of the SKA1-low core can be triggered.
The layout of a single particle detector module is shown in Fig. 67 (right). Each module will cover 3.7 m^2 and will be 3 cm thick. It consists of 4 plastic scintillator plates in which air shower particles produce scintillation light while passing. This light is collected with wavelength shifting bars and led towards 4 Silicon Photomultipliers (SiPMs). Each module is shielded from light in a metal box of a size of about 2 m $\times$ 2 m $\times$ 15 cm.
As already mentioned, the expected rate of air shower event triggers is about 1 every minute. The arrival time of air showers follows a Poissionian distribution. Fig. 68 (right) shows the

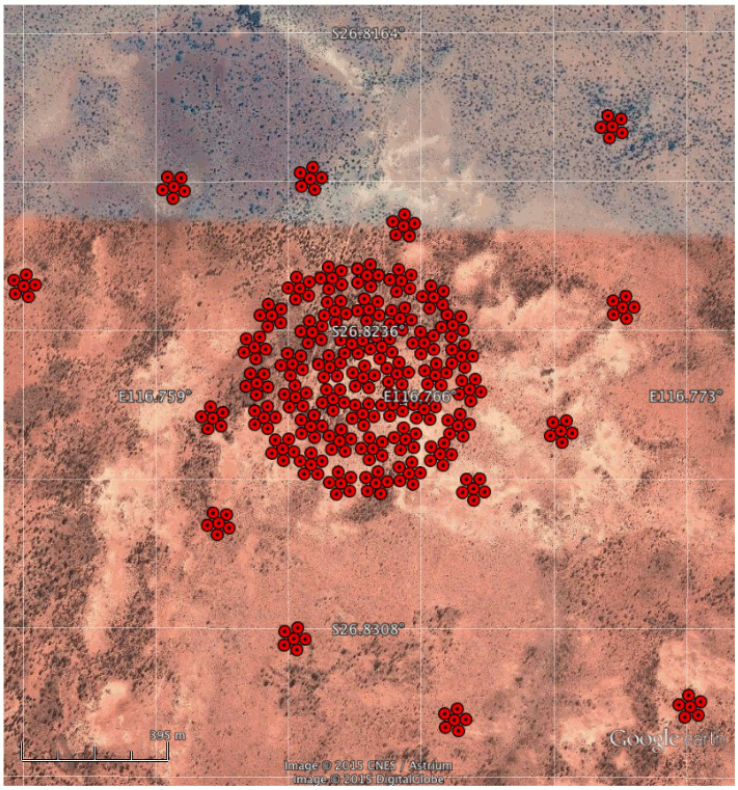

Figure 66: Layout of the SKA1-low core: a tightly packed system of randomised concentric rings, extending to a radius of about 350 m [100]. Each of the 40 red point represents one so-called superstation. The logarithmic spiral arms extending from 350 m to 6400 m are not used for cosmic ray detection.

number of events arriving with a given delay from the previous event. From this the number of arriving events which are lost due to “dead” time of the radio array can be calculated assuming that a certain time is needed for the read-out of the data. During this time, the buffers, storing the data for a certain time, are frozen during read-out of the data and the detector cannot register a new event. 3 s are assumed for the read out time [96]. This will lead to about a fraction of 5% of lost air shower events (see Fig. 68, left).
Also LOFAR uses an particle detector array for triggering on air showers [71]. There it could be shown that the radio frequency interference (RFI) level of the particle detectors is very low and does not effect the measurements of the antenna array. To reduce the RFI furthermore, the light detection in the particle detectors will be performed with SiPMs and optical fiber links will be used for read-out. An additional possibility is to bury the particle detectors to shield possible emission. This could possibly also improve the measurement quality of the particle detector array, as it would allow a dedicated measurement of muons.

7.1.1.2 Buffering of radio data

In contrast to observations in radio astronomy, extensive air showers arrive from random directions of the sky, without any a-priori knowledge of their arrival direction and time. Therefore, the signal of each antenna has to be buffered before reading-out until the trigger of the particle detector has been received ($\sim$ 10 ms). An installation of a suitable buffering capacity is crucial to enable SKA for air-shower detection. The buffers must stores the raw,

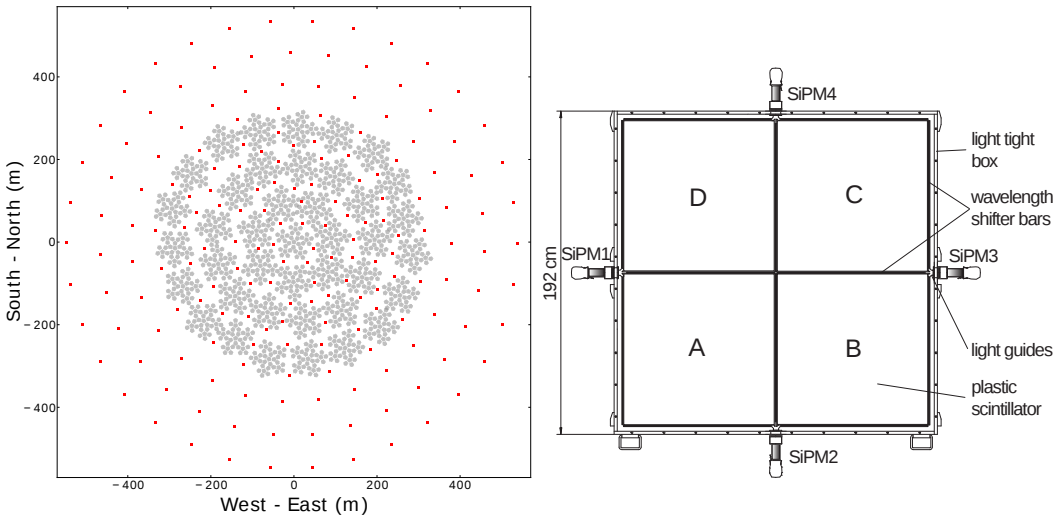

Figure 67: Left: Possible layout for a particle detector array, published in [98]. Possible positions for the particle detectors are marked by red dots. Right: Layout of the KASCADE scintillators [96].

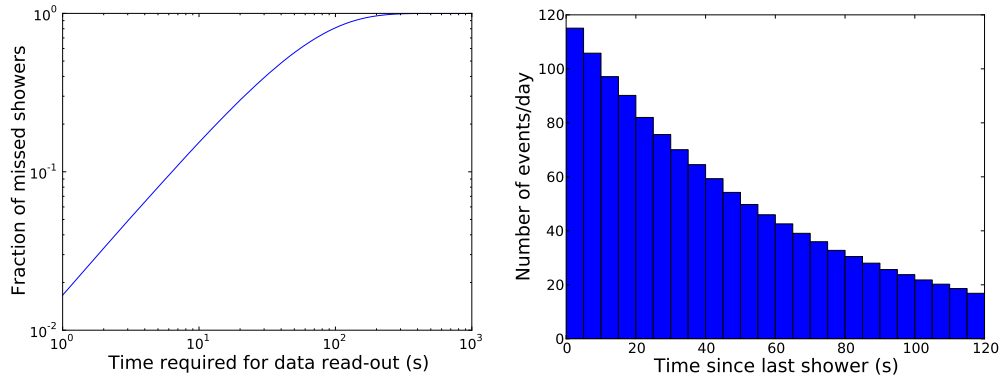

Figure 68: Left: Fraction of showers lost in dependency on the time which is needed for data read-out. Right: Number of events arriving with a given delay from the previous event. Both published in [96].

unprocessed signal for each polarisation for the individual antennas with a dynamic range of at least 8 bits, better 12 bits. Saturation could otherwise affect parts of the radio-emission footprint. This buffering should work completely independently and should run simultaneously without effecting any ongoing radio astronomy observations, aiming to get a near 100% duty cycle.

To reduce the amount of data that needs to be buffered and read out, one possible scenario is to only buffer and read out the data of every fourth antenna as long as these antennas are uniformly distributed. This means that every stations should contain the same fraction of antennas read-out.

7.2 MEASURING THE MASS COMPOSITION OF COSMIC RAYS IN THE TRANSITION REGION

The cosmic rays below 10^{16} eV are expected to come from a Galactic origin, while the highest energetic cosmic rays have to come from an Extragalactic origin, as already introduced in Chapter 2. But where exactly the transition between Galactic and Extragalactic origin takes places is still an open question. Accurate measurements of the cosmic ray mass composition are crucial to get a clean separation between protons and heavier nuclei in this energy region. This would provide the possibility to distinguish between models for sources and propagation of cosmic rays.

The main observable to study the mass of the primary particles initiating extensive air showers is the atmospheric depth X_{max} (in g/cm^2) at which an air shower reaches its maximum particle number. This represents how far the shower penetrates the Earth's atmosphere until it has evolved to its maximum particle number. This parameter is strongly correlated with the mass of the primary particle and can therefore be used to separate the elements of the incoming cosmic rays. Methods used for the identification of the particle mass by the atmospheric shower depth are based on statistics.

Due to a larger inelastic nucleus-air cross section and due to the simultaneous development of several subshowers, the first interaction of heavier nuclei with an atmospheric molecule takes places higher in the atmosphere than for light nuclei. In other words: on average, the development of an iron-induced shower starts earlier. Therefore it reaches the maximum number of particles earlier (lower atmospheric depth) than in the case of proton-induced showers of the same energy (higher atmospheric depth). Typically the difference in the depth for the shower maximum is about:
$\langle X_{\mathrm{max,p}} \rangle - \langle X_{\mathrm{max,Fe}} \rangle = 100\,\mathrm{g/cm^2}$ (see Fig. 69). At the moment the best reconstruction uncertainty for X_{max} is given by the fluorescence detection technique with $\sim 20\,\mathrm{g/cm^2}$ [36], as for example at the Pierre-Auger-Observatory with HEAT (High Elevation Auger Telescopes). Here, light is emitted by air molecules which were excited by shower particles. X_{max} is also measurable by optical Cherenkov light which is emitted by the shower particles. This is done for example by the Tunka experiment [101]. But both techniques require dark nights and have therefore just a duty cycle of about 15%. Particle detector arrays like KASCADE [3] or IceTop [5] measure the mass composition via the electron-muon ratio at ground level, which are produced as secondary particles in the air shower. The ratio depends on the mass of the primary particle, but also on the age of the shower. Therefore, the technique is susceptible to shower-to-shower-fluctuations. The results for the KASCADE-Grande experiment are shown in Fig. 70.

7.2.1 Measurements of the shower maximum via radio signals

Radio detection of air showers has a duty cycle of almost 100%. Like the fluorescence light, the radio emission from particle showers contains the information of the complete longitudinal shower development. Therefore it is possible to reconstruct the shower maximum

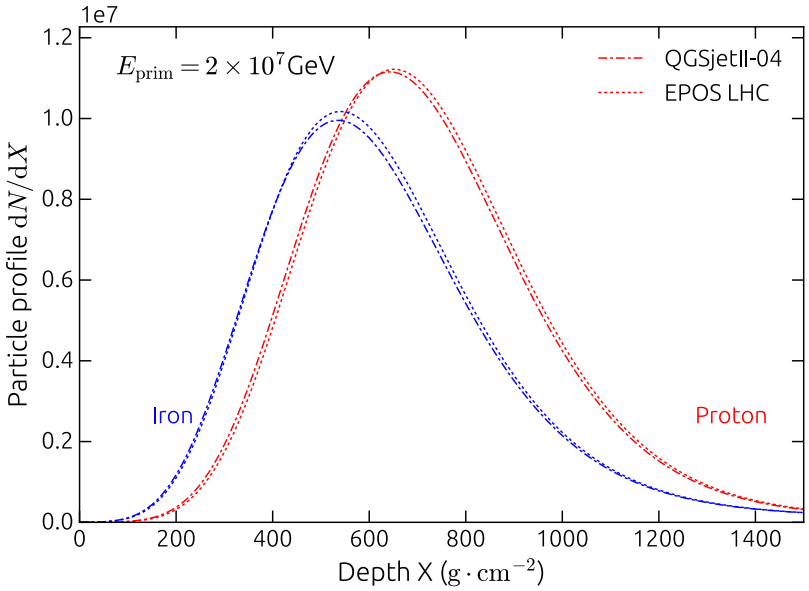

Figure 69: Average longitudinal shower profile: Simulated number of all particles in the shower in dependence on the atmospheric depth [102].

X_{max} from measured radio signals [66]. The feasibility was already shown by previous radio arrays such as LOPES, the Tunka-Rex experiment [103], LOFAR [73] and AERA [104]. Here, a reconstruction via the wavefront of the radio signal as well as as via the slope of the lateral distribution was performed (compare to Fig. 6 in Chapter 2.2).
For the first approach, the reconstruction via the wavefront of the radio emission, it was found that the distance from the radio array to the shower maximum determines the deviation in time of the arrival of the signal in comparison to a plane wavefront [105]. It was observed that the closer the shower maximum was to the radio array, the steeper the radio wavefront, and the steeper the lateral distribution of the radio signal. A simulation study predicted a reconstruction uncertainty of 30 g/cm^2 for the LOPES experiment if the measurements were performed under ideal conditions. Experimentally, LOPES could achieve an uncertainty of 140 g/cm^2.

In the second method (LDF method), the dependency of the slope of the lateral distribution on the shower development was exploited [66]. Input from simulation studies performed with CoREAS simulations was used as input to reconstruct measured events. Simulations predicted a precision of the reconstructed X_{max} of about 50 g/cm^2. For measurements the LOPES experiment finally reached a precision of 95 g/cm^2, even having strong human-made noise at the LOPES site. For the measurements with AERA and Tunka-Rex a precision of the X_{max} reconstruction of $\sim$ 40 g/cm^2 could be achieved [104, 103].

The most precise measurements of the mass composition in the energy region of $10^{17} - 10^{17.5}$ eV were performed by LOFAR.

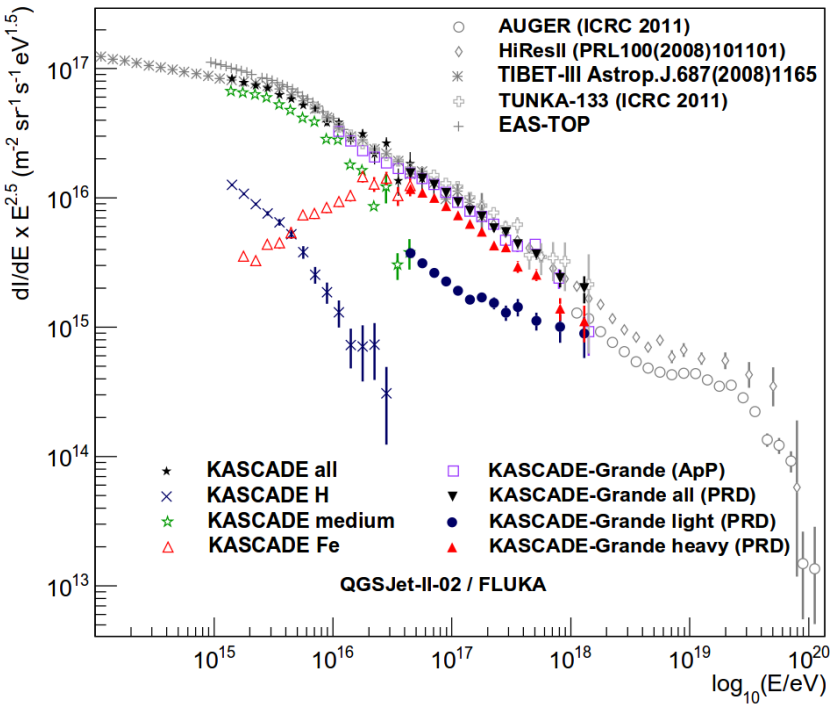

Figure 70: The all-particle energy spectrum and spectra of individual mass groups obtained with KASCADE and KASCADE-Grande [63].

7.2.2 From LOFAR to SKA

LOFAR (see Chapter 3.2.4) acts as one of the pathfinders of SKA for low-frequency radio astronomy and was enabled to perform cosmic ray detection. The impressive mean X_{max} resolution of about 16 g/cm^2 [73] obtained for the reconstruction of the shower maximum in the energy range of $10^{17} - 10^{17.5}$ eV gives an indication of the potential for cosmic ray detection with the future SKA1-low. For the best air shower events a resolution of better than 10 g/cm^2 could be reached.

At LOFAR, the reconstruction of the shower maximum is based on the comparison of measured data with simulated results of a set of 50 proton- and 20 iron-induced air showers [73], produced with CORSIKA (COsmic Ray SImulations for KAscade) [55] and its plug-in for the radio emission calculation CoREAS [56]. An example comparison of a simulated with a measured radio footprint is shown in Fig. 71 (left). In the reconstruction method used by LOFAR, the individual simulations are compared with the measurements to find the simulation with its specific parameters, e.g. X_{max}, whose results fit to the data best (compare to Fig. 71, right). In this comparison, the measurements of the radio antenna array as well as the measurements of the particle detector array are used for the shower depth reconstruction.

For measuring the shower depth of individual air shower events with SKA1-low and just using the information of the radio signal measurements, it is assumed that all “contained ” events will be “good” events due to the highly detailed sampling of the radio emission footprint. Therefore, it is expected that SKA1-low will yield a mean uncertainty of 10 g/cm^2

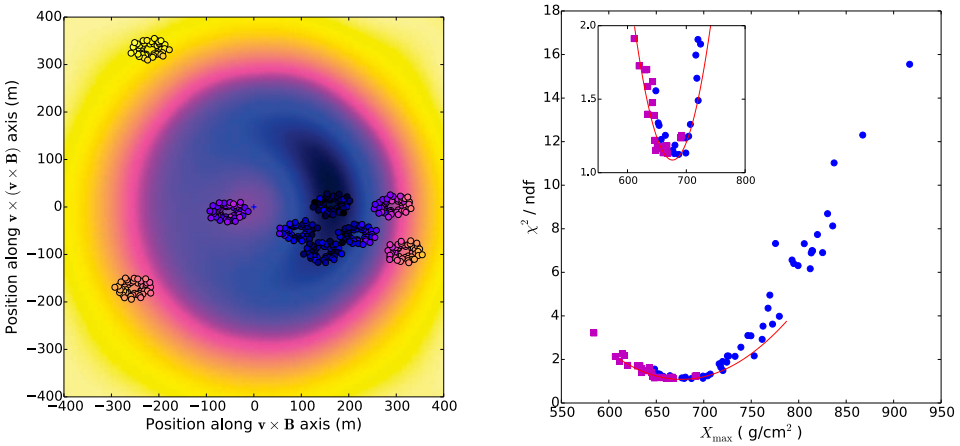

Figure 71: Left: Comparison of measured data (circles) to a simulated radio footprint (background). Right: Distribution of the results from χ^2 fits in the comparison of an measured event to a set of corresponding simulations (purple: proton as primary, blue: iron as primary). Both taken from [74].

or better for the X_{max} measurement for each measured cosmic-ray shower, leading to the world's most precise mass determination. The test of this hypothesis will be performed in detail in the following sections.

7.2.2.1 Increased antenna density and homogeneity

A comparison of the LOFAR array layout and the SKA1-low layout is illustrated in Fig. 72, demonstrating one of the significant differences between LOFAR and SKA1-low. The part of LOFAR which is used for cosmic ray detection consists of an inhomogeneous array with significant gaps in-between the antenna stations, whereas SKA1-low is a very densely packed and very homogeneously distributed antenna array leading to an increased measurement precision of the radio emission footprint on the ground. Thus, a detailed measurement of the characteristics in the footprint, such as the Cherenkov cone, is possible if most of the footprint is covered by SKA1-low while for LOFAR this is only feasible for the "best" events where the shower core hits the superterp's stations.

7.2.2.2 Increased frequency coverage

In addition, the LOFAR and the SKA1-low array differ in the frequency range they cover. While LOFAR measures in the frequency band of $30-80\,\mathrm{MHz}$ containing a large part of the radio energy, SKA1-low covers frequencies from $50-350\,\mathrm{MHz}$. Here, the reconstruction of the shower maximum could profit from the fact that the structure of the Cherenkov cone becomes more pronounced for higher frequencies. Additionally, it has to be investigated whether additional parameters characterising the footprint can be found which could be added to the existing method for X_{max} reconstruction.

The impact of the higher frequencies in combination with a broader bandwidth is studied in Section 7.4.2 in more detail.

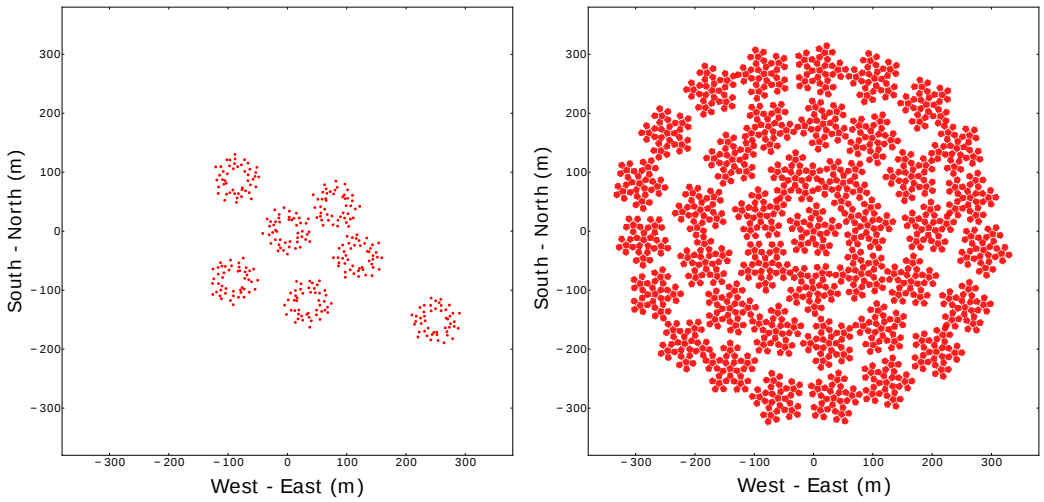

Figure 72: Comparison of the LOFAR antenna array (left) and the SKA1-low array layout (right).

7.2.2.3 Increased event statistics

While the results on the mean uncertainty of the X_{max} reconstruction by LOFAR are impressive, the results on the mass composition of the cosmic ray flux are limited by the event statistic. On the one hand, the fiducial area for air-shower detection is limited to less than 0.1 km^2 since only the LOFAR core is used. On the other hand, the cosmic-ray detection can not be performed 100% of the time mainly due to technical and organisational conflicts with the radio astronomy observations arising since the mode of cosmic ray detection was not planned as a feature initially.
The SKA1-low array will have a fiducial area of about 1 km^2 and aim for 100% duty cycle which will increase the event statistic by a factor of 100 compared to LOFAR. To achieve a duty-cycle of 100%, the cosmic-ray detection mode should run simultaneously without affecting any radio astronomy observation.
Approximately 10,000 air showers per year with an energy above 10^{17} eV are expected to be measured by SKA1-low.

7.3 INITIAL SIMULATION STUDIES

The method used for the reconstruction of the shower depth was developed in the context of cosmic ray measurements with the dense LOFAR core [74], introduced in Sec. 3.2.4. It is based on fitting the simulated two-dimensional radio signal profiles to the measured data. This methods requires a precise simulation of the radio emission. LOFAR showed that the simulations of an air-shower radio signal done with CoREAS [56] are in excellent agreement with the data.
For the following study on the uncertainty of the reconstruction of the shower maximum, simulations set of air-showers induced by protons and iron nuclei of the same primary parameters are done with CORSIKA [55] (v7.4) and its plug-in CoREAS with OGSJETII-04 as the hadronic interaction model [19] and FLUKA for low energies [106]. The radio signal is sampled with 800 MHz due to the given SKA1-low design parameters [100]. As the thinning level a value of $5 \cdot 10^{-7}$ was chosen.

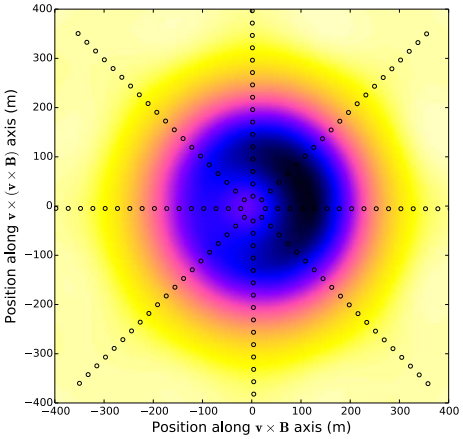

Figure 73: Two-dimensional profile of the received power integrated over a 55 ns window [74]. This shows a simulation result of a proton shower with a primary energy of $2.3 \cdot 10^{17}$ eV and a zenith angle of 49°, having an $X_{\max}$ of 794 g/cm^2. The black circles indicate the antenna positions for which the electric field was calculated. The background represents the interpolation of the total power in-between these positions, normalised to its maximum value of the simulated power.

The radio emission from the air shower due to the geomagnetic and the charge excess effects is polarised differently (see Chapter 3). The geomagnetic radiation is polarised linearly along the $\vec{v} \times \vec{B}$ direction with $\vec{v}$ as the velocity of the shower front and $\vec{B}$ describing the Earth's magnetic field at a certain place on the Earth while the radiation due to the charge excess in the shower is linearly polarised around the shower axis. These two contributions to the total radio signal can add constructively or destructively, depending on the observer's position. For a proper understanding, Fig. 73 shows the received total power in the coordinate system of the shower plane as the final radiation profile. The axes are chosen along $\vec{v} \times \vec{B}$ and $\vec{v} \times (\vec{v} \times \vec{B})$. In the positive $\vec{v} \times \vec{B}$ direction the two emission components interfere constructively while they interfere destructively in the negative $\vec{v} \times \vec{B}$ direction. Along the $\vec{v} \times (\vec{v} \times \vec{B})$ direction the two components are polarised orthogonally. This results in a no-rotationally symmetric interference pattern which typically has a bean-like shape for the LOFAR frequencies from $30 - 80$ MHz.

7.3.1 Reconstruction method of the shower depth for SKA1-low

As observer positions for which the radio signals were calculated 160 antenna positions in the shower plane defined by $\vec{v} \times \vec{B}$ and $\vec{v} \times (\vec{v} \times \vec{B})$ were chosen. In Fig. 74 (left) the positions are indicated by black circles. They form a so-called star-shape pattern having 8 arms, 4 of which are positioned along the $\vec{v} \times \vec{B}$ and $\vec{v} \times (\vec{v} \times \vec{B})$ axis, respectively. Each arm consists of 20 antennas with a distance of 25 m.
This setup ensures the possibility of a robust interpolation between the simulated antenna positions in the shower plane and conserves the asymmetry of the total power received at a particular location arising from the interference of the two radio emission components.
For each antenna position the East-West and the North-South components of the filtered electric field is filtered to the SKA1-low frequency band of $50 - 350$ MHz. No antenna model

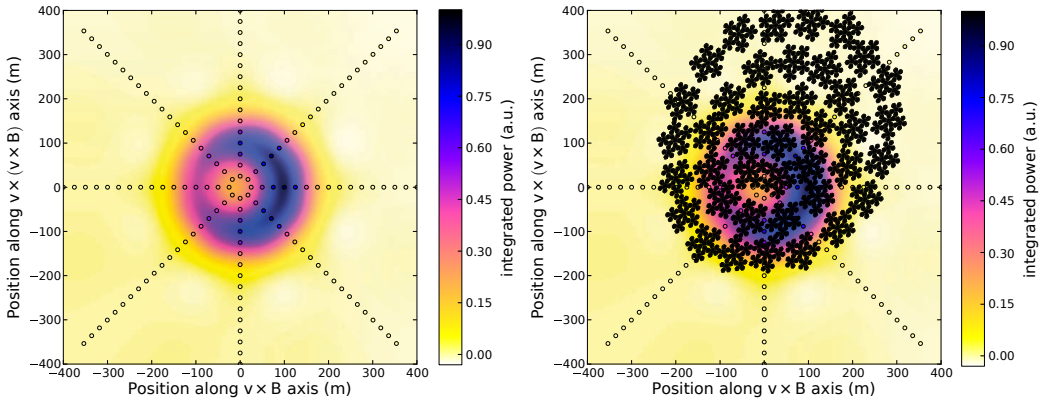

Figure 74: The plots shows the total integrated power in the shower plane defined by the axes $\vec{v} \times \vec{B}$ and $\vec{v} \times (\vec{v} \times \vec{B})$, normalised to the maximum power. Left: Total integrated power at the simulated antenna positions (circles) and the interpolated radio footprint in the shower plane as colored background for a proton-induced air shower with a primary energy of $E = 10^{17}$ eV and a zenith angle of 36.84°, filtered to a frequency band of $50 - 350$ MHz and normalised to the maximum power. Right: The SKA1-low antenna positions rotated into the shower plane. At each antenna position, a value for the total received power is interpolated. Both published in [99].

was included. The resulting signal for both polarisations are then summed up quadratically. Afterwards, the time-integral of the total received power over the total time traces was computed for each antenna in the star-shape pattern. The footprint of the radio signal with its asymmetry due to the interference of the Askaryan and the geomagnetic effect can be reconstructed by interpolation between the rays of the star-shape pattern, as indicated as background in Fig. 74 (right).

For the estimation of the power received by the SKA1-low antennas, the complete SKA antenna array is rotated into the shower-plane frame. Finally, each antenna is assigned a total power corresponding to the interpolated power at this position (see Fig. 75, left). These steps are performed for each single simulation in a set which consists in total of 50 proton-induced and 20 iron-induced air shower simulations. Displayed in Fig. 75 (right), the zoom into the radio footprint measured by SKA1-low indicates with which impressive precision the radio signal of an air shower can be sampled by the homogeneous antenna array.

Finally, each simulation acts once as “fake” data. This means that for this simulation random noise is added to the interpolated total power of each antenna following a Gaussian distribution. This noise is defined as a contribution of 5% of the total power of each antenna as uncertainty on the antenna calibration and 1% of the maximum total power received by an antenna in the whole array as an approximation for Galactic noise. This is just a first approximation to estimate the impact of the noise since with this definition the noise scales with the energy of the primary particle in the reconstruction of the shower depth. More realistic assumptions, including a frequency dependency, have to be implemented in future calculations. The remaining simulations of the set are then compared to this “fake” data on the basis of a χ^2 fit:

$$\chi^2 = \sum_{antennas} \left(\frac{P_{fake} - P_{sim}}{\sigma_{fake}} \right)^2 . \tag{31}$$

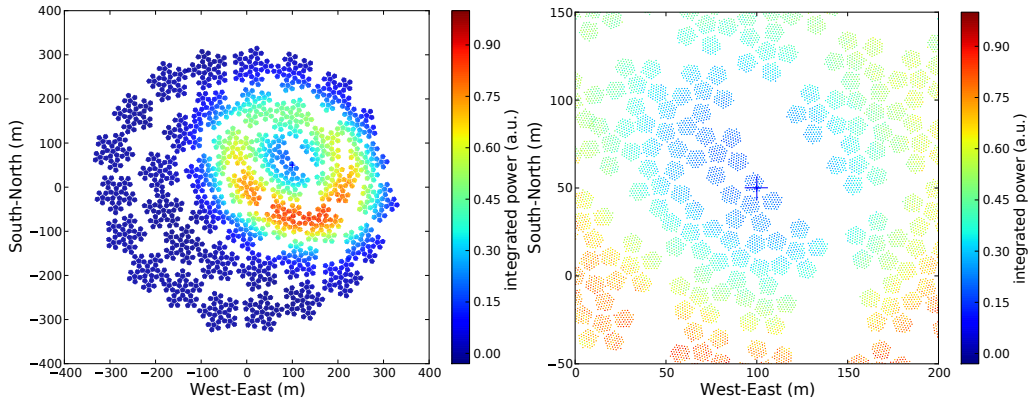

Figure 75: The plots represent the over time integrated power on the ground, normalised to the maximum power, with North pointing upwards. The different color scheme to the shower plane plots is chosen to underline to change of the coordinate system. Left: The example radio footprint on ground as detected by the SKA1-low array, published in [99]. Right: A zoom into the radio footprint measured by the SKA1-low antenna array, published in [98]. The blue cross marks where the air shower core hits the ground.

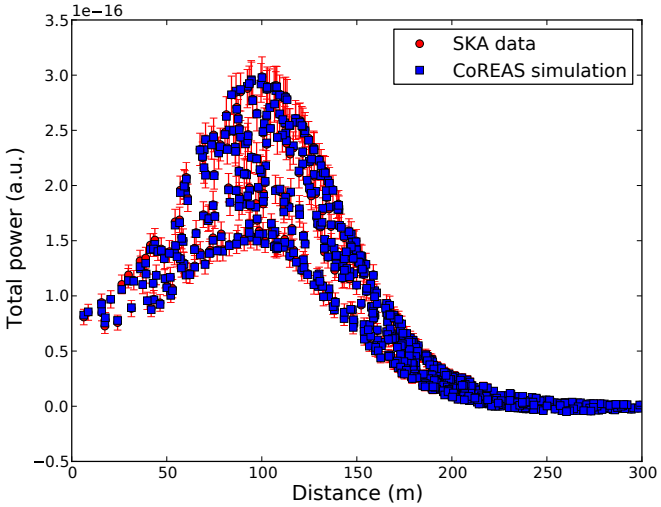

Figure 76: Comparison of the lateral distribution of the radio signal on ground for the “SKA data” and the CoREAS simulation which describes the data best. Here, the total power received by every 64th antenna of the SKA1-low array is shown for a easier assignment of the “measured” and simulated data points.

P_{fake} is the total power of a single antenna in the fake “SKA data” set, with σ_{fake} denoting the assumed uncertainty due to noise, and P_{sim} the power interpolated from the simulations for the same position.
In this comparison, every 8th antenna in a radius of 300 m around the point at which the air shower core hits the ground is included, guaranteeing that the antenna positions are homogeneously distributed over the antenna array. This step can be interpreted as reading out every 8th antenna after an air shower measurement.

For every comparison of the “fake” data to one of the remaining simulations a χ^2 value is returned which can be connected to a corresponding $X_{\text{max, MC}}$, which will be called X_{sim} in the following, known from the simulation. The core position of the air shower is fixed to the Monte-Carlo truth for all simulations. In future studies, the core position should also be

included as a fit parameter. In Fig. 76 the comparison of the power received by the single antennas (P_{fake}) to the simulated signal (P_{sim}) of the best-fitting simulation is illustrated by plotting the lateral distribution of the radio signal on ground. The error bars are determined by the assumed noise for the single antennas. The calculation of the value for the shower maximum is performed by the simulation program CORSIKA. The Gaisser-Hillas formula [107], which nicely describes the longitudinal evolution of an air shower in dependence on the shower depth, is fit to the longitudinal particle distribution read-out in 5 g/cm^2 steps from the air shower simulation.

As shown in Fig. 77 (left, top), this leads to a distribution to which a parabolic function can be fitted. The X_{max} value for which the parabola has its minimum then returns the "reconstructed" shower depth X_{reco} for this "fake" air shower event. Here, all simulations which lead to an $\chi^2/\text{ndf} \leqslant 5$ are included in the fit. As the "real" shower maximum for this event the result of the Gaisser-Hillas fit to the longitudinal particle distribution is chosen.

The absolute difference between X_{reco} and each "real" shower maximum's depth $X_{\text{max,real}}$ of the simulated shower event, which will be called X_{real} in the following, is filled into a histogram (see Fig. 77, top right). As the 1σ uncertainty, marked by a vertical line, the value of $|X_{\text{reco}} - X_{\text{real}}|$ which contains 68% of entries is defined. It represents the statistical uncertainty of the shower reconstruction by the method when all simulations in a set act as "fake" event once.
In Fig. 77 (bottom) it is shown that the distribution of the difference between X_{reco} and X_{real} is clustered around 0.

7.4 FIRST RESULTS FOR THE RECONSTRUCTION OF THE SHOWER DEPTH

For this study, the position of the core where the air shower hits the ground, was chosen at 100 m east and 50 m north of the center position of SKA1-low. This guaranteed to study a general example of a in SKA1-low 'contained' event as well as to avoid the effects of the radial symmetry of SKA1-low.

Fig. 77 (top, right) shows the resulting mean reconstruction uncertainty for the simulation set of 50 proton and 20 iron showers with a primary energy of $E = 10^{17}$ eV, an azimuth angle of 225° and a zenith angle of 36.84°. For these parameters the reconstruction method described here achieves an uncertainty of 6.8 g/cm^2.

Obviously, the uncertainty of the reconstruction can depend on shower parameters such as the primary energy and the arrival direction which will be studied in the next sections.

7.4.1 The influence of the number of antennas read out

As already mentioned, in this simulation study only every 8th antenna of the SKA1-low array is included in the comparison to simulations, which can be interpreted as a reduced number of antennas read out for an air-shower event. To prove that this has no significant impact on the results of the reconstruction uncertainty of the depth of the shower maximum,

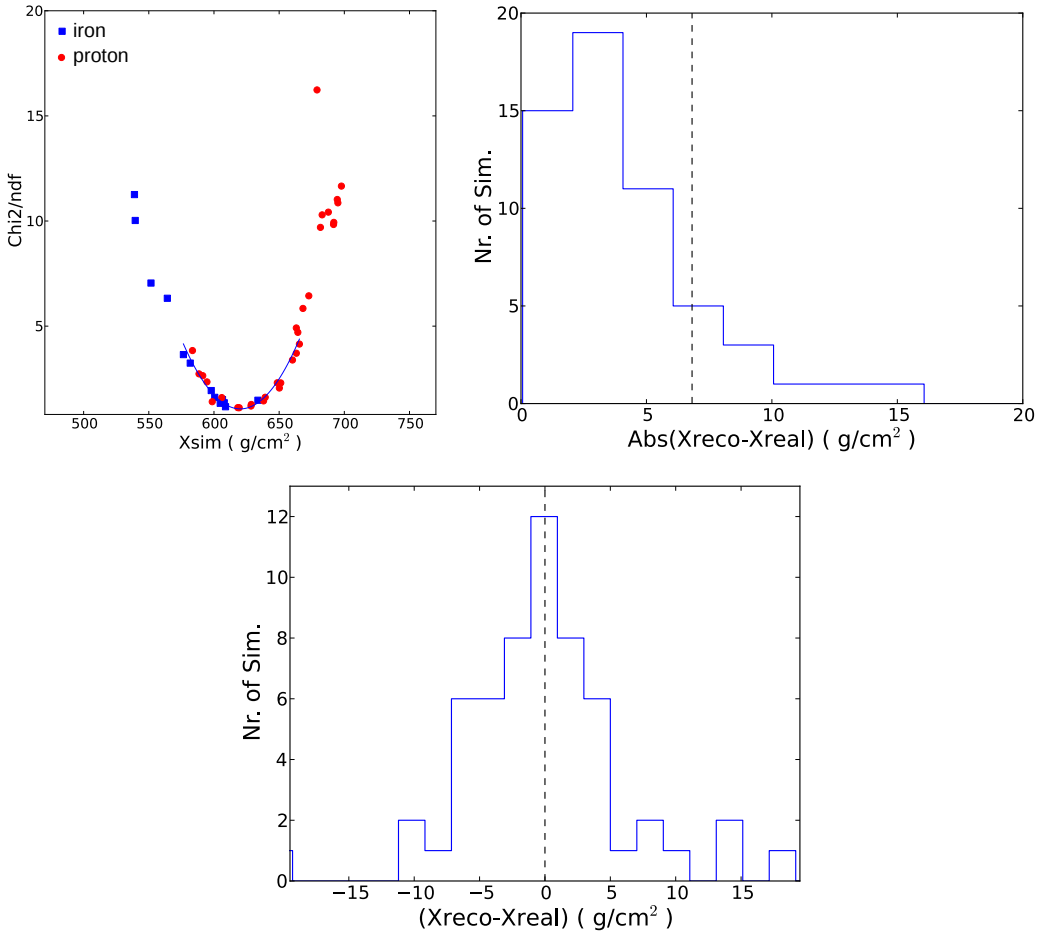

Figure 77: Top: Left: An example χ^2 distribution for the comparison of one "fake" event for the SKA1-low array layout for an air shower event with the remaining simulations of a set with an primary of $E = 10^{17}$ eV and a zenith angle of 36.84°. Right: Histogram for the absolute differences of the reconstructed and the "real" shower depth for the simulation set for a primary energy of $E = 10^{17}$ eV and a zenith angle of 36.84°. Some outliers beyond a difference 20 g/cm^2 are not shown but included in the calculations of the reconstruction uncertainty. Bottom: Distribution of the differences between X_{reco} and X_{real} for the whole simulation set.

the procedure was also applied including all SKA1-low antennas for the same simulation set of 50 proton and 20 iron-induced air showers. The results are shown in Fig. 78.
Even if the distribution in the histogram is changed, since the background noise is randomly added to the simulated signal, the resulting uncertainty for the depth of the shower maximum is 6.8 g/cm^2. This shows that reducing the number of antennas which are included in the reconstruction to every 8th antenna is valid and does not influence the result.
However, an effect of a further thinning of the antenna array has to be studied. Fig. 79 shows the result for the reconstruction uncertainty if just every 16th antenna of the array is included. In the example, this further thinning leads to an uncertainty of 7.2 g/cm^2 which is slightly worse than in the former result. For the example of reading out only every 32th antenna as shown in Fig. 80, the reconstruction uncertainty increases to a value of 7.4 g/cm^2. Reducing of the numbers of antennas even more would lead to a much worse precision in the reconstruction.

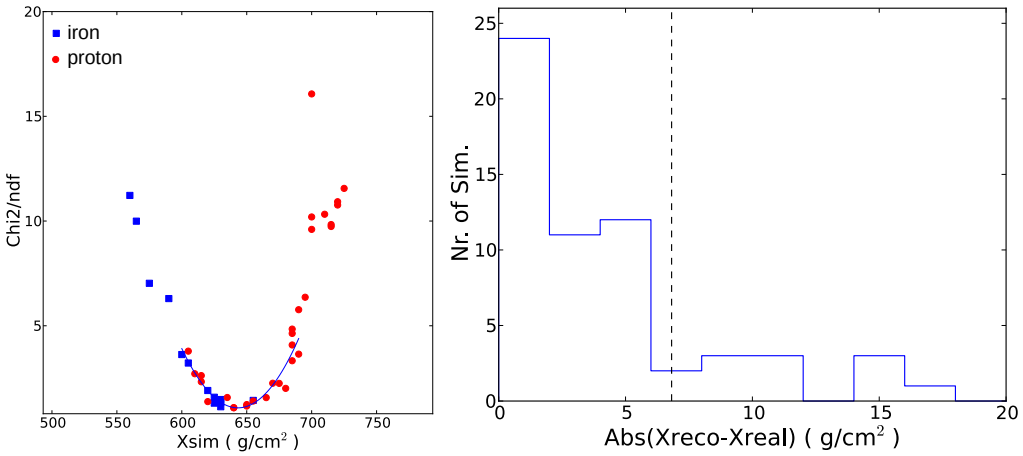

Figure 78: Left: χ^2 distribution for the same example event as in Fig. 77, just including all antennas of SKA1-low in the reconstruction. Right: Histogram for the absolute differences of the reconstructed and the "real" shower depth for the air-shower detection with the SKA1-low array, including all antennas in the reconstruction, leading to a reconstruction uncertainty of 6.8 g/cm^2.

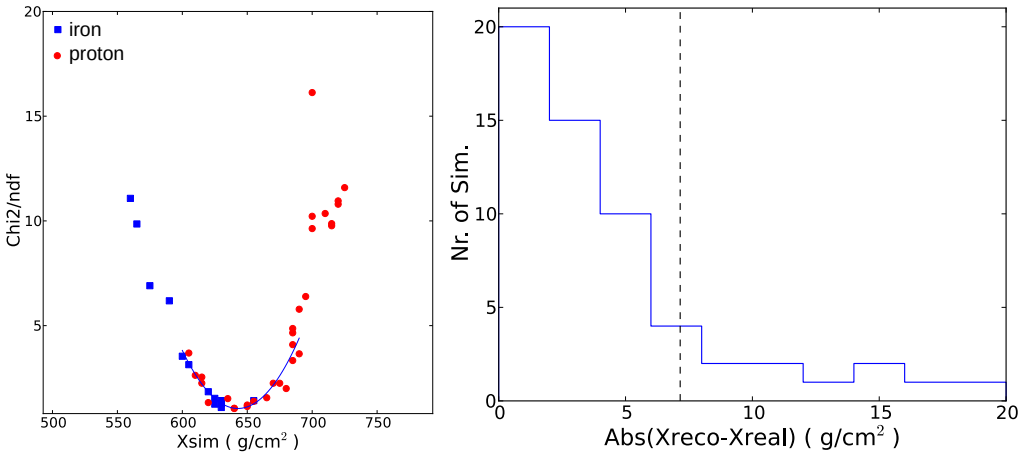

Figure 79: Left: χ^2 distribution for the same example event as in Fig. 77, including every 16th antenna of SKA1-low in the reconstruction. Right: Histogram for the absolute differences of the reconstructed and the "real" shower depth for the air-shower detection with the SKA1-low array, including every 16th antenna in the reconstruction, leading to a reconstruction uncertainty of 7.2 g/cm^2. Some outliers beyond a difference 20 g/cm^2 are not shown but included in the calculations of the reconstruction uncertainty.

A thinning of the antenna array, meaning just reading out a subset of the antennas, leads to a slightly worse reconstruction uncertainty, but does not affect the precision on the shower maximum reconstruction significantly as long as the read-out are homogeneously distributed over the radio footprint. However, the study of the impact of the number of the read-out antennas is closely connected to and therefore limited by the number of simulated antenna positions, whose impact is explored in Sec. 7.4.6. Not to read-out all antennas can therefore be used to reduce the data which have to be transferred and analysed for the individual detected air-shower events.

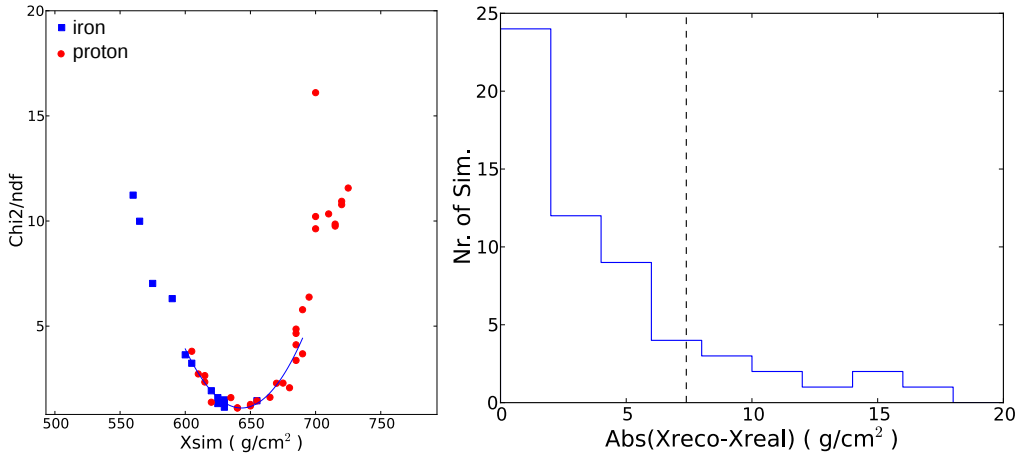

Figure 80: Left: χ^2 distribution for the same example event as in Fig. 77, including every 32th antenna of SKA1-low in the reconstruction. Right: Histogram for the absolute differences of the reconstructed and the "real" shower depth for the air-shower detection with the SKA1-low array, including every 32th antenna in the reconstruction, leading to a reconstruction uncertainty of 7.4 g/cm^2. Some outliers beyond a difference 20 g/cm^2 are not shown but included in the calculations of the reconstruction uncertainty.

In the following the reconstruction of the air-shower events is performed including every 8th SKA1-low antenna. Whether the results of the reconstruction uncertainty for certain parameters as for another primary energy or another arrival direction can be reduced by including more antennas in the fitting procedure has to be explored in a future study.

7.4.2 Impact of the frequency band

One of the clear differences between SKA1-low and LOFAR is the frequency band. In the LOFAR analysis the frequency band is limited to $30-80$ MHz. In this frequency range, a bean-like structure is visible in the radio footprint instead of a clear Cherenkov ring as for the higher frequencies as visible in Fig. 81. The figure shows the radio footprint in the shower plane filtered to $30-80$ MHz (left) as well as filtered to $50-350$ MHz (right). It is observable that the received integrated power over time in the frequency band of $50-350$ MHz is higher than the one in $30-80$ MHz. Even if the galactic noise level for higher frequencies is much lower which could make the separation from noise easier. For a direct comparison, the footprint on ground detected by SKA1-low for the same event as in Fig. 74 is displayed in Fig. 82 for $30-80$ MHz and $50-350$ MHz.
For the same set, containing the same 50 proton- and 20 iron-induced showers with a primary energy of $E = 10^{17}$ eV, an azimuth angle of 225° and a zenith angle of 36.84°, the method returns a larger uncertainty of 16.5 g/cm^2 when filtering the signal to $30-80$ MHz, as illustrated in Fig. 83 (right).
In addition to a higher received power in the SKA1-low frequency band, in comparison to LOFAR SKA1-low seems to profit from the prominent Cherenkov cone structures in applying the introduced method for the reconstruction of the shower depth. The comparison of the fake data set to the simulation for the $50-350$ MHz returns a more distinct χ^2 distribution than the one for the comparison in the frequency range of $30-80$ MHz (compare Fig. 83 (right) and Fig. 77 (right)). The parabola is narrower so that the minimum of the χ^2

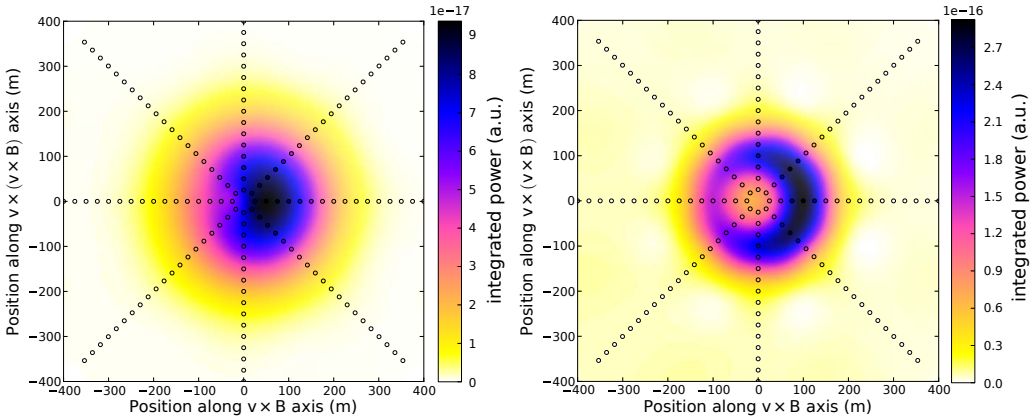

Figure 81: Total integrated power at the simulated antenna positions (circles) and the interpolated radio footprint in the shower plane for a proton-induced air shower with a primary energy of $E = 10^{17}$ eV and a zenith angle of 36.84°, filtered to a frequency band of $30 - 80$ MHz (left) and of $50 - 350$ MHz (right).

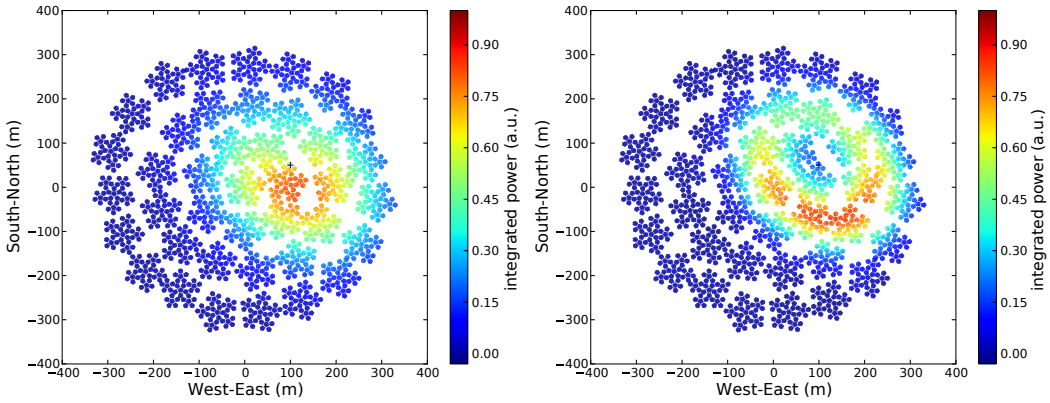

Figure 82: An example radio footprint on ground for an proton-induced air shower of a primary energy of $E = 10^{17}$ eV as detected by the SKA1-low array, filtered to a frequency band of footprint $30 - 80$ MHz (left) and $50 - 350$ MHz (right), respectively, and normalised to the maximum power.

distribution is more precisely defined.

To study the possible improvement in the measurements of the depth of the shower maximum performed with SKA1-low, beside the typical frequency range of $30 - 80$ MHz also the LOFAR array layout is tested in the reconstruction. Displayed in Fig. 84, the same event as in Fig. 81 is now sampled with the LOFAR radio antenna array, filtered to frequencies from $30 - 80$ MHz. The position where the core hits the ground is chosen so that it is comparable to an average measured LOFAR air shower (compare to example events in [74]). Here, the radio footprint would not be fully contained in the LOFAR array. Therefore, the footprint is not so precisely sampled as in the case of SKA1-low. For the complete simulation set, this LOFAR-like setup leads to an uncertainty of 24.5 g/cm^2 for the reconstruction of the shower maximum by the method (see Fig. 85, right).

Fig. 85 (left) shows an example χ^2 distribution for this set. It is observable that now the comparison of almost all simulations would lead to a χ^2/ndf of $\leqslant 5$ to be included in the parabola fit. This means that the measured power distributions on ground look quite similar

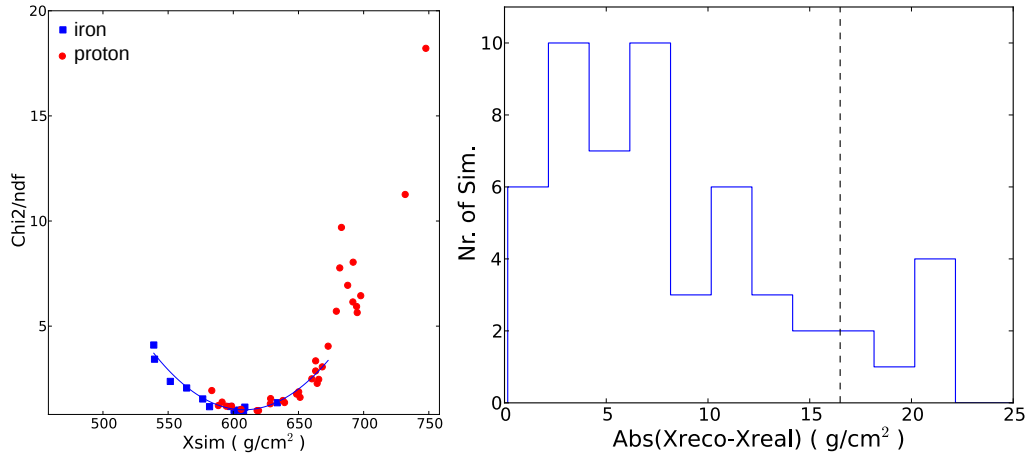

Figure 83: Left: The χ^2 distribution for the SKA1-low array layout for a frequency band of $30-80$ MHz. Right: Histogram for the absolute differences of the reconstructed and the "real" shower depth for the air-shower detection with the SKA1-low array being sensitive to $30-80$ MHz, leading to a reconstruction uncertainty of 16.5 g/cm^2.

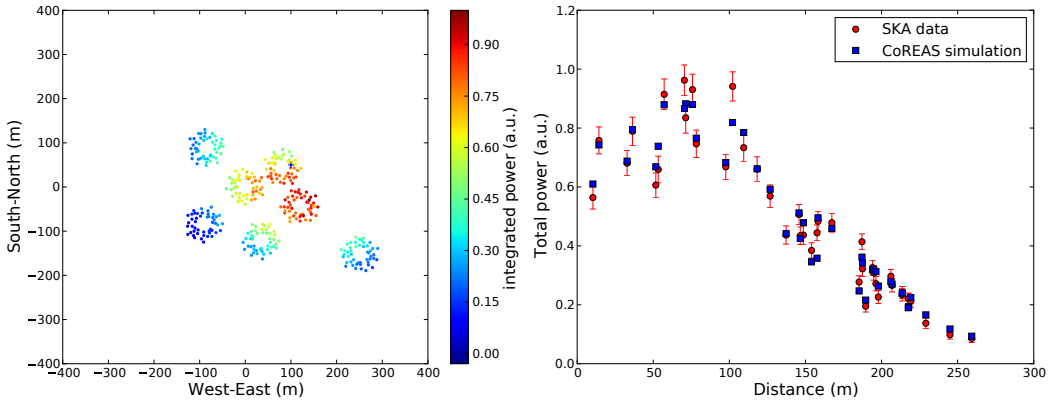

Figure 84: Left: A radio footprint on ground as detected by a LOFAR-like array, filtered to a frequency band of $30-80$ MHz and normalised to the maximum power. Right: The corresponding lateral distribution of the "measured" power and the simulated power of the simulation which fits the data best.

for all 70 simulations in the set and do not differ extremely in dependence of the shower maximum as in the case for the frequency band of $50-350$ MHz.

Besides the fact that for SKA1-low frequencies band at higher frequencies the received total power is higher than for the LOFAR frequency band, for the reconstruction of the depth of shower maximum of individual air shower events SKA1-low can profit especially from the upcoming Cherenkov cone structure in the frequency band of $50-350$ MHz as well as, in comparison to the LOFAR layout, it will profit from from the larger area and also from the more homogeneous sampling of the footprint with a huge number of antennas.

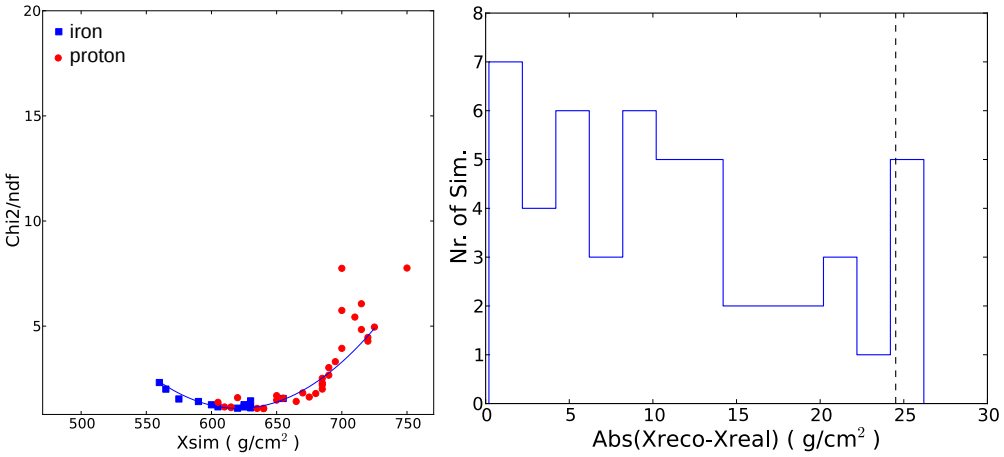

Figure 85: Left: The χ^2 distribution for the LOFAR array layout for a frequency band of $30-80$ MHz. Right: Histogram for the absolute differences of the reconstructed and the "real" shower depth for air-shower detection with the LOFAR array being sensitive to $30-80$ MHz, leading to a reconstruction uncertainty of 24.5 g/cm^2.

7.4.3 Dependence on the primary energy

For a fixed zenith angle of 36.84°, simulation sets for different primary energies were prepared, each consisting of 50 proton- and 20 iron-induced air showers. The results of the reconstruction of the depth of the shower maximum indicate that the reconstruction uncertainty depends on the primary energy, even if the noise (unrealistically) scales with the primary energy. In other words the signal-to-noise ratio does not increase with higher primary energy, in this study the ratio does not change.

Fig. 86 and Fig. 87 show the power distribution for one proton event in the shower plane as well as sampled with the SKA1-low array on ground for a primary energy of $E = 10^{16}$ eV and $E = 10^{18}$ eV, respectively, which can be directly compared to the Figures 74 and 75. It is observable that for the low energetic primaries the Cherenkov ring has a larger radius than for higher energies. This can be explained geometrically: following the Heitler model (see Chapter 2.1.1), more generations of secondary particles can be produced in the air shower induced by a primary with a higher primary energy. Therefore, for air showers induced by lower energetic primaries the source of radiation is in average more far away from ground than for air shower induced by higher energetic primaries. In addition, one can also notice that the power of the radio signal increases with rising energy of the primary particle emphasizing the narrow structure of the Cherenkov ring.

The resulting uncertainties for the reconstruction of the depth of the shower maximum for different primary energies, listed in Tab. 1, are derived from the corresponding histograms containing the uncertainty for the single events (see Fig. 88).
The tendency of a decreasing reconstruction uncertainty with rising primary energy becomes evident. This is not an effect of the rising signal-to-noise ratio since in this study the included noise scales with the energy of the primary particle. This could be explained by a possible better resolution of structures at the Cherenkov cone since for higher primary energies the shower contains more generations of secondary particles and therefore the

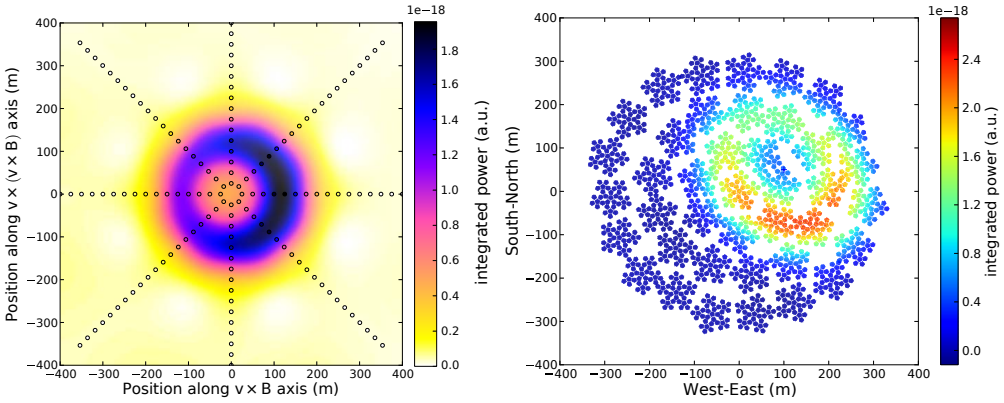

Figure 86: Left: An example simulated footprint of the radio signal in the shower plane, for a proton-induced air shower with a primary energy of $E = 10^{16}$ eV, filtered to the frequency band of $50 - 350$ MHz. Right: The corresponding simulated radio emission footprint on ground as detected by the SKA1-low array.

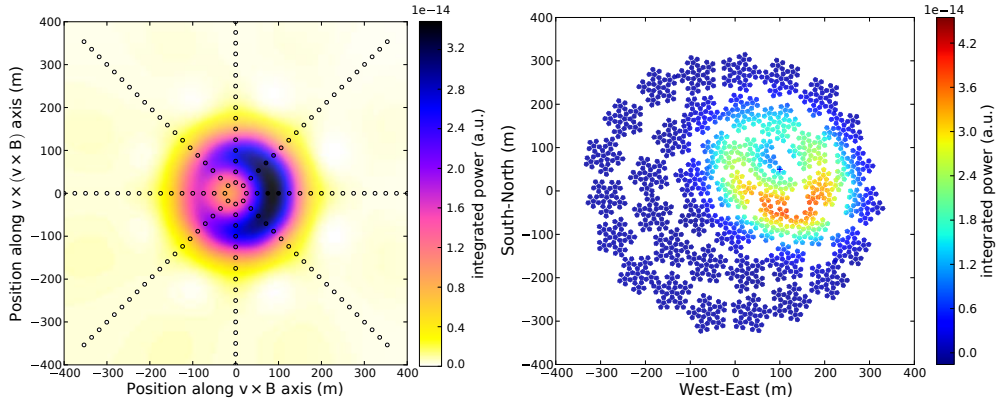

Figure 87: Left: An example simulated footprint of the radio signal in the shower plane, for a proton-induced air shower with a primary energy of $E = 10^{18}$ eV, filtered to the frequency band of $50 - 350$ MHz. Right: The corresponding simulated radio emission footprint on ground as detected by the SKA1-low array.

Table 1: Summary of the uncertainties by the method for the reconstruction of the depth of the shower maximum in dependence on the energy of the primary particle with a zenith angle of 36.84°.

energy	uncertainty
$E = 10^{16}$ eV	9.8 g/cm^2
$E = 10^{16.5}$ eV	8.3 g/cm^2
$E = 10^{17}$ eV	6.8 g/cm^2
$E = 10^{17.5}$ eV	4.5 g/cm^2
$E = 10^{18}$ eV	3.5 g/cm^2

source of the radio emission is closer to the ground. The reconstruction method profits from this since in general the structures of the footprints of the “fake” and the simulated data get compared. Consequently, the more prominent the structures in the two dimensional profiles are, the better the simulation which fits best can be identified.

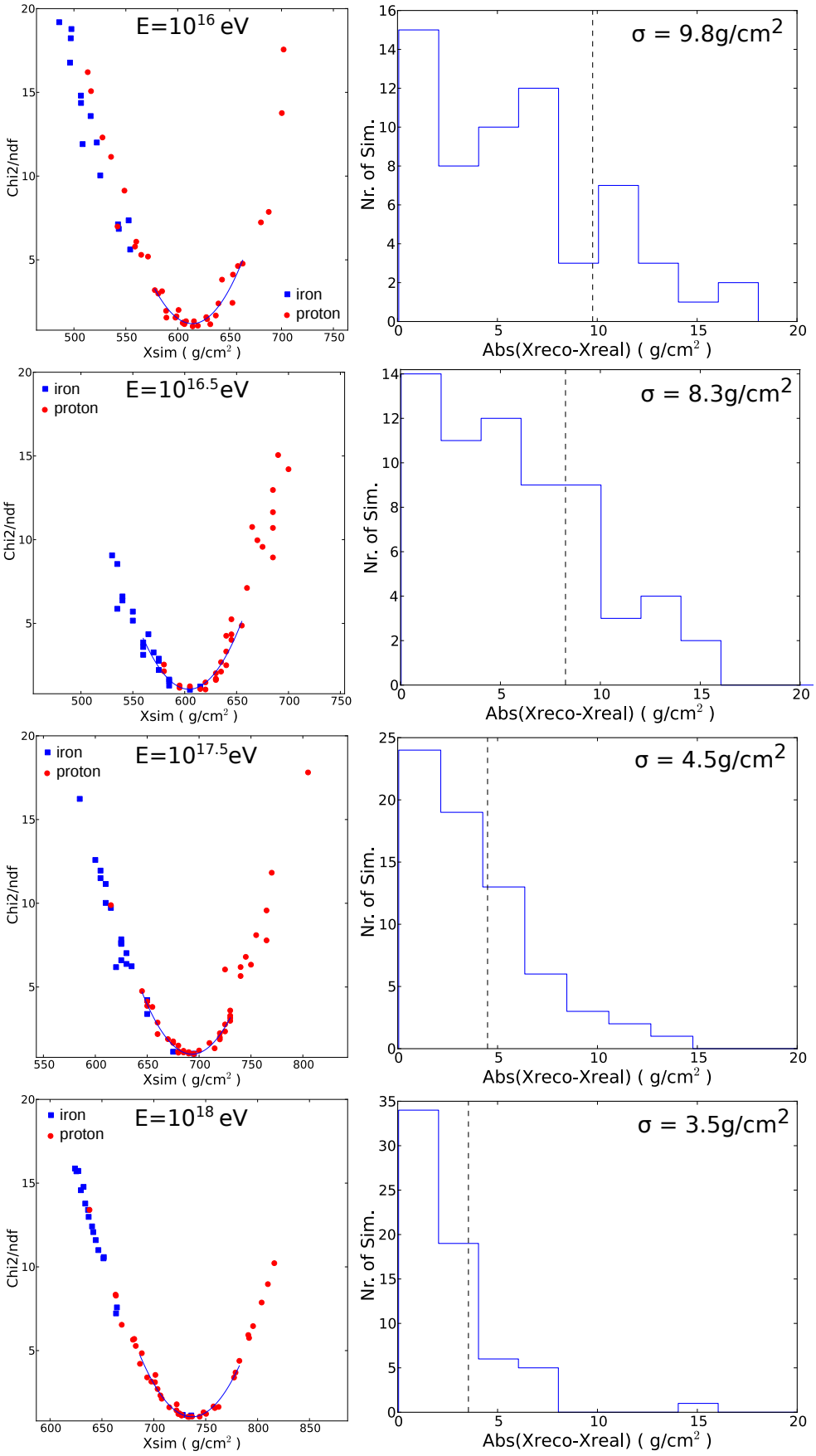

Figure 88: Left: The χ^2 distributions for the SKA1-low array layout for a proton-induced air shower with different primary energies. Right: Histograms for the absolute differences of the reconstructed and the "real" shower depth for the air-shower induced by primaries with different primary energies, leading to reconstruction uncertainties which decreases with rising energy. Some outliers beyond a difference of 20 g/cm^2 are not shown but included in the calculations of the reconstruction uncertainty.

The example χ^2 distributions in the Fig. 88 supports this theory. They are showing the trend that the jitter of the points around the parabola function decreases with higher energies so that the minimum of the parabola and therefore the reconstructed depth of the shower maximum can be determined more precisely. In other words, the uncertainty of the determined minimum decreases.

Especially, for air shower measurements induced by primary particles with high energies, to which SKA1-low will be sensitive, the reconstruction of the depth of the shower maximum on individual air shower events will be extremely precise. With the inclusion of a realistic noise model, it is expected that the shower maximum can be reconstructed even more precisely. The limitations due to the additional statistical and systematic uncertainties (compare to Section 7.5) has to be still evaluated. The tendency of a decreasing uncertainty is not an effect of the signal-to-noise ratio since in this study the noise scales currently with the primary energy. Indeed for low energetic events this assumption could be too optimistic.

7.4.4 Dependence on the zenith angle

In the following, the impact of the zenith angle on the uncertainty of the reconstruction will be studied. Complete simulation sets for a primary energy of $E = 10^{17}$ eV and a zenith angle of 25.84° and 45.58° are compared to the previous results gathered at 36.84°.
Fig. 89 (left) and Fig. 90 (left) show a zoom in the χ^2 distribution ($\pm 150\,\mathrm{g/cm^2}$ around the minimum) for example events for a zenith angle of 25.84° and 45.58°, respectively. It is noticeable that for the higher zenith angle, less simulations lead to a small χ^2/ndf for the comparison to the "fake" data as well as the scatter of the points around the parabolic function gets larger. This could be explained geometrically by that the source of the radio emission is more far away from the ground for larger zenith angles. This leads to the fact that the previously chosen value of 5 for χ^2/ndf, below which the points are included in the parabola fit for finding the minimum, must be adjusted to 9 to ensure that for all comparisons a significant number of points are included in the fit.
In addition, for the larger zenith angle a slight offset between the points of the proton and the iron induced shower is observable in the χ^2 distribution. The origin and whether this include additional information to distinguish between individual primary particles has still to be studied.

Finally, while for the zenith angle of 25.84° the reconstruction uncertainty is $6.1\,\mathrm{g/cm^2}$ (see Fig. 89, right), the uncertainty for the zenith angle of 45.58° is $17.3\,\mathrm{g/cm^2}$ (see Fig. 90, right). The large uncertainty could be explained by the larger distance of the emission source for larger zenith angles and structures in the footprint are less prominent in the radio emission footprint on ground.

The tendency for a higher resolution of the depth of the shower maximum for smaller zenith angles than for large ones could also be caused by the structure of the Cherenkov cone. Fig. 91 shows the mean power distribution along the $\vec{v} \times \vec{B}$ direction averaged over 10 proton-induced air showers for the zenith angles 25.84°, 36.84° and 45.58°.
Due to geometric effects the maximal power decreases and the power distribution gets

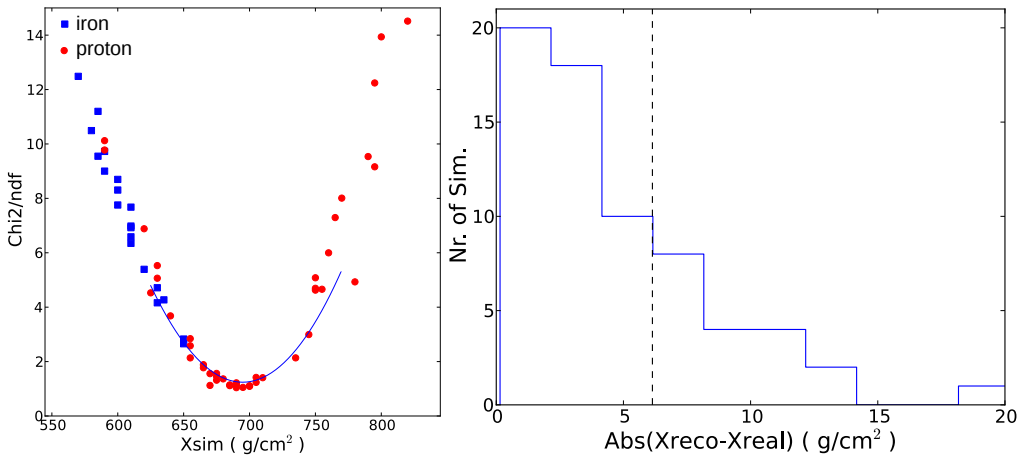

Figure 89: Left: The χ^2 distribution for the SKA1-low array layout for a proton-induced air shower with a primary energy of $E = 10^{17}$ eV and a zenith angle of 25.84°. Right: Histogram for the absolute differences of the reconstructed and the "real" shower depth for the air-shower induced by primaries with an energy of $E = 10^{17}$ eV, leading to a reconstruction uncertainty of 6.1 g/cm^2.

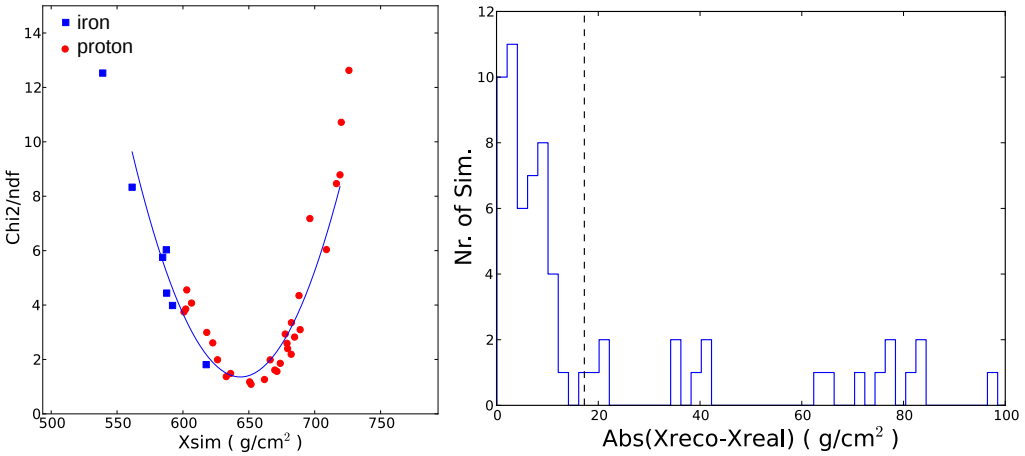

Figure 90: Left: The χ^2 distribution for the SKA1-low array layout for a proton-induced air shower with a primary energy of $E = 10^{17}$ eV and a zenith angle of 45.58°. Right: Histogram for the absolute differences of the reconstructed and the "real" shower depth for the air-shower induced by primaries with an energy of $E = 10^{17}$ eV, leading to a reconstruction uncertainty of 17.3 g/cm^2.

slightly broader as well as the asymmetry of the signal on the Cherenkov cone gets smaller for increasing zenith angles.

7.4.5 Influence of the noise level

To model the background for the radio signal, a combination of system noise of the antenna and noise due to the Galactic background, an additional contribution is added to the simulated radio signal for each antenna. For this study, no valid response model for the SKA1-low antennas was accessible. To assume the impact of noise on the reconstruction uncertainty of the shower maximum, in this study the noise consists of 5% of the power received by the single antenna to model the uncertainty in the antenna-to-antenna calibration

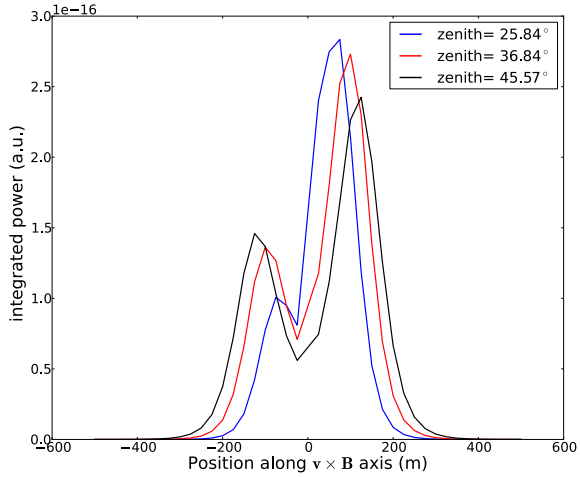

Figure 91: The mean power distribution along the $\vec{v} \times \vec{B}$ axis in shower coordinates, averaged over each 10 proton-induced shower, for the zenith angles 25.84°, 36.84° and 45.58°.

and 1% of the maximal total power received by an antenna in the whole SKA-low array to represents the Galactic noise as background.
This second background contribution, the diffuse emission, mostly from the Galactic plane, can be described with an exponential spectrum [108] in the MHz-frequency band. Radio pulses from air showers are generally detectable above this noise contribution for cosmic-ray energies above $E = 10^{17}$ eV. The detection threshold is about 1 μeV/m/MHz in the frequency range of $30 - 80$ MHz [61]. Since the galactic noise follows an exponential law, the contribution drops rapidly for higher frequencies.
This assumed noise contribution is then added to "measured" total power of each individual antenna, applying an Gaussian distribution to mimic the time-dependence of the noise.

Even if the contribution from noise to the detected radio signal will be small due to modern antenna and system design as well as measuring at higher frequencies, the impact of raising the noise level on the reconstruction uncertainty of the maximum of the shower depth should be studied.

The influence of the antenna response model is explored by varying the uncertainty of the antenna-to-antenna calibration from 5% of the power received by an antenna to 10% (see Fig. 92). In the reconstruction of the depth of the shower maximum, this leads to a larger value for σ in formula 31 for the χ^2-fit. Therefore, even simulations with larger deviations in the structure of the radio footprint on ground return adequate values for the χ^2/ndf. The parabola gets broader and a larger scatter in the minimum position is introduced. Finally, applying the methods for the reconstruction of the depth of the shower maximum returns for a higher noise contribution in the example of a primary energy of $E = 10^{17}$ eV and a zenith angle of 36.84° a larger uncertainty of 11.6 g/cm^2 (see. Fig. 93) as compared to the 6.8 g/cm^2 shown previously in the example in Fig. 77.

In this study, the noise scales with the primary particle energy. For the future, an antenna response model as well as a realistic Galactic noise model have to be included. However, this example study shows that reducing the impact of noise due to the antenna response

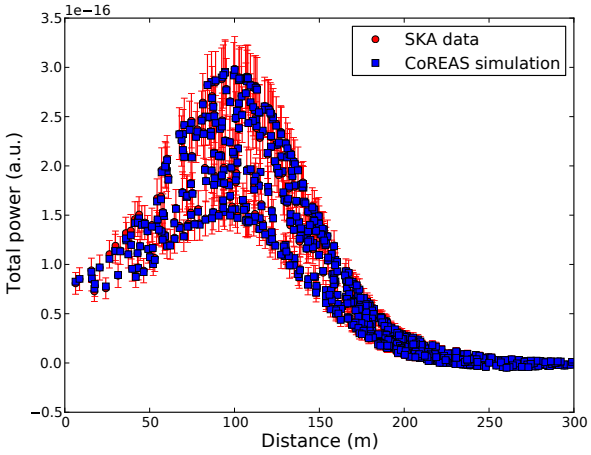

Figure 92: Lateral distribution of the received power by SKA1-low including 10% of the total power as noise level of each antenna. For an easier assignment of the “fake” data to their corresponding simulated signal, only every 64th antenna of the SKA1-low array is plotted.

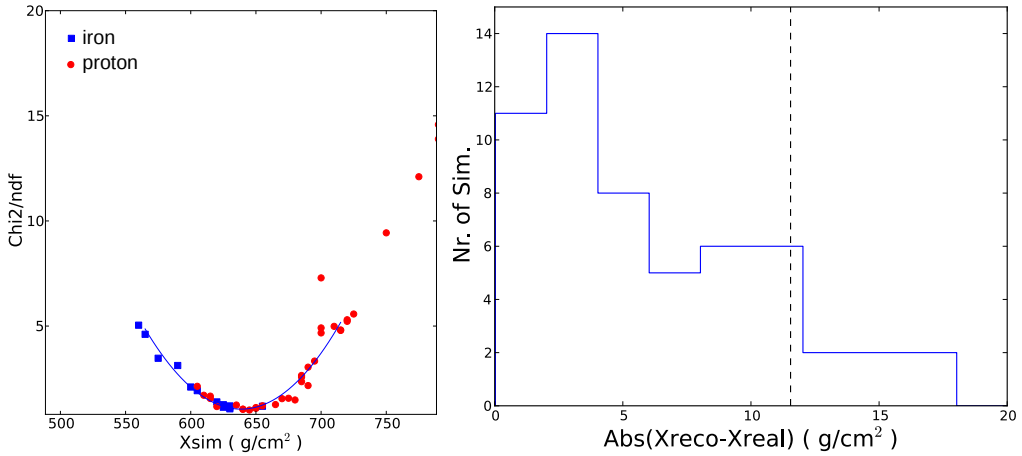

Figure 93: Left: The χ^2 distribution for the SKA1-low array layout for a proton-induced air shower with a primary energy of $E = 10^{17}$ eV. The noise level was raised to 10% of the received power of each antenna. Right: Histogram for the absolute differences of the reconstructed and the “real” shower depth, leading to a reconstruction uncertainty of 11.6 g/cm^2.

model is important to ensure a precise reconstruction of the depth of the shower maximum. Therefore, precise relative calibration of the antennas is crucial.

7.4.6 Impact of the number of simulated antennas and the chosen interpolation method

For the interpolation of the power in shower plane coordinates based on the 160 simulated antenna position, the radial basis function approximation of the ”python” library ”SciPy” is used. This function performs an interpolation on the 2-dimensional scattered data, in this case based on a quintic function ($\propto r^5$).

During the study, the method used for the power interpolation also turned out to be a limiting factor. In the interpolation of the time-integrated power in the shower plane, shown in Fig. 94 (left), dips in the interpolated power distribution are visible between the single rays

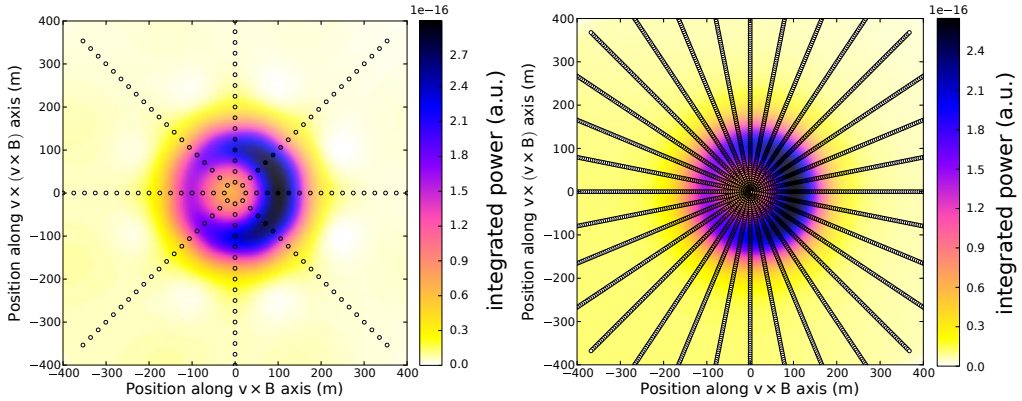

Figure 94: Simulation of a proton-induced air shower with a primary energy of $E = 10^{17}$ eV: time-integrated power for 160 (left) and 3328 (right) simulated antenna positions in the star-shape pattern. The color-code in the background represents the results of the interpolation.

of the star-shape pattern. These were not observed for a frequency band of $30 - 80$ MHz (compare to Fig. 81). These dips seem to be an artifact of the interpolation.
The dips vanish if in exactly the same simulations more antennas (in total 3328 antenna positions) on additional rays in-between the existing ones are simulated and included for the interpolation (see Fig. 94, right).
While for antennas outside the Cherenkov cone there does not seem to be a signal any more, in general the electric field values for the outer antennas seem to be overestimated by the interpolation.

LOFAR claims to have a maximum difference of 2.5% between the interpolated and the directly simulated power for a specific antenna position [74]. The results for the power distribution of SKA1-low array based on the interpolation of 160 and of 3328 antenna positions are shown in Fig. 95 (left). A comparison of the received power received from the interpolation of the 160 and the 3328 antenna positions, respectively, deliver consistent results for most of the SKA1-low antenna positions where a significant signal would be detected, as visible in Fig. 95 (bottom). Just for the outer parts of the Cherenkov ring, the differences in power can achieve values of 10% while the interpolation on the basis of 160 simulated antenna positions overestimate the power received by SKA1-low. Nevertheless, running the simulations with 160 observer positions seems to be precise enough to reconstruct the complete footprint for the SKA1-low array, as long as the inner part of the Cherenkov cone on ground is sampled with a huge number of antennas.

Whether with more simulated antenna positions also possible small-scale structures of the radio footprint can be resolved, which would be smeared out by a too rough simulation pattern, and therefore additional information can be exploited, has to be studied in more detail. A difference between the simulated power interpolated on the basis of 160 simulated antenna positions in comparison to the power achieved from 3328 simulated antenna positions could also become visible in the study of sub-bands of the SKA1-low frequency band or in the high frequency regime.

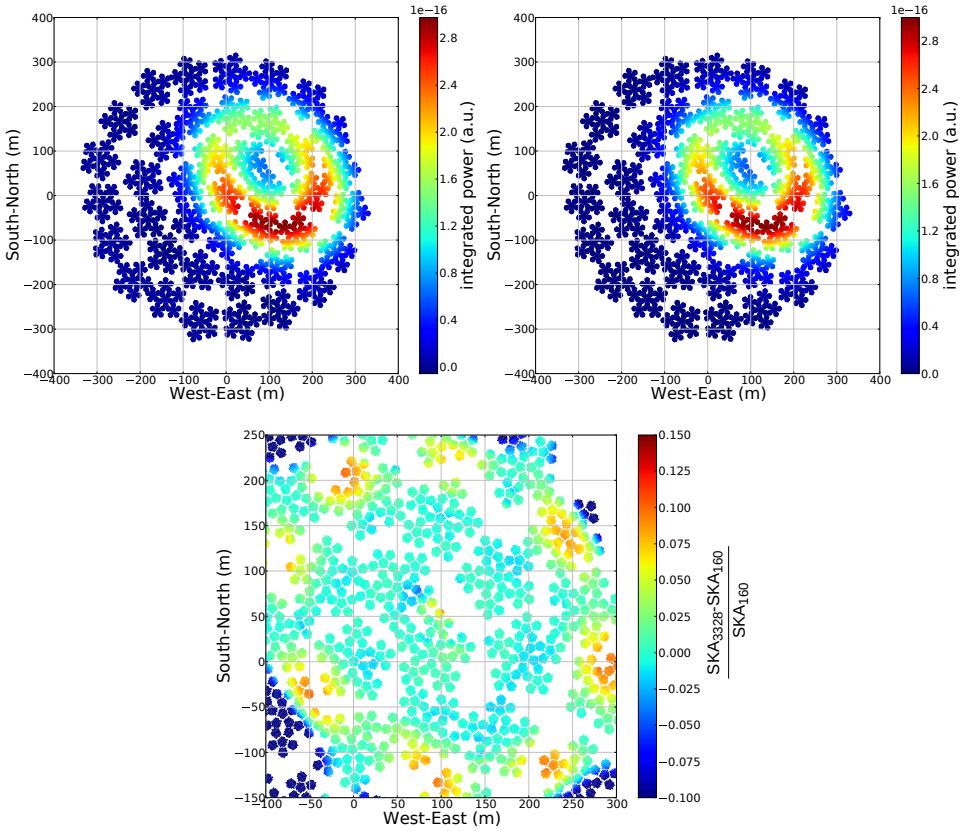

Figure 95: Simulation of a proton-induced air shower with a primary energy of $E = 10^{17}$ eV: Top: received power distribution for the SKA1-low array based on the interpolation of the in time integrated power derived from 160 (left) respectively 3328 (right) simulated antenna positions. Bottom: Relative difference of the simulated power for the SKA1-low array (zoom-in) on the basis of the interpolation between 160 and 3328 antenna positions, respectively.

7.4.7 Ideas for future studies

There are still open questions on the ability of the reconstruction of the shower maximum with the SKA1-low antenna array and the dependency on certain parameters which can be answered in future simulation studies in more detail.

The connection of the reconstruction uncertainty to the parameters defining which simulations in the comparison to a fake event are included has to be explored. In the context of this thesis, a value of $\chi^2/\text{ndf} = 5$ was set while for large zenith angle it was necessary to raise this value to 9 to obtain a consistent fit for the parabola minimum.
In addition, it should be studied in more detail whether the inclusion of more antennas in the reconstruction procedure could improve the reconstruction uncertainty for air shower parameters like e.g. for large zenith angles or near-vertical showers.

In this simulation study, just an approximation for the background noise, reproducing effects due to antenna-to-antenna calibration differences or due to Galactic noise, was used. In following studies a more realistic noise model including a frequency dependency should be included.

Furthermore, a future study could also investigate whether there is any profit in splitting up the frequency band of $50 - 350\,\mathrm{MHz}$ into smaller bands for the interpolation of the power in the shower plane as well as for the whole study. This large SKA1-low frequency band could contain more information which is washed out due to integration of the power over the whole band.

For now, just proton- and iron-induced showers were included in the study of the ability of SKA1-low to reconstruct the depth of the shower maximum for individual air-shower events. It was shown that this reconstruction method used for an array as envisaged for SKA1-low could achieve an intrinsic uncertainty of about $6\,\mathrm{g/cm^2}$. An inclusion of simulations of air-shower events induced by further cosmic rays elements such as hydrogen or nitrogen, besides the both extremes, proton and iron, could show the ability to decompose the measured energy spectrum into individual element spectra. In addition, a future simulations study should also investigate a possible gain in the reconstruction precision by including information beyond the total power such as the timing information of the signal or its polarisation.

7.5 LIMITATIONS IN APPLYING THE METHOD TO MEASURED DATA

In the reconstruction of the depth of the shower maximum for measured data events, a first comparison to simulation sets of air showers narrows the possible parameters of the primary particle down. After this, simulations with these specific input parameters can be reproduced as done for LOFAR [109]. Especially, if the range around the true X_{max} is not sufficiently covered by the existing simulations, simulations with specific depths can be reproduced to include them in the reconstruction procedure for a more precise result. The resulting reconstructed depth depends on the selection of simulations, even if a high number of simulations were done to minimise the impact.

In comparison to the intrinsic reconstruction uncertainty of about $6\,\mathrm{g/cm^2}$ achieved in this simulation study, the results of the application of this method to measured data could be dominated by experimental uncertainties.
If this method, achieving an intrinsic uncertainty of the reconstruction method of about $6\,\mathrm{g/cm^2}$, is applied to measured data, additional experimental uncertainties have to be included as the fact how well the atmosphere at the time of detection is known.

7.5.1 Statistical uncertainties

The measurements of the power of individual antennas is affected by three different sources of statistical uncertainties. The first one is the contribution from background noise, which is a combination of system noise of the antenna itself and noise due to the Galactic background. The second contribution arises from the uncertainties from the antenna response model, especially from the differences between the responses of the single antennas. In addition, even if the uncertainty introduced by interpolation of simulated signals is small, this error has to be included. This is not an uncertainty of the measurement, but has to be taken into account when fitting the data to the simulation.

Furthermore, the included atmospheric model influence the results. The simulations ran with the US standard atmosphere model. In practical application, the reconstructed shower depth has to be corrected for the variations in the atmosphere, using the Global Data Assimilation System (GDAS) of the NOAA National Climatic Data Center. For LOFAR, it was shown that the remaining uncertainty due to the atmosphere model is of the order of 1 g/cm^2 [73].

The index of refraction is implemented in the simulation program as a function of the density. But the index also depends on the relative humidity. So, local weather information has to be used to correct the reconstructed depth for this impact. Based on studies for LOFAR, refractive index variations are assumed to introduce an additional uncertainty of about $\pm$5 g/cm^2.

7.5.2 Systematic uncertainties

The reconstruction of the depth of the shower maximum is sensitive to the choice of the the hadronic interaction model in the simulations. In this study, QGSJET-II-04 [19] is used. A comparison to SYBILL 2.1 or EPOS-LHC will introduce an systematic uncertainty of a few g/cm^2 [73].

Another source of a systematic uncertainty is the code for the simulation of the radio emission itself. As already demonstrated in Chapter 6 the two formalisms for the calculation of the radio emission from particle showers, the endpoint and the ZHS formalisms, deliver results which are consistent with each other and it was also shown that they can reproduce the expected radio signal from a particle shower. As already mentioned, the endpoint formalism is implemented in CoREAS, while the ZHS formalism is applied in ZHAireS. Differences in their simulation results are most likely originated in the usage of different hadronic interaction models, atmospheres, thinning strategies and refractive index models [110] since both are using different air shower simulation codes, CORSIKA and AIRES, respectively. That is the reason why the choice of the radio emission code used for producing the simulated radio signal should not lead to an additional uncertainty, besides the one of the hadronic interaction model.

In applying the method for the shower depth reconstruction to measured data, an additional uncertainty would come up due to an energy cut on air shower events. This could be a source of a bias on the reconstructed mass composition [73]. However, this bias would just have a small effect since energy and the shower depth of an event would be fit simultaneously. In this performed simulation study, the energy of the primary particle was fixed.

7.5.3 Profiting from the high X_{max} resolution

A mean uncertainty on the reconstruction of the shower depth of about 6 g/cm^2, as the intrinsic uncertainty by the method, seems to be feasible to achieve with SKA1-low. This

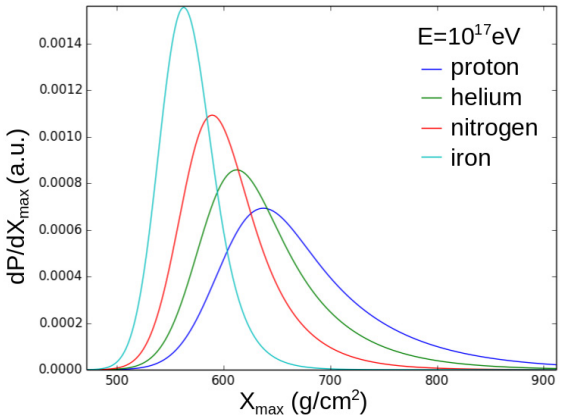

Figure 96: Differential particle distribution as a function of the shower depth X_{max} for different elements as primaries with an energy of 10^{17} eV [109].

would mean a factor of 3 improvement in the resolution of the X_{max} measurement in comparison to LOFAR and a factor of almost 4 with respect to the fluorescence detection technique.

To distinguish the different models for the sources and propagation of the cosmic rays, a measurement of the proton-to-helium ratio in the cosmic ray flux would provide very valuable information. As illustrated in Fig. 96, the average difference in the shower depth for proton- and helium-induced air showers is about 30 g/cm^2, with large shower-to-shower fluctuations. While a 16 g/cm^2 resolution of LOFAR seems to be insufficient, with the SKA1-low array it seems to be feasible to measure the p-He ratio, but this will still be very challenging.

A big gain will come from the higher detection rate. Large statistics will be essential for the decomposition of the cosmic ray flux into individual elements since the shape of the distribution, as shown in Fig. 96, can be measured precisely.

Nevertheless, from an example study on expected variance of Maximum Likelihood estimate on the helium fraction in the cosmic ray flux, assuming that the mass composition consists of 10% helium and 90% proton, the improvement of the X_{max} resolution from 20 g/cm^2 to 10 g/cm^2 would lead only to an 11% improvement in the helium fraction measurement [111]. Even this small improvement will be lost if low X_{max} values are cut away ($X_{max} < 600$ g/cm^2), which might be necessary to reduce the impact of heavier elements than hydrogen.

Additional observables beyond the shower depth which are sensitive to the mass composition will be needed to measure the helium-to-proton ratio: Profiting from the larger statistics, besides the maximum, also other features in the distribution of the shower maximum can be compared in an analysis, e.g. the tails of the X_{max} distribution where the separation between proton- and helium-induced air showers becomes clearer. SKA1-low should also measure the radio footprint of individual events detailed enough to get additional informations from other shape parameters, which could constrain the primary mass, e.g. the R and L parameters to describe the shape of the shower profile, known from fluorescence detection of air showers [112]. Additionally, it has to be studied whether the inclusion of sig-

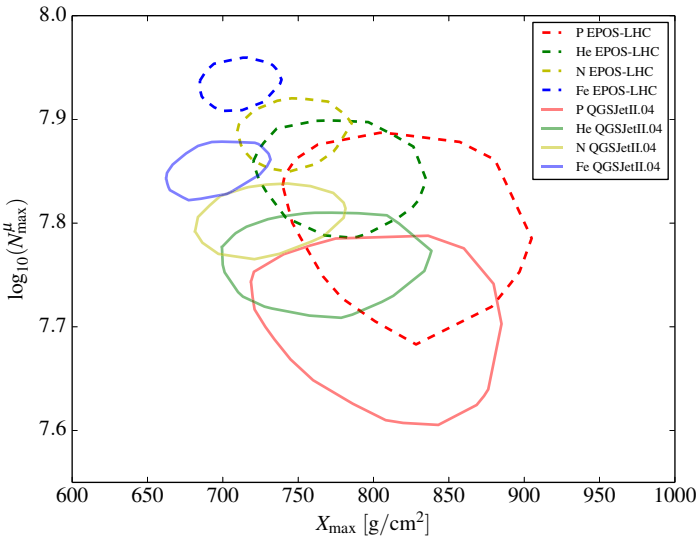

Figure 97: The 1σ contour plot of the number of muons at maximum of the muon shower development ($\log_{10}(N_{\mu,\max})$) vs. the depth of the shower maximum $X_{\max}$ for a primary energy of $E = 10^{19}$ eV and fixed zenith angle of 38° [113]. The simulations were performed for different primary particles and with different hadronic interaction models.

nal timing, pulse shape and polarisation measurements would yield additional information beyond the pure determination of $X_{\max}$.

In comparison to LOFAR, SKA1-low will also profit from a larger energy range to which it will be sensitive and therefore more energy bins will be included in the statistical analysis. With respect to fluorescence measurements as done with HEAT [36], SKA1-low will deliver independent measurements on the mass composition, with different systematic uncertainties and an extension of the measurements to lower energies.

7.5.3.1 Additional information from particle detector measurements

Since the measured number of muons from an air shower measured on ground is sensitive to the mass composition (compare to Sec. 7.2), additional information from the particle detector array could be used in the reconstruction of the depth of the shower maximum. This is also done in the measurements performed by LOFAR [73]. The lateral distribution of the measured muons on ground and their energy are included in the χ^2 fit as described in [74]. Including the information gained from the particle detector array, which will be assembled at the SKA1-low site for triggering air-shower events (see Sec. 7.1.1.1), could deliver additional parameters from which a separation between proton- and helium-induced air showers would become possible. For example, in Fig. 97 it is shown that the maximum number of muons can deliver additional informations about the primary particle as shown in a simulations study for AugerPrime, the Pierre Auger Observatory Upgrade [113]. The profit from reading out information from the particle detectors has to be explored in a future study.

7.6 SUMMARY AND OUTLOOK

In the initial simulation study presented in this thesis, it was demonstrated that a LOFAR-like approach for the reconstruction of the shower depth for single events is applicable to

SKA1-low data. It could be shown that in the energy region of the transition from Galactic to Extragalactic origin of cosmic rays the SKA1-low array could achieve a mean intrinsic reconstruction uncertainty of about 6 g/cm^2 for the depth of the shower maximum of individual air shower events, significantly less than 10 g/cm^2.

The reconstruction profits especially from the very dense antenna array of the SKA1-low array, but also from the larger bandwidth at higher frequencies in comparison to LOFAR. It could be demonstrated that to reduce the data stream, as well as the costs to enable SKA1-low as a cosmic ray detector, not all antennas have to be read out after the detection of an air shower event. The number can be reduced while it has to be studied in more detail to which number exactly.

The influence of experimental uncertainties (realistic background noise, impact of the dynamic range, uncertainty in the atmospheric properties, ...) has to be evaluated in a future study as well.
With SKA1-low as cosmic ray detector an improvement of more than a factor of three in comparison to the fluorescence detection technique with $\sim$ 20 g/cm^2 [36] seems to be feasible.

A separation of proton- and helium-induced air showers to decompose the cosmic ray spectrum into individual element spectra, seems to be even with this high precision in the reconstruction of the shower depth not easily achievable. Additional information is needed. Therefore, a further simulation study is needed to explore whether the measurements of the particle detector can deliver these or whether the radio signal itself contains additional informations beyond the shower maximum.

8 CONCLUSION

The interpretation of air-shower measurements via radio detection is based on predictions from simulations. CoREAS, using the endpoint formalism, and ZHAireS, using the ZHS formalism, can be considered as the current state-of-the-art to calculate the radio signal from air showers. Both use a full Monte-Carlo simulation of the air shower as basis for the calculations, without any simplifying approximations made in the process of emission.
Before this thesis, it was already shown that the predictions for the radio signal from an air shower by the two formalisms agree within $\approx$ 20%. The deviations between CoREAS and ZHAireS are assumed to arise mostly from the underlying air-shower simulation with CORSIKA and AIRES, respectively, possibly due to the used hadronic interaction models, the choice of energy cuts for the simulation of the particle cascades or due to a different model for the atmospheric refractive index. Before this thesis, a direct comparison of the results from the two formalisms independent of these uncertainties and under well-defined laboratory conditions has not been performed so far.

In the context of this thesis, the open question was whether the established microscopic simulations are able to predict radio emission from a well-defined particle shower induced by a pure electron beam, measured under laboratory conditions.
The SLAC T-510 experiment, to which this thesis contributed, could provide a laboratory benchmark for radio frequency radiation from electromagnetic cascades under the influence of a strong magnetic field. Within this thesis, microscopic Geant4 simulations were prepared and performed, including both formalisms running in parallel. It could be shown that the formalisms produce results agreeing within about 5% to each other. A comparison of the expectations from simulations to measured data led to the conclusion that both formalisms can predict the absolute scale of the radio signal produced by a particle shower accurately within the uncertainties of the SLAC T-510 experiment of roughly 30%. On the basis of the simulations, it could be demonstrated that internal reflection of the radio signal at the bottom surface of the target explains the apparent discrepancy of the measured data to the predictions. The effects of the reflections are not fully determined and are thus counted in as systematic uncertainty.
In addition to the scaling of the emitted radio signal with the magnetic field strength as well as the formation of a Cherenkov cone for the vertically as well as for the horizontally polarised component of the radio emission, which were measured in the experiment as features of the radio emission from particle showers, could also be reproduced by the simulations within the systematic uncertainties.

The comparison of the measured data of the SLAC T-510 experiment with the results of the detailed simulation study could confirm the validity of the prediction of microscopic calculations with different systematic uncertainties than in air shower measurements, such as uncertainties in the hadronic interaction models. While the SLAC T-510 experiment does not exactly replicate the physics of an extensive air shower, a good agreement of the predic-

tions and the measurements ensures the applicability of the conclusions also to air-shower detection. The systematic uncertainties of the experiment are not yet competitive with air-shower measurements, but a follow-up experiment can reduce them significantly.

For the interpretation of the measured data of air-shower experiments a reduction of the uncertainties in the predictions of the radio signal is necessary, especially for future high-precision experiments in the radio detection of cosmic rays such as the future SKA1-low antenna array. SKA1-low will sample the radio footprint on ground with extreme resolution and, therefore, it will be sensitive even to the smallest structures.

In the initial simulation study presented in this thesis, it was demonstrated that a LOFAR-like approach for the reconstruction of the shower depth for single air-shower events, based on the comparison of simulated two-dimensional lateral distribution functions to measured data, is also applicable to SKA1-low data. It could be demonstrated that in the energy region of the presumed transition from Galactic to Extragalactic origin of cosmic rays the SKA1-low array could achieve a mean intrinsic reconstruction uncertainty of about 6 g/cm^2 for the depth of the shower maximum of individual air-shower events.
It could be shown that the reconstruction profits especially from the very dense antenna array of the SKA1-low array, but also from the larger bandwidth at higher frequencies in comparison to LOFAR. With SKA1-low as a cosmic ray detector an improvement of more than a factor of three in comparison to the current uncertainty in the shower-maximum reconstruction given by the fluorescence detection technique seems feasible. Therefore, SKA1-low has the potential to measure the mass composition of cosmic rays in the transition region from Galactic to Extragalactic origin the most precisely.
However, a separation of proton- and helium-induced air showers to decompose the cosmic ray spectrum into individual element spectra, seems to be not easily achievable with the current approach. In a future simulation study, it has to be explored whether additional information on the shower maximum or even beyond can be obtained from the radio signal itself or from hybrid measurements with a particle detector array. In addition, the influence of experimental uncertainties, such as a realistic background noise, has to be evaluated in a future study in more detail.

BIBLIOGRAPHY

[1] K. Zuber. *Neutrino Physics*. CRC Press, Taylor and Francis, 2. edition, 2012.

[2] V. Verzi. Cosmic Rays: air showers from low to high energies - Rapporteur Report. In *Proceedings, 34th International Cosmic Ray Conference (ICRC 2015): PoS(ICRC2015)015*, 2016. URL http://pos.sissa.it/archive/conferences/236/015/ICRC2015_015.pdf.

[3] W.D. Apel et al. KASCADE-Grande measurements of energy spectra for elemental groups of cosmic rays. *Astropart. Phys.*, 47:54 – 66, 2013. doi: 10.1016/j.astropartphys.2013.06.004.

[4] V.V. Prosin et al. Tunka-133: Results of 3 year operation. *Nucl. Instr. Meth. Phys. Res. A*, 756:94 – 101, 2014. doi: 10.1016/j.nima.2013.09.018.

[5] M. G. Aartsen et al. Measurement of the cosmic ray energy spectrum with IceTop-73. *Phys. Rev. D*, 88(4):042004, 2013. doi: 10.1103/PhysRevD.88.042004.

[6] W.D. Apel et al. Kneelike structure in the spectrum of the heavy component of cosmic rays observed with KASCADE-Grande. *Phys. Rev. Lett.*, 107:171104, 2011. doi: 10.1103/PhysRevLett.107.171104.

[7] J. Abraham et al. Measurement of the energy spectrum of cosmic rays above 10^{18} eV using the Pierre Auger Observatory. *Phys. Lett. B*, 685(4-5):239 – 246, 2010. doi: 10.1016/j.physletb.2010.02.013.

[8] K. Greisen. End to the cosmic-ray spectrum? *Phys. Rev. Lett.*, 16:748–750, 1966. doi: 10.1103/PhysRevLett.16.748.

[9] G.T. Zatsepin and V.A. Kuzmin. Upper limit of the spectrum of cosmic rays. *JETP Lett.*, 4:78–80, 1966. URL http://adsabs.harvard.edu/abs/1966JETPL...4...78Z.

[10] D. Allard, E. Parizot, E. Khan, S. Goriely, and A. V. Olinto. UHE nuclei propagation and the interpretation of the ankle in the cosmic-ray spectrum. *Astron. Astrophys.*, 443:L29–L32, 2005. doi: 10.1051/0004-6361:200500199.

[11] T.K. Gaisser, R. Engel, and E. Resconi. *Cosmic Rays and Particle Physics*. Cambrigde University Press, 2nd edition, 2016.

[12] E.S. Seo. Direct measurements of cosmic rays using balloon borne experiments. *Astropart. Phys.*, 39 - 40:76 – 87, 2012. doi: 10.1016/j.astropartphys.2012.04.002.

[13] I. De Mitri, N. Giglietto, G. Marsella, A. Surdo, and R. Sparvoli. From high energy gamma sources to cosmic rays, one century after their discovery direct measurements of cosmic rays in space. In *Proceedings, 9th workshop on Science with the New Generation of High Energy Gamma-ray Experiments*, 2013. doi: 10.1016/j.nuclphysbps.2013.05.019.

[14] A. Haungs, H. Rebel, and M. Roth. Energy spectrum and mass composition of high-energy cosmic rays. *Rep. Prog. Phys.*, 66(7):1145, 2003. URL http://stacks.iop.org/0034-4885/66/i=7/a=202.

[15] R. Engel, D. Heck, and T. Pierog. Extensive air showers and hadronic interactions at high energy. *Ann. Rev. Nucl. Part. Sci.*, 61:467–489, 2011. doi: 10.1146/annurev.nucl.012809.104544.

[16] W. Heitler. *The Quantum Theory of Radiation*. Oxford University Press, 1944.

[17] J. Blümer, R. Engel, and J.R. Hörandel. Cosmic rays from the knee to the highest energies. *Prog. Part. Nucl. Phys.*, 63(2):293 – 338, 2009. doi: 10.1016/j.ppnp.2009.05.002.

[18] B.F. Rauch et al. Cosmic Ray origin in OB Associations and Preferential Acceleration of Refractory Elements: Evidence from Abundances of Elements 26Fe through 34Se. *Astrophys. J.*, 697(2):2083, 2009. doi: 10.1088/0004-637X/697/2/2083.

[19] S. Ostapchenko. QGSJET-II: physics, recent improvements, and results for air showers. In *Proceedings, 17th International Symposium on Very High Energy Cosmic Ray Interactions (ISVHECRI 2012)*, 2013. doi: 10.1051/epjconf/20125202001.

[20] E.-J. Ahn, R. Engel, T.K. Gaisser, P. Lipari, and T. Stanev. Cosmic ray interaction event generator SIBYLL 2.1. *Phys. Rev. D*, 80:094003, 2009. doi: 10.1103/PhysRevD.80.094003.

[21] K. Werner. The hadronic interaction model EPOS. *Nucl. Phys. B - Proc. Sup.*, 175:81–87, 2008. doi: 10.1016/j.nuclphysbps.2007.10.012.

[22] M. Unger. Report of the Working Group on the Composition of Ultra-High Energy Cosmic Rays. In *Proceedings, 34th International Cosmic Ray Conference (ICRC 2015): PoS(ICRC2015)307*, 2015. doi: 10.7566/JPSCP.9.010016.

[23] F.G. Schroeder. Radio detection of Cosmic-Ray Air Showers and High-Energy Neutrinos. 2016. To be published in Prog. Part. Nucl. Phys.. arXiv:1607.08781.

[24] M. Ostrowski. Mechanisms and sites of ultrahigh-energy cosmic ray origin. *Astropart. Phys.*, 18:229–236, 2002. doi: 10.1016/S0927-6505(02)00154-8.

[25] J. Abraham et al. Correlation of the highest energy cosmic rays with nearby extragalactic objects. *Science*, 318:938–943, 2007. doi: 10.1126/science.1151124.

[26] E. Fermi. On the origin of the Cosmic Radiation. *Phys. Rev.*, 75(8):1169–1174, 1949. doi: 10.1103/PhysRev.75.1169.

[27] A.M. Hillas. Can diffusive shock acceleration in supernova remnants account for high-energy galactic cosmic rays? *J. Phys. G Nucl. Partic.*, 31:R95–R131, 2005. doi: 10.1088/0954-3899/31/5/R02.

[28] D. Caprioli. Cosmic-ray Acceleration and Propagation. In *Proceedings, 34th International Cosmic Ray Conference (ICRC 2015): PoS(ICRC2015)008*, 2016. arXiv:1510.07042.

[29] F. Aharonian. Primary particle acceleration above 100 TeV in the shell-type Supernova Remnant RX J1713.7-3946 with deep H.E.S.S. observations. *Astron. Astrophys.*, 464:235–243, 2007. doi: 10.1051/0004-6361:20066381.

[30] W.D. Apel et al. The KASCADE-Grande experiment. *Nucl. Instr. Meth. Phys. Res. A*, 620:202–216, 2010. doi: 10.1016/j.nima.2010.03.147.

[31] A. Aab et al. The Pierre Auger Cosmic Ray Observatory. *Nucl. Instr. Meth. Phys. Res. A*, 798:172 – 213, 2015. doi: 10.1016/j.nima.2015.06.058.

[32] D. Borla Tridon, T. Schweizer, F. Goebel, R. Mirzoyan, and M. Teshima. The MAGIC-II gamma-ray stereoscopic telescope system . *Nucl. Instr. Meth. Phys. Res. A*, 623(1): 437 – 439, 2010. doi: 10.1016/j.nima.2010.03.028.

[33] J. Bolmont et al. The camera of the fifth H.E.S.S. telescope. Part I: System description. *Nucl. Instr. Meth. Phys. Res. A*, 761:46–57, 2014. doi: 10.1016/j.nima.2014.05.093.

[34] I. Anatoly. The Yakutsk array experiment: Main results and future directions. In *Proceedings, International Symposium on Future Directions in UHECR Physics (UHECR2012)*, 2013. doi: 10.1051/epjconf/20135304003.

[35] M. Ricci. The JEM-EUSO Program. In *Proceedings, 14th International Conference on Topics in Astroparticle and Underground Physics (TAUP 2015)*, 2016. doi: 10.1088/1742-6596/718/5/052034.

[36] A. Aab et al. Depth of maximum of air-shower profiles at the Pierre Auger Observatory. I. Measurements at energies above $10^{17.8}$ eV. *Phys. Rev. D*, 90:122005, 2014. doi: 10.1103/PhysRevD.90.122005.

[37] G.A. Askaryan. Excess negative charge of an electron-photon shower and its coherent radio emission. *Soviet Physics JETP, 14*, 1962.

[38] G.A. Askaryan. Coherent radio emission from cosmic showers in air and in dense media. *Soviet Physics JETP, 21*, 1965. URL http://adsabs.harvard.edu/abs/1965JETP...21..658A.

[39] D. Saltzberg et al. Observation of the Askaryan Effect: Coherent Microwave Cherenkov Emission from Charge Asymmetry in High-Energy Particle Cascades. *Phys. Rev. Lett.*, 86:2802–2805, Mar 2001. doi: 10.1103/PhysRevLett.86.2802.

[40] P.W. Gorham, D. Saltzberg, R. C. Field, E. Guillian, R. Milincic, D. Walz, and D. Williams. Accelerator measurements of the Askaryan effect in rock salt: A Roadmap toward teraton underground neutrino detectors. *Phys. Rev. D*, 72:023002, 2005. doi: 10.1103/PhysRevD.72.023002.

[41] P.W. Gorham et al. Observations of the Askaryan Effect in Ice. *Phys. Rev. Lett.*, 99: 171101, 2007. doi: 10.1103/PhysRevLett.99.171101.

[42] A. Aab et al. Probing the radio emission from air showers with polarization measurements. *Phys. Rev. D*, 89:052002, 2014. doi: 10.1103/PhysRevD.89.052002.

[43] H. Allan, R. Clay, and J. Jones. Radio Pulses from Extensive Air Showers. *Nature, 227, pp. 1116 - 1118*, 1970. URL http://www.nature.com/nature/journal/v217/n5127/pdf/217440a0.pdf.

[44] D. Ardouin et al. Geomagnetic origin of the radio emission from cosmic ray induced air showers observed by CODALEMA. *Astropart. Phys.*, 31(3):192 – 200, 2009. doi: 10.1016/j.astropartphys.2009.01.001.

[45] N. Palmieri et al. Investigation on the energy and mass composition of cosmic rays using LOPES radio data. In *Proceedings, 33rd International Cosmic Ray Conference (ICRC2013): ID 0439*, page 0439, 2013. arXiv:1309.2410.

[46] A. Aab et al. Energy estimation of cosmic rays with the Engineering Radio Array of the Pierre Auger Observatory. *Phys. Rev. D*, 93:122005, 2016. doi: 10.1103/PhysRevD.93.122005.

[47] A. Nelles. Measuring air showers with the LOFAR radio telescope. In *Proceedings, 33rd International Cosmic Ray Conference (ICRC2013):ID 0558*. URL http://www.cbpf.br/~icrc2013/papers/icrc2013-0558.pdf.

[48] R. Hiller et al. Calibration of the absolute amplitude scale of the Tunka Radio Extension. In *Proceedings, 34th International Cosmic Ray Conference (ICRC 2015): PoS(ICRC2015)573*, 2015. arXiv:1508.06210.

[49] O. et al. Scholten. Measurement of the circular polarization in radio emission from extensive air showers confirms emission mechanisms. *Phys. Rev. D*, 94:103010, 2016. doi: 10.1103/PhysRevD.94.103010.

[50] T. Huege, M. Ludwig, and C.W. James. Simulating radio emission from air showers with CoREAS. *AIP Conf. Proc.*, 1535:128, 2013. doi: 10.1063/1.4807534.

[51] J.D. Jackson. *Classical Electrodynamics*. Wiley&Sons, New York, 3rd edition, 1999.

[52] C.W. James, H. Falcke, T. Huege, and M. Ludwig. General description of electromagnetic radiation processes based on instantaneous charge acceleration in 'endpoints'. *Phys. Rev. E*, 84:056602, 2011. doi: 10.1103/PhysRevE.84.056602.

[53] E. Zas, F. Halzen, and T. Stanev. Electromagnetic pulses from high-energy showers: Implications for neutrino detection. *Phys. Rev. D*, 45:362–376, 1992. doi: 10.1103/PhysRevD.45.362.

[54] J. Alvarez-Muñiz, A. Romero-Wolf, and E. Zas. Cherenkov radio pulses from electromagnetic showers in the time-domain. *Phys. Rev. D*, 81:123009, 2010. doi: 10.1103/PhysRevD.81.123009.

[55] D. Heck, G. Schatz, T. Thouw, J. Knapp, and J.N. Capdevielle. CORSIKA: A Monte Carlo code to simulate extensive air showers. 1998. URL https://web.ikp.kit.edu/corsika/physics_description/corsika_phys.pdf. FZKA Report 6019, Forschungszentrum Karlsruhe.

[56] T. Huege, M. Ludwig, and C.W. James. Simulating radio emission from air showers with CoREAS. *AIP Conf. Proc.*, 1535:128, 2013. doi: 10.1063/1.4807534.

[57] S. J. Sciutto. AIRES: A System for air shower simulations. User's guide and reference manual. Version 2.2.0. 1999. arXiv:astro-ph/9911331.

[58] J. Alvarez-Muñiz, W.R. Carvalho Jr., and E. Zas. Monte Carlo simulations of radio pulses in atmospheric showers using ZHAireS. *Astropart. Phys.*, 35(6):325 – 341, 2012. doi: 10.1016/j.astropartphys.2011.10.005.

[59] N.N. Kalmykov, A.A. Konstantinov, and R. Engel. Radio emission from extensive air showers as a method for cosmic-ray detection. *Phys. Atom. Nucl.*, 73:1191–1202, 2010. doi: 10.1134/S1063778810070136.

[60] K. Belov. Radio emission from Air Showers. Comparison of theoretical approaches. *AIP Conf. Proc.*, 1535:157, 2013. doi: 10.1063/1.4807540.

[61] T. Huege. Radio detection of cosmic ray air showers in the digital era. *Phys. Rep.*, 620:1–52, 2016. doi: 10.1016/j.physrep.2016.02.001.

[62] T. Huege et al. The LOPES experiment - recent results, status and perspectives. In *Proceedings, 4th International Workshop on Acoustic and Radio EeV Neutrino Detection Activities (ARENA 2010)*, 2012. doi: 10.1016/j.nima.2010.11.081.

[63] A. Haungs et al. High-energy cosmic rays measured with KASCADE-Grande. In *Proceedings, 33rd International Cosmic Ray Conference (ICRC2013): ID 0398*, 2013. arXiv:1308.1485.

[64] H. Falcke et al. Detection and imaging of atmospheric radio flashes from cosmic ray air showers. *Nature*, 435:313–316, 2005. doi: 10.1038/nature03614.

[65] S. Buitink et al. Amplified radio emission from cosmic ray air showers in thunderstorms. *Astron. Astrophys.*, 467:385–394, 2007. doi: 10.1051/0004-6361:20066006.

[66] W.D. Apel et al. Reconstruction of the energy and depth of maximum of cosmic-ray air-showers from LOPES radio measurements. *Phys. Rev. D*, 90(6):062001, 2014. doi: 10.1103/PhysRevD.90.062001.

[67] S. Fliescher. Radio detection of cosmic ray induced air showers at the Pierre Auger Observatory. In *Proceedings, 4th International workshop on Acoustic and Radio EeV Neutrino detection Activities*, 2012. doi: 10.1016/j.nima.2010.11.045.

[68] S. Hoover et al. Observation of Ultrahigh-Energy Cosmic Rays with the ANITA Balloon-Borne Radio Interferometer. *Phys. Rev. Lett.*, 105(15):151101, 2010. doi: 10.1103/PhysRevLett.105.151101.

[69] A. Nelles et al. Detecting Radio Emission from Air Showers with LOFAR. *AIP Conf. Proc.*, 1535:105, 2013. doi: 10.1063/1.4807530.

[70] P. Schellart et al. Detecting cosmic rays with the LOFAR radio telescope. *Astron. Astrophys.*, 560:A98, 2013. doi: 10.1051/0004-6361/201322683.

[71] S. Thoudam et al. LORA: A scintillator array for LOFAR to measure extensive air showers. *Nucl. Instrum. Meth.*, A767:339–346, 2014. doi: 10.1016/j.nima.2014.08.021.

[72] A. Nelles, S. Buitink, H. Falcke, J. Hörandel, T. Huege, and P. Schellart. A parameterization for the radio emission of air showers as predicted by CoREAS simulations and applied to LOFAR measurements. *Astropart. Phys.*, 60:13–24, 2015. doi: 10.1016/j.astropartphys.2014.05.001.

[73] S. Buitink et al. A large light-mass component of cosmic rays at $10^{17} - 10^{17.5}$ eV from radio observations. *Nature*, 531:70, 2016. doi: 10.1038/nature16976.

[74] S. Buitink et al. Method for high precision reconstruction of air shower X_{max} using two-dimensional radio intensity profiles. *Phys. Rev. D*, 90(8):082003, 2014. doi: 10.1103/PhysRevD.90.082003.

[75] T. Huege. Theory and simulations of air shower radio emission. In *Proceedings, 5th International Workshop on Acoustic and Radio EeV Neutrino Detection Activities (ARENA 2012)*, 2012. doi: 10.1063/1.4807533.

[76] F.G. Schröder. Radio detection of air showers with the Auger Engineering Radio Array. In *Proceedings, 33rd International Cosmic Ray Conference (ICRC2013): ID 0899*, 2013. URL http://www.cbpf.br/%7Eicrc2013/papers/icrc2013-0899.pdf.

[77] K. Link et al. Revised absolute amplitude calibration of the LOPES experiment. In *Proceedings, 34th International Cosmic Ray Conference (ICRC 2015): PoS(ICRC2015)311*, 2016. arXiv:1508.03471.

[78] P. A. Bezyazeekov et al. Measurement of cosmic-ray air showers with the Tunka Radio Extension (Tunka-Rex). *Nucl. Instr. Meth. Phys. Res. A*, 802:89–96, 2015. doi: 10.1016/j.nima.2015.08.061.

[79] W.D. Apel et al. Improved absolute calibration of LOPES measurements and its impact on the comparison with REAS 3.11 and CoREAS simulations. *Astropart. Phys.*, 75:72 – 74, 2016. doi: 10.1016/j.astropartphys.2015.09.002.

[80] K. Belov et al. Accelerator measurements of magnetically-induced radio emission from particle cascades with applications to cosmic-ray air showers. *Phys. Rev. Lett.*, 116(14):141103, 2016. doi: 10.1103/PhysRevLett.116.141103.

[81] S.A. Wissel et al. Measurements, system response, and calibration of the SLAC T-510 experiment. In *Proceedings, 34th International Cosmic Ray Conference (ICRC 2015): PoS(ICRC2015)342*, 2016. URL http://pos.sissa.it/archive/conferences/236/342/ICRC2015_342.pdf.

[82] K. Kuwatani. Private communication.

[83] P.W. Gorham et al. The Antarctic Impulsive Transient Antenna Ultra-high Energy Neutrino Detector Design, Performance, and Sensitivity for 2006-2007 Balloon Flight. *Astropart. Phys.*, 32:10–41, 2009. doi: 10.1016/j.astropartphys.2009.05.003.

[84] N.G. Lehtinen, P.W. Gorham, A.R. Jacobson, and R.A. Roussel-Dupré. FORTE satellite constraints on ultrahigh energy cosmic particle fluxes. *Phys. Rev. D*, 69:013008, 2004. doi: 10.1103/PhysRevD.69.013008.

[85] K. Mulrey. SLAC T-510: Radio emission from particle cascades in the presence of a magnetic field. In *Proceedings, 7th Acoustic and Radio EeV Neutrino Detection Activities (ARENA2016)*, 2016. To be published.

[86] K. Mulrey. Private communication.

[87] A. Zilles. Geant4 Simulations of Radio Signals from Particle Showers for the SLAC T-510 Experiment. In *Proceedings, 6th Acoustic and Radio EeV Neutrino Detection Activities (ARENA2014)*, 2014. URL http://slac.stanford.edu/pubs/slacreports/reports21/slac-r-1042.pdf.

[88] A. Zilles et al. Modelling of radio emission in the SLAC T-510 experiment using microscopic Geant4 simulations. In *Proceedings, 34th International Cosmic Ray Conference (ICRC 2015): PoS(ICRC)313*, 2015. URL http://pos.sissa.it/archive/conferences/236/313/ICRC2015_313.pdf.

[89] *Geant4 Physics Reference Manual*. URL http://geant4.cern.ch/G4UsersDocuments/UsersGuides/PhysicsReferenceManual/html/node34.html.

[90] C.W. James. Private communication.

[91] D.R. Williams. *The Askaryan Effect and Detection of Extremely High Energy Neutrinos in the Lunar Regolth and Salt*. PhD thesis, University of California, Los Angeles, 2004.

[92] A. Zilles. Modeling of radio emission from a particle cascade in a magnetic field and its experimental validation. In *Proceedings, 7th Acoustic and Radio EeV Neutrino Detection Activities (ARENA2016)*, 2016. To be published.

[93] K. Mulrey. *Characterizing radio emission from extensive air showers with the SLAC T-510 experiment, with application to ANITA*. PhD thesis, University of Delaware, 2016.

[94] C. Glaser, M. Erdmann, J.R. Hörandel, T. Huege, and J. Schulz. Simulation of Radiation Energy Release in Air Showers. *J. Cosmol. Astropart. Phys.*, 1609(09):024, 2016. doi: 10.1088/1475-7516/2016/09/024.

[95] S.A. Wissel. Private communication.

[96] T. Huege et al. Enabling detection of cosmic ray air showers with SKA-low. Engeneering change proposal submitted to the SKA organisation, July 2015.

[97] T. Huege et al. High-precision measurements of extensive air showers with the SKA. 2015. URL http://pos.sissa.it/archive/conferences/236/309/ICRC2015_309.pdf.

[98] T. Huege et al. Ultimate precision in cosmic-ray detection - the SKA. In *Proceedings, 7th Acoustic and Radio EeV Neutrino Detection Activities (ARENA2016)*, 2016. To be published.

[99] A. Zilles, S. Buitink, and T. Huege. Initial simulation study on high-precision radio measurements of the depth of shower maximum with SKA1-low. In *Proceedings, 7th*

Acoustic and Radio EeV Neutrino Detection Activities (ARENA2016), 2016. To be published.

[100] SKA Organisation. SKA1-Low Configuration, October 2015. URL http://astronomers.skatelescope.org/wp-content/uploads/2015/11/SKA1-Low-Configuration_V4a.pdf. draft.

[101] N. Budnev et al. Tunka-25 Air Shower Cherenkov array: The main results. *Astropart. Phys.*, 50-52:18 – 25, 2013. doi: 10.1016/j.astropartphys.2013.09.006.

[102] F. Riehn. Private communication.

[103] P. A. Bezyazeekov et al. Radio measurements of the energy and the depth of the shower maximum of cosmic-ray air showers by Tunka-Rex. *J. Cosmol. Astropart. Phys.*, 1601(01):052, 2016. doi: 10.1088/1475-7516/2016/01/052.

[104] F. Gaté. X_{max} reconstruction from amplitude information with AERA. In *Proceedings, 7th Acoustic and Radio EeV Neutrino Detection Activities (ARENA2016)*, 2016. To be published.

[105] F.G. Schröder et al. Investigation of the radio wavefront of air showers with LOPES measurements and CoREAS simulations. In *Proceedings, 6th Acoustic and Radio EeV Neutrino Detection Activities (ARENA2014)*, 2015. arXiv:1507.07753.

[106] G. Battistoni et al. The FLUKA Code: An Accurate Simulation Tool for Particle Therapy. *Front. Oncol.*, 6:116, 2016. doi: 10.3389/fonc.2016.00116.

[107] T.K. Gaisser and A.M. Hillas. Reliability of the method of constant intensity cuts for reconstructing the average development of vertical showers. In *Proceedings, 15th International Cosmic Ray Conference (ICRC1977)*, volume 8, pages 353–357, 1977. URL http://adsabs.harvard.edu/abs/1977ICRC....8..353G.

[108] R.S. Roger, C.H. Costain, T.L. Landecker, and C.M. Swerdlyk. The radio emission from the Galaxy at 22 MHz. *Astron. Astrophys. Sup.*, 137:7–19, 1999. doi: 10.1051/aas:1999239.

[109] S. Buitink. Private communication.

[110] H. Schoorlemmer et al. Energy and Flux Measurements of Ultra-High Energy Cosmic Rays Observed During the First ANITA Flight. *Astropart. Phys.*, 77:32–43, 2016. doi: 10.1016/j.astropartphys.2016.01.001.

[111] T. Winchen. Private communication.

[112] F. Diogo. Measurement of the average electromagnetic longitudinal shower profile at the Pierre Auger Observatory. In *Proceedings, 34th International Cosmic Ray Conference (ICRC 2015): PoS(ICRC2015)413*, 2016. URL http://pos.sissa.it/archive/conferences/236/413/ICRC2015_413.pdf.

[113] A. Aab et al. The Pierre Auger Observatory Upgrade - Preliminary Design Report. 2016. arXiv:1604.03637.

DECLARATION

Anne Zilles
Welfenstrasse 19
76137 Karlsruhe
anne.zilles@kit.edu

Erklärung der selbständigen Anfertigung meiner Dissertationsschrift

Hiermit versichere ich, dass ich die Dissertationsschrift mit dem Titel

Emission of Radio Waves in Particle Showers:
Validation of microscopic simulations with the SLAC T-510 experiment
and their potential in the future Square Kilometre Array

selbständig und ohne unerlaubte fremde Hilfe verfasst habe. Dabei habe ich keine anderen, als die von mir angegebenen Hilfsmittel benutzt.

Karlsruhe, den

(Anne Zilles)

ACKNOWLEDGMENTS

Zunächst möchte ich mich bei Prof. Johannes Blümer für die Möglichkeit zur Promotion und die Übernahme des Referats meiner Arbeit bedanken.
Prof. Michael Feindt möchte ich für die Übernahme des Korreferats danken.

Ich möchte mich bei Tim Huege bedanken, der mich als Betreuer meiner Promotion unterstützend und beratend begleitet hat.
Desweiteren möchte ich mich bei Andreas Haungs, Frank Schröder und Qader Dorosti bedanken, die mir ebenfalls jederzeit mit Rat und Tat zur Seite standen.

Außerdem möchte ich mich für eine sehr schöne Zeit im Büro 135 bedanken! Dazu beigetragen haben: Katrin, Aswathi und Agnieszka, als auch in früheren Zeiten, Daniel, Andi und Martin.
Meinen Dank für eine herzliche Aufnahme ins IKP geht auch an alle anderen Doktoranden und Studenten, wie auch an alle Mitarbeiter des IKPs. Hervorheben möchte ich dabei Sabine, Jürgen und Doris, die mir bei der Arbeit z.B. durch Anfertigen von Simulationen, durch mehr Datenspeicherplatz und Drucken der Arbeit geholfen haben.

Additionally, I would like to thank many people I had the chance to work with:

- To the SLAC T-510 collaboration: Thank you that you gave me the chance to contribute to the experiment in such an important way! Special thanks to Konstantin, Steph, Katie, Andres, Dave, Dave and Brian for the faith, input and the help I got from you!
- To the SKA Focus Group on High Energy Particles: Especially, I would like to thank Clancy, Justin and Stijn who gave me input and supported me e.g. with setting up the simulations study.

Ich habe auch soviele Menschen außerhalb des Instituts kennen gelernt, so dass die Liste der Danksagungen viel zu lang würde. Ich danke ihnen für viele Diskussionen, in denen ich gelernt habe oder einfach Spaß hatte, und viele Momente, die wir in und außerhalb der Wissenschaft geteilt haben.

Ein großen Dank geht auch an Flo für das Korrekturlesen dieser Arbeit. ;)